

MASTER 2

Geography Environment Development

Curriculum GEOSPHERES:

Geography – Space – Human – Environment – Resources – Systems

Master in network



Diachronic monitoring of the Folgefonna glacier through remote sensing in a climate change context

Internship completed at the University of Bergen (Department of earth science)

Home University: École des Mines de Saint-Étienne (EMSE)

Master's thesis defended on: 21/07/2022

The jury is composed of:

- **Pr. Steve Peuble**, Professor researcher at the École des Mines de Saint-Étienne
- **Pr. Frédéric Paran**, Professor researcher at the École des Mines de Saint-Étienne

PFUNDSTEIN Guillaume

M2 GEOSPHERES

2021–2022

Partner institutions:

Abstract

Folgefonna is a maritime glacier with three ice caps located in the Hardanger region, south of Norway. This paper studies the glacier's historical and future evolution through remote sensing in a climate change context. This work is divided into four main sections, which the first two are the most critical.

The first section analyzes the development of Folgefonna during the last 80 years. Several characteristics were calculated in parallel to observe this development. The glacier's outlines were computed using satellite imagery (Landsat 8–7–6 and Sentinel 2). These satellite images were also used to calculate the Equilibrium Lines of Altitude (ELA) and the snow coverage. Then, the volume and mass evolution was examined by comparing different Digital Elevation Models (DEMs). The creation of DEMs from photogrammetry from old black and white aerial photographs (carried out during the internship) was onerous. Four DEMs were shaped with this method (1937, 1953, 1962, and 1981). Once created, these DEMs were co-registered, interpolated (via local hypsometry), and the volume and mass difference was calculated. After that, the Gravity Recovery and Climate Experiment (GRACE) dataset was used to calculate the water mass contained in Folgefonna from April 2002 until December 2021. The results present two clear phases in the development of the glacier area since 1959 – an expansion followed by a depletion. The glacier expands by $9 \pm 28\text{km}^2$ (+3.9%, ref. 1959) from 1959 to 1995. Then, from 1995 to 2021, it regresses by $54.6 \pm 25.3\text{km}^2$ (–23%, ref. 1995). From 1994 to 2021, the ELA is elevated by 88.5m and reaches an altitude of 1433.6m in 2021. In the same periods, the snow area is depleted by $45.5 \pm 17.6\text{km}^2$. For the three ice caps of Folgefonna, from 1959 to 2017, the volume of ice declines by $3.03 \pm 0.059\text{km}^3$, the mass decreases by $2.6 \pm 0.6\text{Gt}$, and the sea level rises by $7.2 \pm 1.8\mu\text{m}$. As the DEMs do not cover the entire surface of the glacier, the study area was reduced by 42.3km^2 (19.52%, ref:1959). This reduction allowed for more accurate monitoring of Folgefonna from 1937 to 2021, producing two clear phases of evolution. Until 1962, the volume increases by $0.357 \pm 0.244\text{km}^3$ (mass: $+0.303 \pm 0.317\text{Gt}$); then, from 1962 until 2017, the volume is reduced by $1.087 \pm 0.222\text{km}^3$ (mass: $-0.924 \pm 0.243\text{Gt}$). The computed GRACE data shows a constant mass of water contained in the Folgefonna region from 2002 to 2021.

The second section of this paper elaborates on the advancements produced for processing DEMs. A software called Eagloo was developed in python to automate co-registration, interpolation, integrated errors and volume/mass calculations. The PySimpleGui framework was used to construct the frontend of the software. For the backend, both the Demcoreg and Xdem frameworks were chosen. All DEMs were treated through this software; it allows more efficient processing and simplifies functions in comparison to all existing python frameworks.

The third section of this paper studies the correlation between the evolution of the glacier and the climatic data. The highest correlations come from the moving average of the glacier area over four years and the summer temperature ($r = -0.78$). However, the most relevant correlations could not be calculated due to a lack of data for the evolution of the DEMs.

The last section forecasts Folgefonna's features until the year 2100. To assess the glacier's potential evolution, the Open Global Glacier Model (OGGM), an open-source python framework, is employed. Four different scenarios were taken into account. In the lowest emission scenario (RCP 26), the glacier loses 6.5km^3 (–21.6%), while its volume is reduced by 11.1km^3 (–37%) in the highest emission scenario (RCP 85).

Résumé

Le Folgefonna est un glacier maritime composé de trois calottes de glace. Il est situé au sud de la Norvège, dans la région de Hardanger. L'objectif était d'analyser l'évolution future et passée de ce glacier dans un contexte de changement climatique, à partir de techniques de télédétection. Cette étude a été scindée en quatre parties, dont les deux premières sont les plus importantes.

Dans un premier temps, l'évolution passée du Folgefonna a été analysée durant les 80 dernières années. Plusieurs caractéristiques ont été calculées en parallèle. Premièrement, les évolutions de la surface, de la ligne d'équilibre (limite entre la neige et la glace) et de l'enneigement estival du glacier ont été analysées à partir d'images satellite (Landsat 8-7-6 et Sentinel 2). Ensuite, les évolutions du volume et de la masse ont été calculées à partir de plusieurs Modèles Numériques de Terrain (MNT). Une partie conséquente de ce travail fut de générer des MNT à partir d'anciennes photographies aériennes en noir et blanc (réalisé durant le stage). Avec cette méthode quatre modèles ont été obtenus (1937, 1953, 1962 et 1981). Ils ont ensuite été co-enregistrés, interpolés à partir d'une méthode hypsométrique locale, et les différences de volume et de masse ont été calculées. Ensuite, en utilisant les données GRACE (Gravity Recovery and Climate Experiment), l'équivalent en masse d'eau a été analysé d'avril 2002 à décembre 2021 à partir de données gravimétriques. En ce qui concerne les résultats obtenus, l'évolution de la superficie du glacier a connu deux phases différentes, de 1959 à 1995 le glacier a augmenté de $9 \pm 28 \text{ km}^2$ (+3.9%, ref. 1959). Puis de 1995 à 2021, il a réduit de $54,6 \pm 25,3 \text{ km}^2$ (-23 %, réf. 1995). Pour la ligne d'équilibre, entre 1994 et 2021, elle s'est élevée de 88,5 m, avec une altitude de 1433,6 m en 2021. De 1959 à 2017, le volume et la masse ont respectivement diminué de $3,03 \pm 0,06 \text{ km}^3$ et de $2,6 \pm 0,6 \text{ Gt}$, impliquant une élévation du niveau de la mer de $7,2 \pm 1,8 \text{ } \mu\text{m}$. Les MNT calculés ne couvrant pas la totalité de la surface du glacier, le choix a été fait de réduire la zone d'étude à $42,3 \text{ km}^2$ (soit 19,52 % de la surface totale du glacier, ref:1959). Ce rétrécissement a permis d'obtenir un suivi plus précis du Folgefonna. Sur la période étudiée, deux phases ont été observées. De 1937 à 1962, le volume du glacier a augmenté de $0,357 \pm 0,244 \text{ km}^3$ (masse : $+0,303 \pm 0,317 \text{ Gt}$). Puis de 1962 à 2017, le Folgefonna a perdu un volume de $1,087 \pm 0,222 \text{ km}^3$ (masse : $-0,924 \pm 0,243 \text{ Gt}$). Pour les données GRACE de 2002 à 2021, la masse d'eau contenue dans la région du Folgefonna semble être constante.

La deuxième partie de cette étude fut d'améliorer le traitement des MNT. Un logiciel nommé Eagloo a été développé en python afin d'automatiser le processus de co-enregistrement, d'interpolation, d'erreurs intégrées et des calculs de volume et de masse. La partie frontend a été développée à partir du framework PySimpleGui. Quant à la partie backend, les frameworks Demcoreg et Xdem ont été utilisés pour les fonctions principales du logiciel. Ce dernier a été utilisé pour traiter chacun des MNT, il permet d'augmenter la vitesse de traitement et de faciliter l'utilisation des fonctions en comparaison avec les frameworks déjà existants.

Par la suite, une analyse de la corrélation entre l'évolution des paramètres du glacier et les données climatiques a été effectuée. Le plus haut coefficient de corrélation a été obtenu entre la moyenne glissante de la surface du glacier sur quatre ans et la température d'été ($r = -0,78$). Cependant, en raison d'un manque de données, les calculs de corrélation entre les données climatiques et l'évolution via le suivi des MNT n'ont pas pu être réalisés.

Dernièrement l'évolution future du Folgefonna a été modélisée de 2020 à 2100, un script open source nommé Open Global Glacier Model (OGGM) a été utilisé. Quatre scénarios ont été retenus, pour celui associé aux plus faibles émissions (RCP 26), le glacier pourrait diminuer de $6,5 \text{ km}^3$ (soit - 21,6%, ref :2020) ; quant à celui représentant les plus hautes émissions (RCP 85), il diminuerait de $11,1 \text{ km}^3$ (soit - 37%, ref : 2020).

Plagiarism declaration

I, the undersigned, Guillaume Pfundstein declare on honor:

1. I know that plagiarism means taking and using the ideas, writings, works or inventions of another as if they were one's own. I know that plagiarism not only includes verbatim copying, but also the extensive use of another person's ideas without proper acknowledgment (which includes the proper use of quotation marks). I know that plagiarism covers this sort of use of material found in textual sources and on the Internet.

2. I acknowledge and understand that plagiarism is wrong.

3. I understand that my research must be accurately referenced. I have followed the rules and conventions concerning referencing, citation and the use of quotations.

4. This assignment is my own work. I acknowledge that copying someone else's assignment, or part of it, is wrong and that submitting identical work to others constitutes a form of plagiarism.

Completed in Bergen

Date: 15/07/2022

Signature of the master's author: Guillaume Pfundstein

Bibliographic record

Work: Master thesis

Author: Guillaume Pfundstein

Title of the project: Diachronic monitoring of Folgefonna Glacier through remote sensing in a climate change context

Defense date: 21/07/2022

Home University: École des Mines de Saint-Étienne

Internship place: University of Bergen, Norway

Home university supervisor: Pr. Steve Peuble

Internship supervisor: Pr. Andreas Born / Pr. Benjamin Aubrey Robson

Pages: Number of pages: 73 / Number of appendices: 15 / Number of bibliographic references: 61

Analytic Keywords: Glaciology, Remote sensing, Photogrammetry, Gravimetry, Co-registration, Interpolation, Digital Elevation Model (DEM)

Geographic Keywords: Folgefonna, Hardanger, Vestland county, Norway

Acknowledgments

I would like to acknowledge and give my thanks to my home university supervisor, Pr. Steve Peuble, for his patience, guidance, and support. I have benefited greatly from his wealth of knowledge.

Very special thanks to Pr. Didier Graillot, now professor emeritus, who throughout my schooling at the École des Mines de Saint-Étienne was of invaluable help. It also allowed me to immerse myself in the path of earth sciences.

I am grateful to Pr. Benjamin Robson for his patient support, very precious guidance, and supervision during my internship at the University of Bergen.

My sincere thanks to Pr. Andreas Born who allowed me to complete an internship at the University of Bergen.

I am also thankful to my associated supervisors Pr. Pierre-Alain Ayrat, Pr. Jean-Jacques Delannoy, Pr. Nathalie Dubus and Pr. Frederic Paran for their noble guidance, and support with full encouragement and enthusiasm.

As well as the entire teaching and administrative team of the École des Mines de Saint-Étienne, for their high-quality attention.

I would also like to give special thanks to my partner Annick Voutat and my family as a whole for their continuous support and understanding when undertaking my research and writing my project.

Table of contents

Abstract	iii
Résumé	iv
Plagiarism declaration	v
Bibliographic record	vi
Acknowledgments	vii
Table of contents	viii
Glossary	xi
Chapter 1 Introduction and issue	1
1.1 Glaciers in a climate change context	1
1.2 Remote sensing in glaciology	2
1.3 Objectives and outlines	3
Chapter 2 Study area	5
2.1 Presentation of Folgefonna	5
2.2 Climate change and historical glacier evolution	6
2.2.1 Historical glacier evolution in Norway	6
2.2.2 Holocene	6
2.2.3 Climate evolution	6
2.3 Hydropower plants	6
2.3.1 Hydropower plants in Norway	6
2.3.2 Hydropower plants around Folgefonna	7
Chapter 3 Literature review	8
3.1 Remote sensing technologies used in the last decades in glaciology	8
3.1.1 Glacier area	8
3.1.2 Equilibrium Lines Altitude (ELA)	8
3.1.3 Photogrammetric survey method	9
3.1.4 DEMs generated by altimetric data	9
3.1.5 Processing DEMs	10
3.1.6 Gravimetry	13
3.2 Glacier mass balance	13
3.3 Correlations between meteorological data and Folgefonna features	14

Chapter 4	Methodology and Data	15
4.1	Historical evolution of Folgefonna with remote sensing	15
4.1.1	Evolution of the glacier area with satellite imagery	16
4.1.2	Evolution of the Equilibrium Line Altitude	18
4.1.3	Snow coverage	19
4.1.4	DATA synthesis of glacier area, ELA and snow coverage	20
4.1.5	Photogrammetric DEM calculation	21
4.1.6	Formerly generated DEMs	26
4.1.7	Co-registration, bias corrections and interpolations of DEMs	27
4.1.8	Evolution of Folgefonna's geophysical features	30
4.1.9	Evolution of the mass balance by gravimetry	33
4.2	DEM processing software development	34
4.3	Correlation calculations	35
4.3.1	Correlation of ELA and glacier area	35
4.3.2	GRACE data correlations	35
4.4	Open-Global Glacier Model – historical and future evolution	36
4.4.1	Model description	36
4.4.2	Choice of the methods	36
4.4.3	Workflow	37
4.4.4	Model description	38
4.4.5	Climatic data	39
4.4.6	Spatial data	39
Chapter 5	Results	40
5.1	Historical evolution of Folgefonna by remote sensing	40
5.1.1	Evolution of the glacier area	40
5.1.2	Equilibrium Lines Altitude	44
5.1.3	Snow area on glacier	46
5.1.4	DEMs evolution	47
5.1.5	Gravimetry– GRACE	52
5.2	Results with the Eagloo software	55
5.2.1	Layer homogenization	56
5.2.2	Co-registration	
	Error! Bookmark not defined.	
5.2.3	Subtraction	57
5.2.4	Interpolation	58
5.2.5	Errors based on slope and curvature	58
5.2.6	Mass and volume calculation	59
5.2.7	PDF report generation	60
5.3	Climatic data and correlation	60
5.3.1	Climatic data	60
5.3.2	Correlation between glacier features and climatic data	62
5.4	OGGM results	65
5.4.1	Historical evolution	65
5.4.2	Future evolution	66

Chapter 6	Analysis and discussions	68
6.1	Methods and results discussion	68
6.1.1	Evolution of glacier area, TSL and snow coverage	68
6.1.2	DEM evolution	69
6.1.3	Gravimetry	70
6.1.4	Eagloo	70
6.1.5	Folgefonna evolution	71
6.2	Analysis of the Results	71
Chapter 7	Conclusion	73
7.1	How have Folgefonna's features evolved during the last century using remote sensing methods?	73
7.2	How can photogrammetric processing be improved?	73
7.3	Is there a strong correlation between the evolution of Folgefonna and the climatic data?	74
7.4	How will Folgefonna evolve facing different climatic scenarios?	74
References		75
A.	Appendix	80
	List of figures	90
	List of tables	92
	List of diagrams	93
	List of appendices	94

Glossary

The following acronyms and abbreviations are used in this report.

Abbreviation	Description
AGEI	Automated Glacier Extraction Index
BP	Before Present
dDEMs	Subtraction between two Digital Elevation Models
DEM	Digital Elevation Model
ELA	Equilibrium Line Altitude
GCP	Ground Control Point
GRACE	Gravity Recovery and Climate Experiment
ICP	Iterative Closest Point
LIA	Little Ice Age
LiDAR	Light Detection And Ranging
M.A.S.L.	Meters Above Sea Level
m.w.e.	Meter water equivalent
NIR	Near-infrared
NMAD	Normalized Median Absolute Deviation
RMSE	Root Mean Square Error
TSL	Transient Snow Line
Sfm	Structure from Motion
SRTM	Shuttle Radar Topography Mission
SWIR	Shortwave Infrared
RaDAR	Radio Detection And Ranging
ROI	Regions Of Interest

Chapter 1

Introduction and issue

In this chapter, a presentation of glaciers in a climate change context is firstly given; secondly, the main remote sensing methods used in glaciology are presented, and finally, the issues and methods are described.

1.1 Glaciers in a climate change context

Glaciers are formed where climate conditions and topographic features enable the accumulation of snow over the years. The snow gradually transforms into ice through a long, complex and highly temperature-dependent process (Benn and Evans, 2010). On planet earth, glaciers are also subject to gravity. They flow at the speed of the main function of ice temperature and topography. The two main processes are the accumulation, a gain of snow and ice, and the ablation associated with the loss of snow and ice. The mass balance of a glacier is determined by summing all accumulation and ablation processes.

Glaciers are one of the most sensitive geophysical indicators of climate change, as their geometry is adjusted in response to the evolution of temperatures and precipitations (IPCC 2021). During the 20th century, glaciers lost a consequent mass. Numerous studies have suggested that anthropogenic activities are considerably responsible for this rapid climate change (Thompson, 2010). Glacier changes can lead to several direct destabilizations in our current societies. Firstly, retreating glaciers increase geohazards, such as landslides or floods (Richardson and Reynolds, 2000). They disturb runoff seasonality which many humans depend highly on. Finally in the coming decades, glaciers will be critical contributors to the rise in sea-levels and will most likely drive significant changes in the hydrological regime of glacierized drainage basins in the mountains (Vuille et al., 2018; Hock et al., 2019).

The climate on earth has always fluctuated. From 29,000 to 21,000 BP (the last glacial maximum), the sea level was about 134m lower than it is today, with a maximum grounded ice volume of $\sim 52 \times 10^6 \text{ km}^3$ greater than today (Lambeck et al., 2014). Between the end of the last glacial maximum and now (2022), the global average temperature has increased by $6.1 \text{ }^\circ\text{C}$ (95% confidence interval: 6.5 to $5.7 \text{ }^\circ\text{C}$) (Tierney et al., 2020).

At present, the thermal expansion of the oceans represents about one-third to half of the observed rate of the rising sea-levels. Mass loss from the world's ice-covered regions such as Greenland, Antarctica, small ice caps, and mountain glacier systems drives the remainder (Church and al., 2013). The ice currently contained in glaciers could raise the sea levels by $65.64 \pm 1.03\text{m}$ (Farinotti et al., 2019; Morlighem et al., 2017; Morlighem et al., 2019), with $57.9 \pm 0.9\text{m}$ only for the Antarctic ice sheet (Morlighem et al., 2019), $7.42 \pm 0.05\text{m}$ for the Groenland (Morlighem et al., 2017) and $0.32 \pm 0.08\text{m}$ for the 215,000 other glaciers of the world (Farinotti et al., 2019).

1.2 Remote sensing in glaciology

Remote sensing in glaciology is a recent method for glacier monitoring. It allows the observation of an extensive range of glaciers without lengthy and costly field work missions. These methods are notably valuable for hard-access regions such as Antarctica or Greenland.

Data can be collected through several intermediaries (place/engine). Commonly in glaciology, these are:

- From the ground directly
- From drones
- From helicopters
- From airplanes
- From satellites

The data is collected with an extensive range of sensors. However, only two families of sensors exist; passive sensors directly detect input from the physical environment and active sensors, which send out a signal. All of these sensors convert input from the physical environment to numerical data. The primary sensors used in glaciology are the following:

- Camera (type: passive sensor – physical input: light radiations)
- Gravimetric sensor (type: passive sensor – physical input: gravity strength)
- Light Detection And Ranging (LiDAR) (type: active sensor – emitted signal: light wave – calculation: the time between emission and reception)
- Radio Detection And Ranging (RaDAR) (type: active sensor, emitted signal: electromagnetic wave, calculate: time between emission and reception)

From the gathered raw data, the following calculations are possible:

- Digital Elevation Model (DEM) with photogrammetry (entries: photographs)
- DEM with LiDAR or RaDAR data
- Evolution of mass (Gravimetric data)
- Glacier area (entries: Photographs (multispectral images))
- Transient Snow Lines (TSLs) (entries: photographs (multispectral images))

These technics are increasingly used in glaciology due to the surge in satellite and airplane density and technological improvement.

An example for the camera, $\frac{d^2\theta}{dt^2}$ (calculated in equation 1.1) has constantly been positive during the last decades:

$$\theta(t) = \frac{\text{Resolution}(t) \times \text{Lens_quality}(t) \times \text{Speed_of_focusing}(t)}{\text{Weight}(t) \times \text{Camera_distortion}(t) \times \text{Price}(t)} \quad (1.1)$$

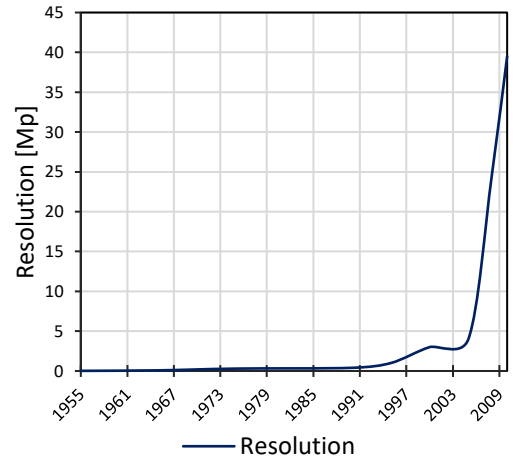


Figure 1.1: Temporal evolution of public camera resolution, in megapixels, as a function of the year. (data: Youssef, 2005)

1.3 Objectives and outlines

This work set out to use a wide range of remote sensing methods on a specific glacier with high data availability to observe the past evolution of such a glacier.

The Folgefonna glacier, located in the south of Norway, has three ice caps. This work focuses on these ice caps. Although the volume of water contained in Folgefonna is of minor consequence in the rising sea levels, studying these ice caps is valuable in better understanding the evolution of glaciers globally.

Main issue: What is the historical and future evolution of Folgefonna in a climate change context through remote sensing methods?

Underlying issues:

- 1 – How have Folgefonna’s features evolved during the last century using remote sensing methods?
- 2 – How can DEMs processing be improved?
- 3 – Is there a strong correlation between the evolution of Folgefonna and the climatic data?
- 4 – How will Folgefonna evolve facing different climatic scenarios?

Legitimacy:

Global–scale: Observing the evolution provides a better understanding of the glacier's dynamics in a rapid climate change context and improves global glaciological models.

Local–scale: Assessing the mass balance evolution of Folgefonna is vital for the dependent hydraulic electricity production.

Plan and methodology:

This research is divided into four underlying issues:

- 1- Determination of the evolution of Folgefonna during the last century using an extensive range of remote sensing methods:
 - Calculation of glacier outlines of Folgefonna through free satellite images
 - Definition of the evolution of the Equilibrium Lines Altitude (ELA – lines between accumulation area and ablation area)
 - Computation of Digital Elevation Models (DEMs) from old black and white photographs by using photogrammetry
 - Search of already calculated DEMs (LiDAR, photogrammetry)
 - Post-process of the DEMs (co-registration, interpolation)
 - Computation of the volume and mass change with its associated errors
 - Observation of the development of the water mass balance using gravimetric data

- 2- Development of software for DEM processing (co-registration, interpolation, subtraction, errors, volume, and mass calculations)

- 3- Calculation of the potential correlations between climatic data (temperature, precipitation) and variations in glacier features.

- 4- Observation of the potential evolution of Folgefonna following climate previsions and analysis of climatic data correlations via open-source python glacier model script.

Note:

This thesis was partially accomplished during an internship proposed by the University of Bergen (Department of earth science). The processing of DEMs with old black and white aerial photography and their co-registration was performed during the internship.

The development of the software (Eagloo), calculation of glacier outlines, Equilibrium Lines Altitude (ELA), the evolution of water mass balance by gravimetry, and correlation between glacier evolution and climatic data were carried out outside of the framework of the traineeship.

Chapter 2

Study area

2.1 Presentation of Folgefonna

Folgefonna is the third largest glacier in mainland Norway. It is made of three ice caps located on the western Norwegian coast ($60^{\circ} 00.34' N$; $6^{\circ}21.06' E$), approximately 65km southeast of the city of Bergen. It is a maritime-type glacier with heavy snow accumulations in winter and substantial ablation in the summer period (Imhof et al., 2011).

The three glacial entities are Nordre Folgefonna (24.8km^2), Midtre Folgefonna (9.1km^2), and Søndre Folgefonna (156.7km^2) (data from 2011). Their elevation ranges from 730m to over 1,635m. The ice volume was estimated to be 28km^3 with a maximum depth of 570m in 2019 by subtracting of a DEM and a subglacial topographic map measured by ice radar (Johansson et al., 2019).

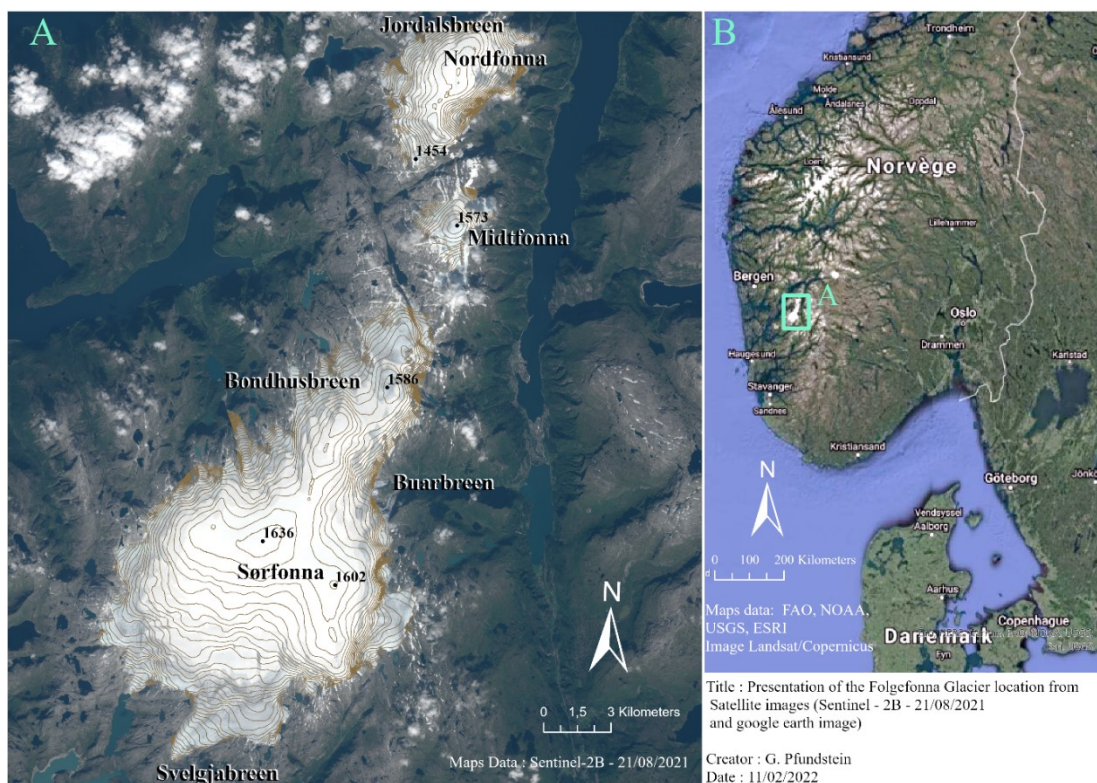


Figure 2.1: Presentation of the location of Folgefonna from satellite images (Maps data: Sentinel – 2B – 21/08/2021 and google earth image)

2.2 Climate change and historical glacier evolution

2.2.1 Historical glacier evolution in Norway

Norwegian glaciers are mainly composed of maritime glaciers. According to a study performed by Winsvold et al. in 2014 based on Landsat TM/ETM+ and digitized topographic maps, Norwegian mainland glaciers have lost an area of 2,994km² between 1947 and 1985¹ to 2,668km² for the period between 1999 and 2006 (corresponding to –326km², or –11% of the initial period).

Due to their maritime characteristics, these glaciers have seen a mass surplus between 1962 and 2000 (Andreassen et al., 2005). Indeed, coastal glaciers such as Ålftobreen and Nigardsbreen have gained significant total mass, +9m.w.e. and +17m.w.e. respectively. The period from 1989 to 1995 was highly positive due to snow-rich winters, while the continental glaciers globally retreated. For Norwegian glaciers, increasing precipitations counterbalanced the rise in temperatures.

2.2.2 Holocene

Almost all glaciers in Norway had their Holocene maxima during the Little Ice Age (LIA) (Bogen et al., 1989). According to a study of Bondhusbrea and Buerbreen on the south of Folgefonna, the LIA maximum was reached in the late 1870s, with a second peak around 1890 (Nussbaumer et al., 2011). However, there is no historical evidence before AD 1800.

2.2.3 Climate evolution

The climate has changed significantly in southwestern Norway. In Bergen, a Norwegian city located 65km from Folgefonna, for the period from 1900 to 2000, precipitations have increased by 7 % in summer and by 19 % in winter, and the mean temperature has increased by 0.71 °C (calculated from the meteorological data available on the Norwegian Meteorological Institute website met.no).

2.3 Hydropower plants

2.3.1 Hydropower plants in Norway

In Norway, hydropower supplies 90% of the country's electricity (Statkraft, 2022) – and 15% comes from glacier runoff. The installed hydropower capacity is estimated to be 14,447MW, with a total hydropower production of 63TWh (Statkraft, 2022). In 2017, Norway had more than 1,000 hydropower reservoirs, with a maximum stored energy of approximately 85TWh (Graabak et al., 2017).

¹ Due to long-time monitoring, this is a period, not a date.

2.3.2 Hydropower plants around Folgefonna

The hydro-electrical industry exploits most of the drainage basins of Folgefonna. These infrastructures depend directly on the discharge of meltwater.

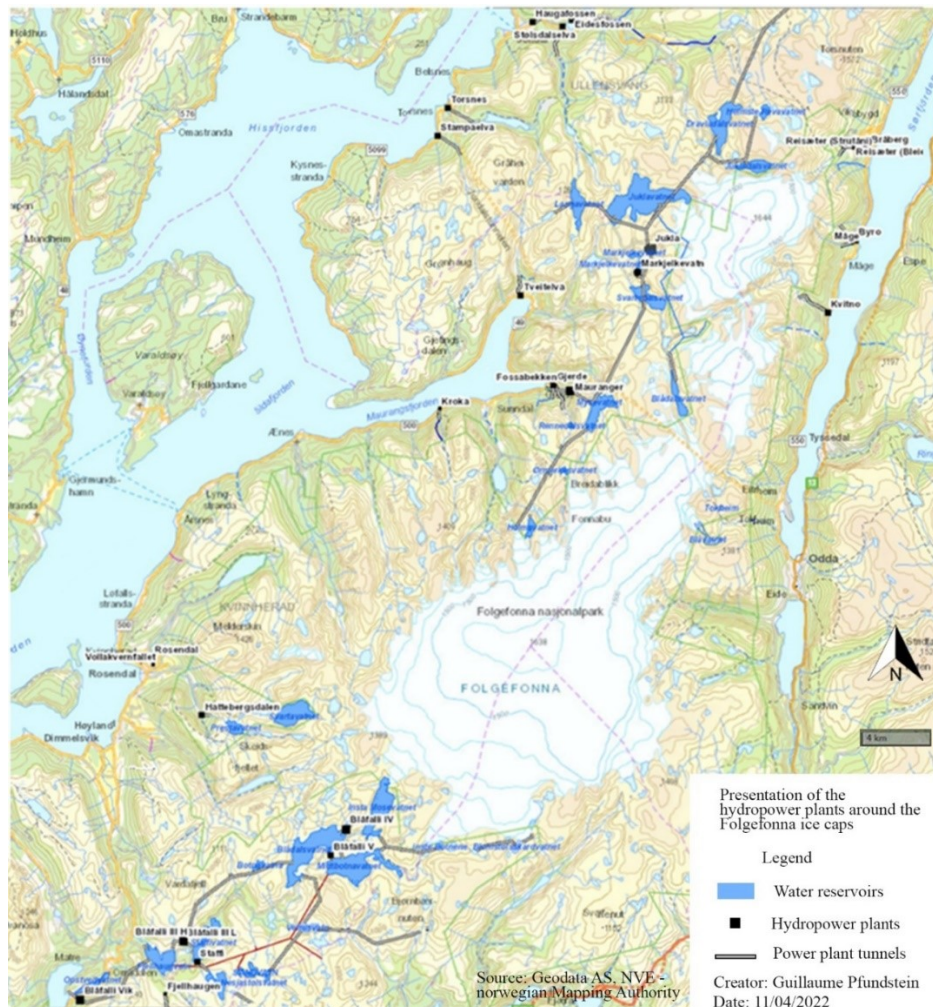


Figure 2.2: Presentation of the hydropower plants on the drainage basins of Folgefonna's ice caps (Source: Geodata AS, NVE – Norwegian Mapping Authority).

There are nine hydropower plants around the glacier, with a total maximum production of 565.46MW (calculated from data provided by the Norwegian Water Resources and Energy Directorate (NVE): nve.no).

There are two major installations:

- **Mauranger** is a hydropower plant located on the west of Folgefonna. This plant has been operating since 1974 and produces a maximum performance of 250MW (annual production of 1,316.5GWh). Almost each drainage basin of this plant is supplied by the glacier, with seven artificial reservoirs connected by an extensive tunnel network. This installation is critically dependent on runoff supplied by Folgefonna. The total drainage basin is approximately $167 \pm 15\text{km}^2$ (2022 – calculated from a topographic map provided by NVE).
- **Blåfalli Vik** is a more recent hydropower plant south of Folgefonna in operation since 2003. It has a maximum performance of 230MW (annual production of 810GWh). Nine artificial reservoirs (linked by tunnels) are above the main plant and four smaller plants. The total drainage basin is $177 \pm 20\text{km}^2$ (2022 – calculated from a topographic map provided by NVE).

Chapter 3

Literature review

This section presents the main physical and mathematical technical principles used in this work.

3.1 Remote sensing technologies used in the last decades in glaciology

3.1.1 Glacier area

The glacier area is the size of the glacier calculated at the end of the ablation season (beginning of accumulation season), generally between August and October.

3.1.1.1 Glacier area utility

There is no strong correlation between glacier area and mass balance. However, the glacier area is an indicator of the glacier's health.

3.1.1.2 Remote computation of the glacier area

There is a wide range of methods to compute the glacier area. All methods use a very low spectral reflectance of ice and snow in the shortwave infrared (SWIR) versus the high reflectance in the visible spectrum (VIS) to identify glaciers (Dozier, 1989) from aerial or satellite images.

According to Paul et al., 2015, generating contrast-enhanced false-color composites is recommended. It is equivalent to bands 3, 2, 1 (321), 432 and 543 as RGB (Red, Green, Blue) for the Landsat Thematic Mapper (TM). The comparison of the main calculation methods from the glacier's area proves the simple band ratio method to be the finest (i.e. Albert 2002; Paul and Kääb, 2002; Paul and Kääb, 2005). The method is more straightforward, accurate, efficient and robust than all others.

3.1.2 Equilibrium Lines Altitude (ELA)

The mass–balance evolution can be determined by monitoring the ELA, as a correlation between the height of the TSLs (ELA) and the annual specific net mass balance exists (Østrem, 1975).

The ELA can easily be identified from conventional air or satellite photographs.

3.1.3 Photogrammetric survey method

Automated aerial and close-range digital photogrammetry have become powerful tools for three-dimensional topographic modelling (Remondino and El-Hakim, 2006; Matthews, 2008; Fraser and Cronk, 2009). Photogrammetry is used to calculate several DEMs of Folgefonna; this section presents the principles of this processing method.

3.1.3.1 Structure from motion

The ‘Structure-from-motion’ (Sfm) is a photogrammetric method for building DEMs. It does not need to know the 3D location of the photographic engine. Sfm is an inexpensive, effective and flexible approach to capture complex topography (Westoby et al., 2012). Sfm can produce DEMs of similar quality to traditional photogrammetric methods (Mölg and Bolch, 2017). However, it differs fundamentally from traditional photogrammetry as the orientation and location are automatically calculated through photogrammetric software such as Metashape or OrthoEngine. The quality of the final point cloud depends on the photo set’s density, sharpness, and resolution (Westoby et al., 2012). As the resolution impacts the quality of DEMs, so does the distance between the object and the camera. Three photographs of the same object are the minimum requirement for photogrammetry; however, using more photographs for the Sfm method significantly improves DEM quality.

3.1.3.2 Lens distortion

One of the main problems in photogrammetry is the distortion caused by the camera lens. Lens aberration alters the resulting image on film or a sensor. This distortion is inherent to each camera; it can involve scale, position, and other features in a photograph (Neale et al., 2011). Lens distortion must be considered to reduce final biases in a DEM.

Numerous software calculate the distortion coefficient to automatically correct the lens distortion. The distortion correction relies on a polynomial function that modifies the distance of a pixel from the center of the image.

In this work, lens distortion was taken into account only when calibration reports were available.

3.1.4 DEMs generated by altimetric data

3.1.4.1 LiDAR and RaDAR

To generate DEMs from altimetric data, Radio Detection And Ranging (RaDAR) or Light Detection And Ranging (LiDAR) is used to calculate the distance between the satellites and the ground points by knowing wave celerity. As the positions of satellites (or airplanes and drones) is known, the accurate altitudes of ground points can be found. The ice volume can be calculated through the altitude and bedrock topography of a glacier.

3.1.4.2 Satellite data

There are three global elevation datasets available to date, Shuttle Radar Topography Mission (SRTM), ICESat, and the ASTER GDEM. However, only SRTM and ICESat were used.

3.1.4.2.1 SRTM

SRTM DEMs have been available since 2000. SRTM uses two single-pass interferometric SAR systems. This radar technology uses electromagnetic waves that penetrate deeply into the snow. According to several studies in the French Alps, significant altitudinal biases have been estimated at -7m every $1,000\text{m}$ in the ice-free area, and SRTM elevations are underestimated by up to 10m (Berthier et al., 2006). Spatial pixels measure $30\text{m} \times 30\text{m}$ with a 16m absolute vertical linear accuracy and a 20m absolute horizontal accuracy. SRTM missions have captured data as far as 60° north. As Folgefonna is located at this latitude, data provided by SRTM does not cover the whole area.

3.1.4.2.2 ICESat

Two near-polar orbit missions with an altitude of approximately 600km have been launched. The first one (ICESat) was conducted from 2003 to 2010, while the second one (ICESat-2) has been in operation since 2018. Both use an altimetric laser system; for ICESat, the Geoscience Laser Altimeter System (GLAS) was used, and for ICESat-2, the Advanced Topographic Laser Altimeter System (ATLAS).

According to several studies, the ICESat performed the best results for analyzing the evolution of the ice volume through satellite monitoring. The altimeter has proven accuracy within $\pm 15\text{cm}$ over flat deserts (Fricker et al., 2005). ICESat products are freely available on the NSIDC website.

3.1.4.2.3 DATA used

Due to the availability of more accurate data, two DEMs from ICESat and one SRTM DEM from 2000 were only used for comparisons².

3.1.5 Processing DEMs

To compare and execute calculations between several DEMs (i.e. volume change, mass change), post-processing steps such as co-registration, interpolation, errors, and features calculations (volume and mass) may be necessary. All the methods presented here are implemented in the developed software.

3.1.5.1 Co-registration

Once DEMs are generated, a co-registration between two DEMs can be required. Indeed, errors and biases may persist from technical limitations, sensor instabilities or bad surveying conditions on the ground. Along with mistakes in volume change, these errors can affect the accuracy of the measurements over the years (Nuth and Kääb, 2011). The co-registration between two DEMs is based on common stable ground between the DEM, which has to be

² This data is introduced in the literature review as it was partially used for this work.

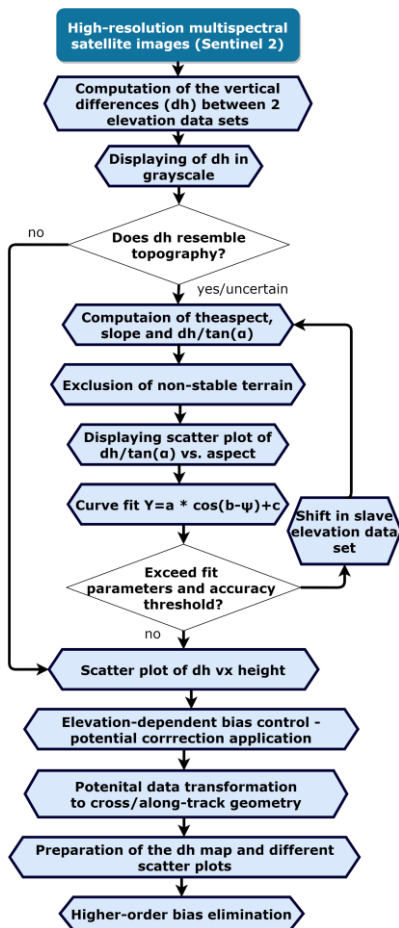


Diagram 3.1: Co-registering process for a DEM to a reference DEM with the Nuth and Käab algorithm credit: Nuth and Käab, 2011

co-register, and the reference DEM. The purpose is to reduce the differences between the common stable ground by applying a translation and a potential rotation on the three spatial axes(x,y,z) on unstable ground, such as glaciers, rivers, lakes, and landslides or avalanches.

From the various co-registration methods, four were chosen:

- Nuth and Käab
- Iterative Closest Points (ICP)
- Deramp
- Vertical Offset

3.1.5.1.1 Nuth and Käab

The Nuth and Käab algorithm (Nuth and Käab, 2011) is based on the existence of a relationship between elevation differences and the derivatives of slope and aspect of two misaligned DEMs. The purpose is to approximate equation 3.1. This equation allows the calculation of the shift to be applied to the one of the DEMs, following three axes(x,y,z).

$$dh = a \cdot \cos(b - \varphi) * \tan \alpha + \overline{dh} \quad (3.1)$$

Where dh is the individual elevation difference, a is the magnitude of the horizontal shift, b is the direction of the shift vector, α is the terrain slope, φ is the terrain aspect, and \overline{dh} is the overall elevation bias between the two elevation datasets.

On stable ground (ice-free terrain), a polynomial relationship between the elevation differences and elevation is used to adjust the DEMs (Nuth and Käab, 2011):

$$dh = \sum_1^n \kappa_n Z^n + \tau \quad (3.2)$$

Where Z is the elevation, κ and τ are the regression parameters and n is the order of the polynomial.

Note: This method operates only in translation on the three-location axis – no rotations are performed.

3.1.5.1.2 Iterative closest point

The Iterative Closest Point (ICP) is a co-registration algorithm that works by iteratively moving a shift DEM until it fits the reference DEM as closely as possible. It consists of computing the nearest neighbor analysis between a reference DEM and the DEM to be aligned. Once it is carried out, the calculated shifts are applied to the DEM, and the processing restarts until it reaches a shift limit.

Note: This method operates in rotation and translation.

3.1.5.1.3 Deramp

Deramp works by estimating and correcting for an N-degree polynomial over the entire subtraction between a reference DEM and the DEM to be aligned (dDEM)³. It is especially useful to correct small rotations in the dataset or nonlinear errors that, for example, often occur in Sfm (Rosnell et al., 2012).

3.1.5.1.4 Vertical offset

The vertical offset algorithm only estimates the altitude difference between a reference DEM and the DEM to be aligned. The average is calculated, and the shift is applied to the DEM to be aligned. In the developed software, this algorithm was always coupled with another algorithm.

3.1.5.2 Interpolation

Some DEMs present voids on the glacier. To reduce these, interpolation calculations are executed. Three different algorithms are used – linear interpolation and local and regional hypsometric interpolation.

3.1.5.2.1 Linear interpolation

The linear spatial interpolation of a dDEM is the most straightforward approach for interpolation. The voids are filled by calculating the average of pixel values around a specific point. The size of the interpolation circles is the lonely parameter that must be set out.

3.1.5.2.2 Local and regional hypsometric interpolation

The hypsometric method is interesting for glacier interpolation. It assumes a relationship between the altitude and the elevation change in the dDEM, which often is the case for glaciers. This relationship is strongly correlated for a specific glacier but weakly correlated at the regional scale.

The difference between the local and the regional method is the following:

- **Local method:** the interpolation is located in small areas; in this case, Folgefonna would be divided following the drainage basins so there would be more than ten interpolation areas and several elevation changes over the entire glacier.
- **Regional method:** the interpolation is calculated on a vast area; in this case, the interpolation coefficients would be computed on the three ice caps, disregarding south and north exposition. For a specific altitude, only one elevation change is associated with the entire glacier.

³ Subtraction between two DEMs : $dDEM = DEM_1 - DEM_2$

3.1.5.3 Ice density for volume change to mass change conversion

The ice density coefficient is used to convert volume change into mass change. This index is heterogenous as a function of several features (particularly depth and time). Fresh snow has a density of 0.05 to 0.07g/cm³, while wet and firm snow has a density of 0.7 to 0.8g/cm³ (Muskett, 2012). The ice density of pure ice is 0.917g/cm³.

As shown in the graph created by Huss in 2013 (on the right), ice density is shown as a function of depth. The ice seems to reach its maximum at approximately 22m deep.

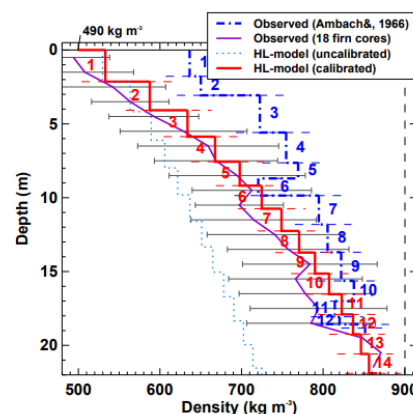


Figure 3.1: Ice density as a function of depth – credit: Huss, 2013

3.1.6 Gravimetry

Gravimetry is a research field measuring the acceleration of gravity. It is a geodesic discipline which determines the shape of Earth, its gravitational field, and its rotation (Ramilien, 2016). The shape of Earth is characterized by the surface topography and gravitational field.

The Gravity Recovery and Climate Experiment (GRACE) satellite mission were launched in 2002 by NASA and Deutsches Zentrum für Luft – und Raumfahrt (German space agency). GRACE provides a monthly global field solution. The gravity field provided by this mission is used to study many geophysical processes involving changes in Earth's mass distribution (Wouters and al., 2014). Indeed, it can be used to measure the evolution of soil moisture, groundwater, floods or glaciers.

Mass variations on Earth's surface can be calculated through this method in glaciology. However, the uncertainty in monitoring the evolution of low glacierized areas can be high.

3.2 Glacier mass balance

The mass balance cannot directly be measured through a remote sensing method. However, there is a strong correlation between the annual Equilibrium Line Altitude (ELA), representing the altitude of the Transient Snow Line (TSL) at the end of summer and the surface mass balance (SMB) ($r > 0.67$) (Rabatel et al., 2008).

The SMB can be estimated without any required fieldwork as several python scripts, such as the Open Global Glacier Model (OGGM) (Marzeion et al., 2012), are used as a physical approach. Alternatively, a python script called ALPGM provides a non-linear method based on AI technics (Bolibar, 2020).

3.3 Correlations between meteorological data and Folgefonna features

The sensitivity of the glacier's mass balance to climate change is widely recognized (Haeberli, 1995). Indeed, several studies have shown the influence of the climate on glaciers' mass balance.

The correlation coefficient between the North Atlantic Oscillation (NAO) and the Ålfotbreen glacier's mass balance is estimated at $r^2=0.51$. The correlation index between NAO and winter precipitations (from December to March) from 1864 to 1995 in western Norway is $r=0.77$ (Nesje et al., 2000). This proves that NAO has a direct influence on precipitations in Norway.

This work uses only precipitations, temperatures and wind statistics. The purpose is to determine which climatic parameters or climatic parameters ratio has the highest correlation coefficient with glacier features (glacier area, ELA, volume or mass).

For the projection of Folgefonna, a script named Open Global Glacier Model (OGGM) is used (described in part 4.4). However, this method requires climatic data. As there is high future climatic uncertainty, four different scenarios were chosen: RCP 2.6 – 4.5 – 6.0 – 8.5, according to the IPCC(2021):

- **RCP 2.6** is a stringent pathway, requiring carbon dioxide emissions to decline as of 2020, reaching zero by 2100 and halving current methane emissions. This would keep the global temperature increase below 2 °C by 2100.
- **RCP 4.5** is an intermediate scenario, requiring carbon dioxide emissions to start declining by approximately 2045 and reach roughly half of the levels of 2050 by 2100, Methane emissions must also stop increasing by 2050. The goal is to keep the global temperatures from rising above 2°C to 3°C.
- **RCP 6.0** is a scenario where the emissions peak around 2080. The temperature would increase between 3°C and 4 °C.
- **RCP 8.5** is the worst-case climate change scenario, where the emissions are neither restricted nor reduced.

Chapter 4

Methodology and Data

In this chapter, the data⁴ and methods used in this work are given.

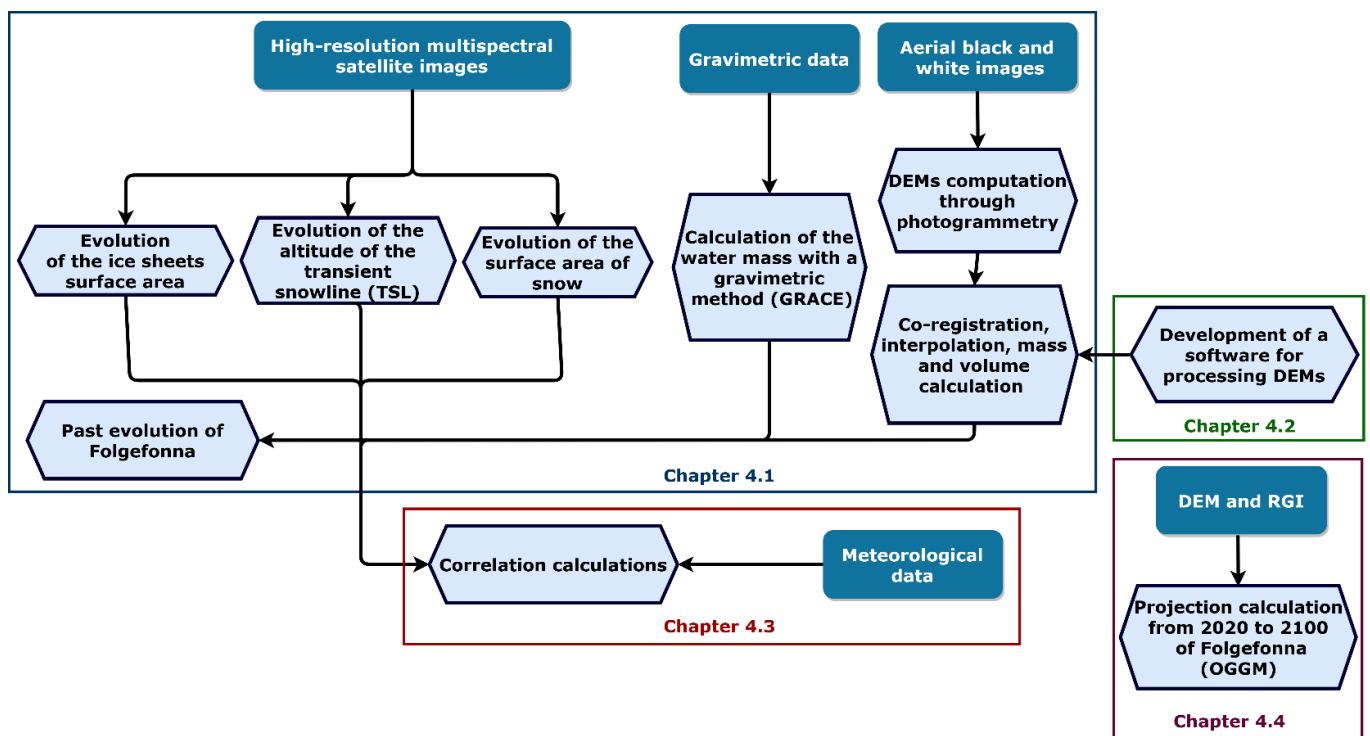


Diagram 4.1: General presentation of the methods

4.1 Historical evolution of Folgefonna with remote sensing

This section analyzes the evolution of Folgefonna during the last 80 years with remote sensing methods. As presented in Diagram 4.1, several elements were calculated in parallel:

- Ice sheet surface area
- Equilibrium Lines Altitude
- Snow area
- Volume evolution
- Mass evolution
- Water mass with GRACE

⁴ All geographic data was projected in World Geodetic System 1984 (WGS84), UTM zone 33N.

4.1.1 Evolution of the glacier area with satellite imagery

4.1.1.1 General presentation

The evolution of Folgefonna was calculated starting from 1959, given that before then, the data for Folgefonna is too noisy to provide satisfying results. The most significant advantage of this method is the free and highly recurrent data access. These multispectral images are taken from satellites such as Landsat or Sentinel satellite missions. It is one of the easiest methods to monitor the evolution of a glacier with remote sensing.

Optimally, the images should be taken on the day of the year with the lowest snow coverage (generally in the end of the ablation season, in the end of the summer). Diagram 4.2 illustrates the process of glacier area computation.

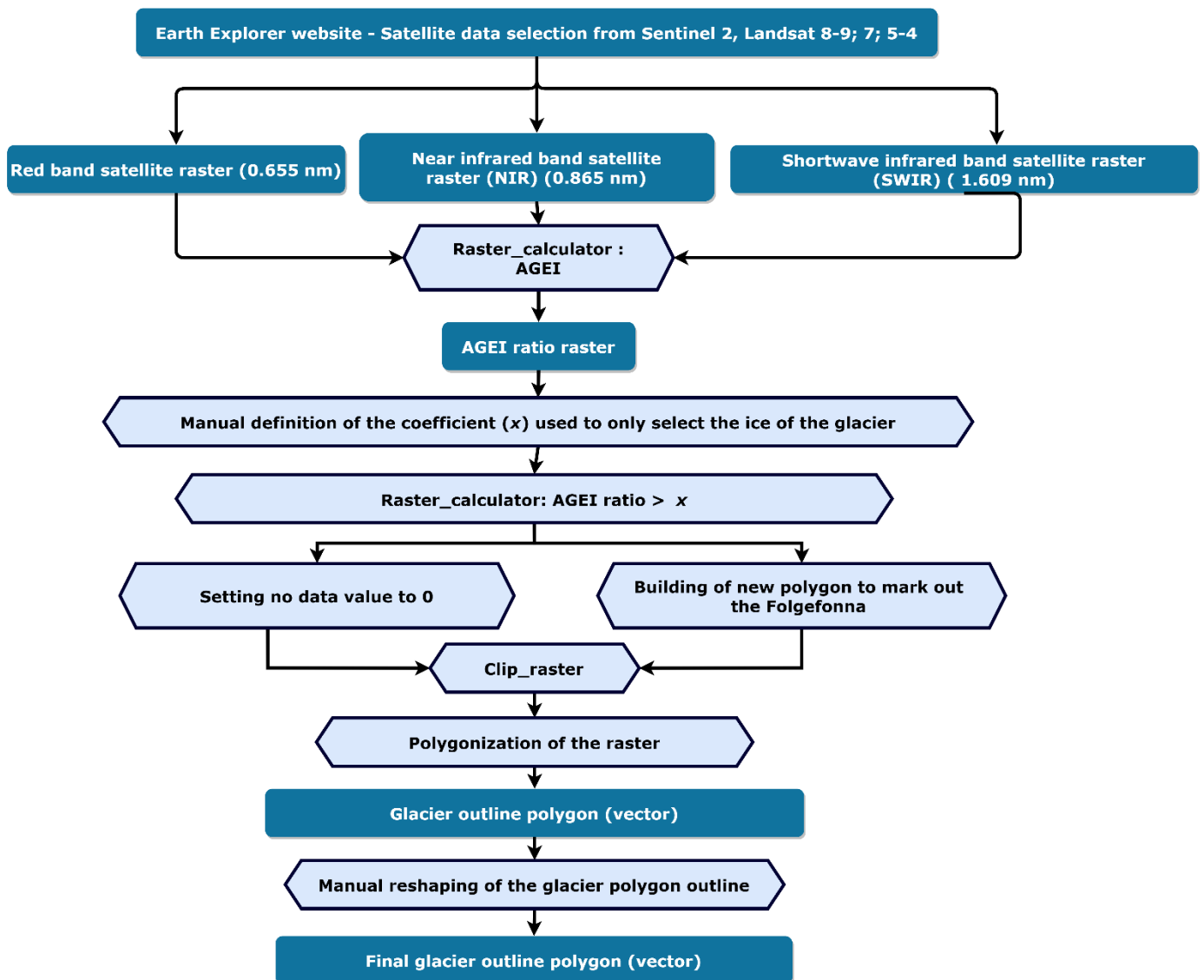


Diagram 4.2: Presentation of calculation process to obtain the glacier area from multiband satellite imagery

4.1.1.2 Collection of multispectral satellite imagery

The first step in monitoring the evolution of glacier areas is choosing which types and which satellite mission(s). The satellite providing free imagery with the highest resolution since 2012 is Sentinel-2 with a 10m resolution⁵ (for the Regions Of Interest (ROI)). As of 2012, Sentinel-2 satellite multispectral images were therefore used. They were downloaded on the EarthExplorer's website (USGS), where the images are free of access and are already orthorectified.

The second step is the selection of suitable images, as snow and clouds can obstruct the image (Racoviteanu et al., 2009). All images were selected between August and October due to their availability and quality.

- For before 2016, the glacier area is calculated using imagery from Landsat 5 TM, 7 ETM+ and 8, with a ground resolution of 30m. For Landsat 5, the bands 3,4 and 5 are used; for Landsat 7, the bands 4 and 5; for Landsat 8, the bands 5 and 6 (Table 4.2).
- For after 2016, the calculations use imagery from Sentinel 2, with a ground resolution of 10m. The bands 4, 8, and 11 are used.

4.1.1.3 Classification

Near Infrared (NIR) and ShortWave InfraRed (SWIR) bands are used to determine the glacier layer. Several methods were tried, including the maximum-likelihood classification, Normalized Difference Snow Index (NDSI), Red/SWIR, NIR/SWIR and Automated Glacier Extraction Index (AGEI). Each of method presents its advantages and disadvantages.

The AGEI ratio is used as it is the most accurate for classifying the glacier's edge mixed pixels (Zhang et al.,2019). Indeed, one of the main problems is the presence of snow on and beside the glacier.

$$AGEI = \frac{\alpha \cdot DN_{Red} + (1-\alpha) \cdot DN_{NIR}}{DN_{SWIR}} \quad (4.1)$$

Where $\alpha \in [0,1]$ is a weighted coefficient, an increment of 0.1 between 0.1 and 0.9 is set to optimize the algorithm.

The classification is partly automated with ArcGIS. Two model builders were built. The first one (Appendix A.1 – A) is used to calculate the AGEI ratio. The second one (Appendix A.1 – B) is used to convert the AGEI ratio raster layer into a polygon shapefile.

4.1.1.4 Manual verification

The classification can contain several imprecisions depending on the quality and snow coverage of the satellite images. Manual verification is crucial to confirm the glacier area. The shapefile is validated if the glacier area shapefiles perfectly match the visible glacier outline on the raster layer (AGEI raster). Otherwise, the shapefiles have to be readjusted. When the snow coverage is low, typically at the beginning of autumn, one can easily visually distinguish snow-covered grounds from the glacier. However, when the snow coverage is high, the human eye cannot accurately differentiate one from the other, resulting in lower accuracy.

⁵ The resolution depends on the bands.

4.1.1.5 Area correction with the slope

Folgefonna has varying degrees of steepness, a low slope in the middle of the ice sheets and steeper slopes on the peripheric tongues such as Bondhusbreen or Bondhusbrea. ArcGIS functions (such as the “Surface toolset”) were used to account for the glacier’s slope.

4.1.1.6 Uncertainties

The three main uncertainties for glacier area calculations are the following:

- **Geo–physical uncertainties:** Folgefonna has three ice caps with varying topography. The advantage is the low debris, as they are focused on the glacier’s tongues. Nevertheless, the main geophysical elements which increase the uncertainty are clouds, snow, water, shadows, footprint size, and sampling.
- **Acquisition uncertainties:** During data acquisition, the corrections from the slope analysis, roughness, and radar penetration are the main sources of uncertainties.
- **Processing uncertainties:** The Manual digitizing statistical filtering and bias corrections constitute the primary source of uncertainties.

Method	Threshold value	Resulting ice area (km ²)	Estimated processing time	Over-classified ice area (%)	Under-classified ice area (%)	Estimated accuracy (%)
The control						
A. Hand Digitized		58.0	12 hours	n/a	n/a	~ 99.8
Supervised techniques						
B. Maximum Likelihood		52.0	18 min	0.4	9.4	90.2
C. Minimum Distance		43.2	15 min	0.0	24.5	75.5
D. Parallelepiped		49.8	15 min	0.0	12.9	87.1
*E. Spectral Angle Mapper (SAM)		57.7	15 min	2.1	1.2	96.7
Unsupervised techniques						
F. ISODATA		56.7	2.25 min	4.4	5.1	90.6
Fuzzy classification techniques						
G. Linear Unmixing	>0.2	58.2	16 min	5.8	4.0	90.2
H. MTMF	>0.0	47.5	16 min	1.0	17.9	81.1
I. SFF - Scatterplot vs. RMS		46.8	20 min	0.1	18.2	81.7
J. SFF	>0.5	49.8	18 min	0.5	13.3	86.2
K. MNF - PPI - MTMF - Scatterplot		47.0	2 hours	4.3	22.0	73.7
L. MNF - PPI - Linear Unmixing		49.6	2 hours	3.2	16.5	80.3
Band math and threshold techniques						
M. 3/5 Ratio	>4.0	52.6	10 sec	0.5	8.5	91.0
*N. 4/5 Ratio	>3.3	53.1	10 sec	0.5	7.5	92.0
*O. NDSI	>0.5	54.6	11 sec	0.9	5.2	93.9
P. MNF Transform	>10	52.2	1 min	0.0	8.7	91.3
Mean:		51.35	69 min	2.0	13.2	84.8

^aWhere applicable.

^bAsterisks indicate the three methods recommended for future studies (E, N, and O).

Table 4.1: Measured accuracy of the different glacial mapping methods from Landsat TM data (credit: Albert, 2002)

The Landsat TM table (Table 4.1) presents the measured accuracy of different methods for glacial mapping. The error associated with the NDSI technique is 6.1%; it is assumed to be the same for AGEI. This percentage was therefore applied to all glacier area calculations. However, the error is likely lower with a manual correction of each glacier outline.

4.1.2 Evolution of the Equilibrium Line Altitude

The method used to calculate the evolution of ELA is presented below.

The beginning of the method is the same as presented in chapter 4.1.1 until the final calculations named “Glacier outline polygon” (Diagram 4.3). However, the AGEI ratio calculation can be cunningly different from the ELA computation. In fact, for the glacier outlines, the glacier needs to be differentiated from the rocks; while the ELA aims to discern the glacier from the snow. The step to increase the contrast differs slightly.

The contrast is increased with one of the two following equations:

$$C_1 = \frac{R \cdot NIR}{SWIR} \quad (4.2)$$

$$C_2 = \frac{NIR^2}{SWIR} \quad (4.3)$$



Figure 4.1: Formula 4.2 applied to Sentinel 2 data of 2015

4.1.2.1 ELA calculation

The ELA is an essential feature to compute as there is a correlation between ELA and the glacier mass balance. The average ELA calculation was completed with the ArcGIS Pro software. One “model builder” was created to compute all the processes in a single run. The first step is to clip the Region Of Interest (ROI) as four regions were studied: Folgefonna (entire glacier), Søndre Folgefonna, Midtre Folgefonna, and Nordre Folgefonna. Once the region is clipped, only the contour lines of the polygons are kept, and the “Polygon_to_line” ArcGIS function is used. Subsequently, the profiles of a reference DEM are computed, and two different DEMs are used. From 1985 to 2015, then 2013 Høydedata DEM was chosen. For the period 2015 to 2021, the 2017 Høydedata DEM was taken as a reference. Finally, to calculate the elevation profiles of ELA, the “Stack_profile” ArcGIS function is computed.

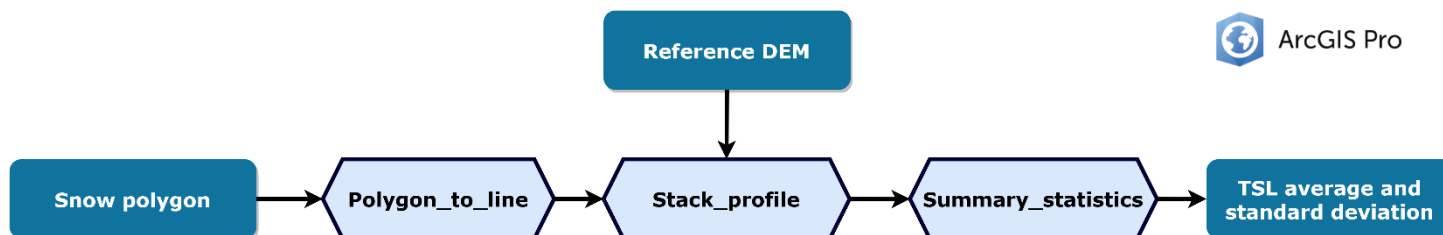


Diagram 4.3: Calculation method to determine the altitude of TSL average (ELA) and associated standard deviation

4.1.3 Snow coverage

The snow coverage evolution corresponds to the same periods as ELA or the glacier area calculations. This means that for each year, the snow coverage is optimally calculated on the day at the end of the ablation season.

The snow coverage evolution is calculated during the ELA processing (section 4.1.2). However, the uncertainties are computed using the same method defined in the glacier area process (section 4.1.1.6).

4.1.4 DATA synthesis of glacier area, ELA and snow coverage

The table below presents the data used to calculate the glacier area, ELA and snow coverage.

Date	Satellite	Sensor	Bands	Resolution	Revisit interval
2021-08-26	Sentinel-2	MSI	Bands 4,8 and 11	B4: 10m ; B8: 10m ; B11: 20 m	5 days
2020-09-17	Sentinel-2	MSI	Bands 4,8 and 11	B4: 10m ; B8: 10m ; B11: 20 m	5 days
2019-07-16	Sentinel-2	MSI	Bands 4,8 and 11	B4: 10m ; B8: 10m ; B11: 20 m	5 days
2018-09-04	Sentinel-2	MSI	Bands 4,8 and 11	B4: 10m ; B8: 10m ; B11: 20 m	5 days
2017-09-16 ; 2017-08-27	Sentinel-2	MSI	Bands 4,8 and 11	B4: 10m ; B8: 10m ; B11: 20 m	5 days
2016-09-05	Sentinel-2	MSI	Bands 4,5 and 8	B4: 10m ; B5: 10m ; B8: 20 m	5 days
2015	Sentinel-2	MSI	Bands 4,5 and 8	B4: 10m ; B5: 10m ; B8: 20 m	5 days
2014-09-15	Landsat-8	OLI	Bands 5 and 6	B5: 30m ; B6: 30m	16 days
2013-10-14	Landsat-8	OLI	Bands 5 and 6	B5: 30m ; B6: 30m	16 days
2011-09-16	Landsat 7	ETM+	Bands 4 and 5	B4: 30m ; B5: 30m	16 days
2010-09-10	Landsat 7	ETM+	Bands 4 and 5	B4: 30m ; B5: 30m	16 days
2008-07-28	Landsat-4-5	TM	Bands 3, 4 and 5	B3: 30m ; B4: 30m ; B5: 30m	16 days
2006-10-11	Landsat-4-5	TM	Bands 3, 4 and 5	B3: 30m ; B4: 30m ; B5: 30m	16 days
2004-08-10	Landsat 7	ETM+	Bands 4 and 5	B4: 30m ; B5: 30m	16 days
2005-10-16	Landsat-4-5	TM	Bands 3,4 and 5	B3: 30m ; B4: 30m ; B5: 30m	16 days
2002-09-22	Landsat-4-5	TM	Bands 3,4 and 5	B3: 30m ; B4: 30m ; B5: 30m	16 days
1998-10-05	Landsat-4-5	TM	Bands 3,4 and 5	B3: 30m ; B4: 30m ; B5: 30m	16 days
1994-08-23	Landsat-4-5	TM	Bands 3,4 and 5	B3: 30m ; B4: 30m ; B5: 30m	16 days
1995-09-18	Landsat-4-5	TM	Bands 3,4 and 5	B3: 30m ; B4: 30m ; B5: 30m	16 days
1993	Landsat-4-5	TM	Bands 3,4 and 5	B3: 30m ; B4: 30m ; B5: 30m	16 days
1992-10-04	Landsat-4-5	TM	Bands 4 and 5	B4: 30m ; B5: 30m	16 days
1987-09-28	Landsat-4-5	TM	Bands 3,4 and 5	B3: 30m ; B4: 30m ; B5: 30m	16 days

Table 4.2: Presentation of the data used to compute the glacier area, ELA and snow coverage

4.1.5 Photogrammetric DEM calculation

This section explains the methods of processing to compute DEMs from photographs. This section was carried out during the internship at the University of Bergen.

4.1.5.1 Datasets and software

All the DEMs created in this work were built through aerial photographs taken from airplanes. These images are scanned black and white photos from film cameras containing 255 shades of grey. Most of this data was bought on the Flyfoto Høydedata website – where the first overview pictures are dated 1937. Table 4.3 presents the features of the images.

Year	Number of Images	Source of data	H.o.h.	Calibration report
1937	16	Norges Geografiske Oppmåling (NGO)	unknown	No
1953	33	NGO (bought on Flyfoto Høydedata website)	4970m	No
1962	94	NGO (bought on Flyfoto Høydedata website)	3600m	Yes
1981	37	NGO (bought on Flyfoto Høydedata website)	4700m – 5300m	Yes

Table 4.3: Presentation of image dataset used for DEM calculation

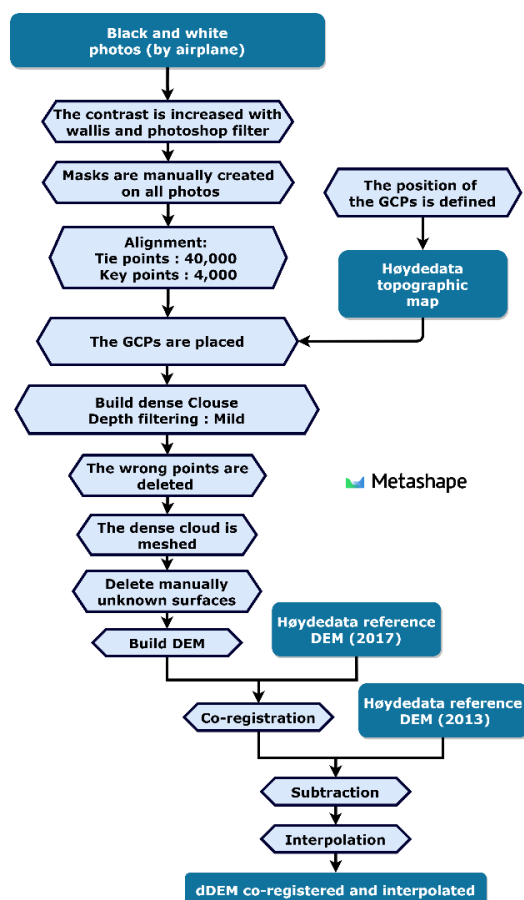


Figure 4.2: Presentation of photogrammetry processing for black and white

The Agisoft Metashape Professional software is used to compute the DEMs.

4.1.5.2 Pre-processing of imagery

The scanned black and white images often have a too low contrast on the glacier to yield satisfying results. The natural contrast on the glacier's surface can induce problems during the dense cloud process. When the contrast is too low, getting enough points over the glacier to provide high DEM quality is impossible (section 4.1.5.7). The contrast is particularly low when the sunlight is directly or indirectly reflected in the camera's lens.

In this case⁶, pre-processing the images significantly improves the photogrammetry process. This section presents the processing method for such image enhancements.

4.1.5.2.1 Photoshop pre-processing

All images are coded in eight bits, meaning there are only 255 colors. The Photoshop software is used to increase the contrast and find numerous tie points over the glacier. It allows for doubling the number of colors on each photo. The

⁶ For black and white photos

“curve” function in Photoshop permits modification of the colors of images.

After that, a polynomial function is used (Figure 4.3). Doubled colors mean that one grey level refers to two different objects; for example, the 100 grey level refers to snow and rock on the same image.

Applying the same filter⁷ on each photo of the same series is necessary to obtain homogenous colors. In Metashape, the color pixels are compared to align the cameras and build dense points clouds.

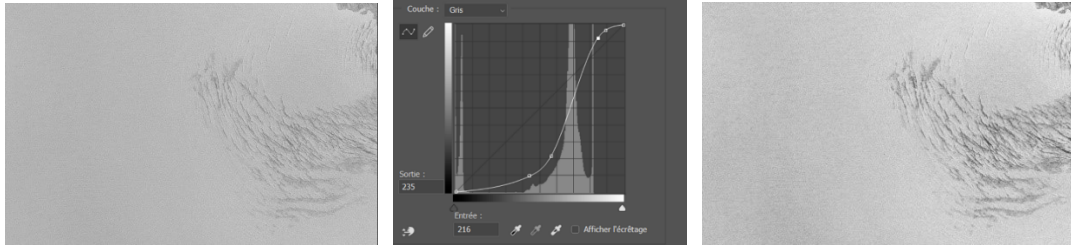


Figure 4.3: Raising image contrast with Photoshop

4.1.5.2.2 Wallis filter

The Wallis filter script (Appendix A.5) allows for locally modifying the contrast and brightness on the glacier. This cannot be done with Photoshop. Minor details on the glacier’s surface need to be visible to obtain maximum points over the glacier during the “Dense_cloud” processing in Metashape.

Figure 4.4 displays the results of the Wallis filter computation on a portion of black and white photos of Folgefonna. A clear improvement is visible, particularly in the visibility of the structure of the snow (bumps).

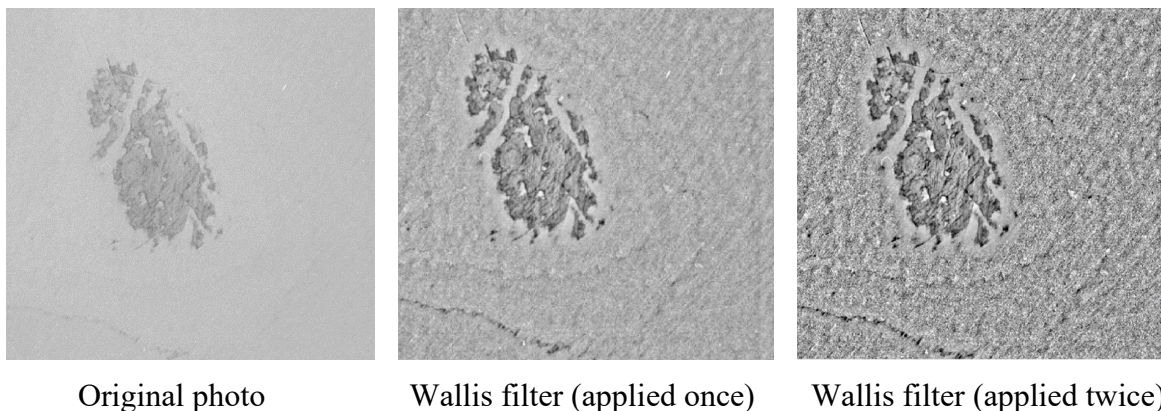


Figure 4.4: Application of the Wallis filter on a low contrast black and white photo of a part of Folgefonna

⁷ The “Treatment_by_lot” Photoshop function applies the transformation to an entire series of photos.

4.1.5.3 Masking

The first step in Agisoft Metashape is to mask all sides of the images. Only one or two masks are built for perfectly scanned series and where the selected images have a high reflectance. The objective is to easily distinguish the difference between the landscapes and the frame of the image. Once seamlessly adjusted, the mask is exported and applied to all other photos with the exact pixel dimensions. The mask must be individually applied to the photos with different pixel dimensions – an extensive process.

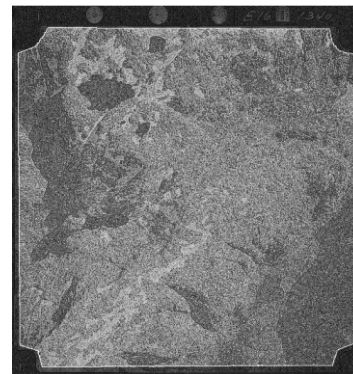


Figure 4.5: Black and white photography of the Folgefonna with masked frame (1962)

4.1.5.4 Reduction of the distortion

Photographs may contain some distortion effects (section 3.1.3.2), which increases the final uncertainty⁸. As shown in Table 4.3, there are only reports for 1962 and 1981.

For 1962, an explicit calculation was performed using geometry software with a specific script (Appendix A.4, geometric transformations).

The coefficients are directly inserted in the “Camera_Calibration” pane (in Metashape).

4.1.5.5 Alignment

The alignment of cameras is a fundamental step in photogrammetry.

On Metashape, several methods were tried to align the photos. The most efficient method used for all series is the following:

The accuracy is set to the highest. The exclude stationary tie points, “guided image matching and adaptive camera model fitting” option is ticked. Masks are applied to the key points, and the number of key point limit per Megapixel is inputted to be 6,000, and the number of tie point limit is fixed at 5,000 (Metashape manual, 2021).

Once the masks are created, the cameras can be aligned. For this step, the “align_photos” function is used. This script finds key points on each image, which are directly utilized to align the cameras with the parallax phenomena. Then, the tie points are found. Tie points correspond to common key points between several images.

The “Adaptative camera model fitting” option is ticked. This option enables the automatic selection of the camera parameters to be included in adjustments based on their estimated reliability (radial distortion).

⁸ The purpose is to observe volume and mass evolution.

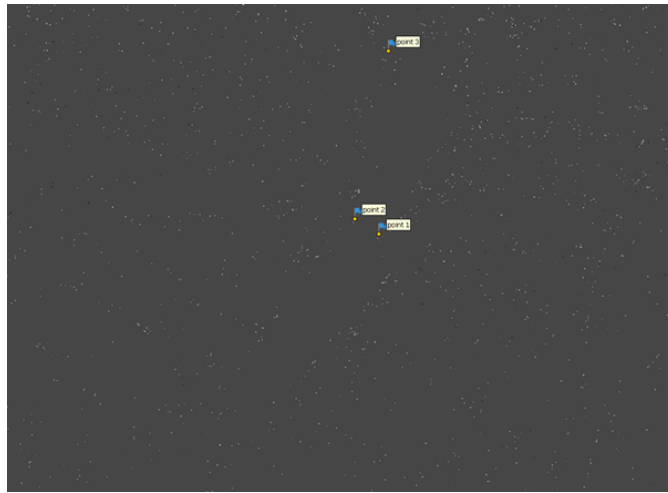


Figure 4.6: Tie points cloud after the alignment step for 1962 – 3 Ground Control Points (GCPs) are placed.

4.1.5.6 Ground Control Points (GCPs):

Once the photos are aligned, markers are placed on the images. This allows finding their coordinates on the Høyedata website. The Norwegian vertical reference frame NN2000 was chosen for altimetric data (Lysaker et al., 2020). Markers with coordinates are called Ground Control Points (GCPs) or control points (in Metashape). These points are used as references to control the model and camera calibration. The Sfm point clouds only require three points to scale and georeference (Mölg and Bolch, 2017). However, horizontal and vertical accuracy grows as the number of GCPs used increases (Agüera–Vega et al., 2017).

Figure 4.7 confirms that the accuracy is linked to the number of GCPs with a logarithm trend. According to the same study:

With 15 GCPs, the Root Mean Square Elevation (RMSE) is the following: $RMSE_x = 3.3 \pm 0.346\text{cm}$; $RMSE_y = 3.2 \pm 0.441\text{cm}$; $RMSE_z = 5.8 \pm 1.21\text{cm}$.

With 20 GCPs: $RMSE_x = 3.2 \pm 0.346\text{cm}$
 $RMSE_y = 3.1 \pm 0.218\text{cm}$; $RMSE_z = 4.7 \pm 0.86\text{cm}$.

Optimal results for $RMSE_x$, $RMSE_y$, and $RMSE_z$ are reached for 15 GCPs. Finally, at least 15 GCPs are placed for each series, and each marker must have at least two placed projections on aligned photos (Metashape manual, 2021).

In this step, several checkpoints⁹ are also placed to control the DEMs generated at the end of the simulations. Then, the camera alignment is optimized with the “optimize camera” function. The objective of this function is to adjust camera alignment with all available measurements and corresponding accuracies, GCPs coordinates, scale bar distances, image projections of tie points, and markers (Metashape manual, 2021).

If all cameras are not aligned in the previous step, another “chunk” is created. This is where all unaligned cameras are dropped, and a new alignment process is launched. If all cameras are successfully aligned, GCPs are placed. Once the optimization is launched, both “chunks” are merged into a new one. The “Camera_optimization” function is then relaunched.

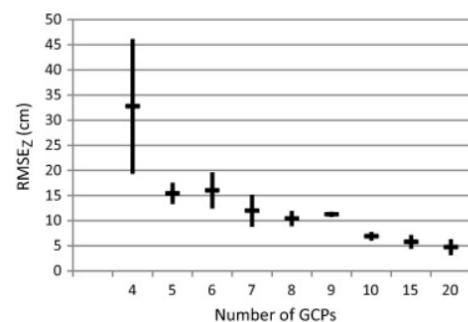


Figure 4.7: $RMSE_z$ [cm] mean values vs number of GCPs. Extremum of the bars indicates standard deviation – source: Agüera–Vega et al., 2017

⁹ In Metashape, they are markers without coordinates, contrary to control points.

4.1.5.7 Dense cloud

Once all GCPs are placed, a dense cloud is built through the “Build_dense_cloud” function. The depth filtering mode is always set on aggressive or moderate. This parameter is adjusted according to the quality of the final DEM. Concretely, when there are many object characteristics, the dense cloud processing works flawlessly (i.e. stable ground). However, in places with a low concentration of object characteristics (i.e. snow-covered glaciers), the dense cloud can be thick, and an aggressive or moderate depth filter might remove all the points in this section.

The accuracy is always set on “highest”, which can cause a lengthy calculation time.

Note: The dense clouds presented in Figure 4.8 are in the exact location as in the tie points file (Figure 4.6).

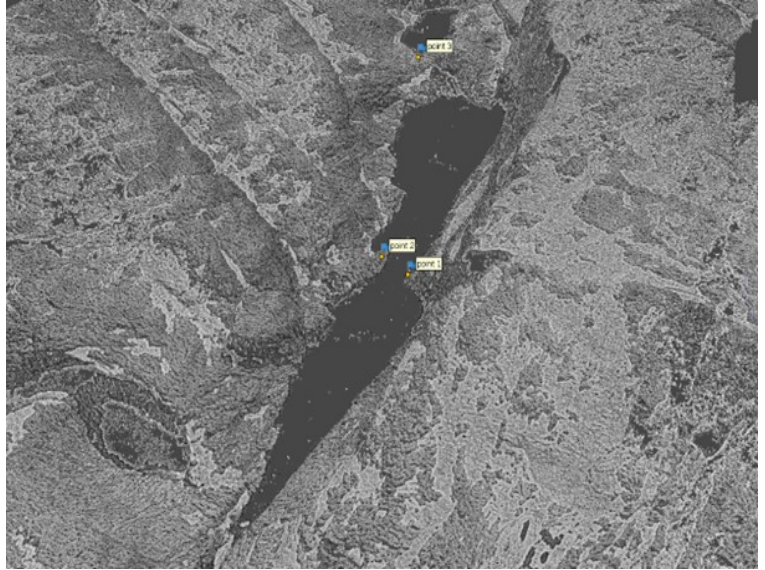


Figure 4.8: Dense cloud generated from the tie points cloud presented in figure 4.6. (year: 1962)

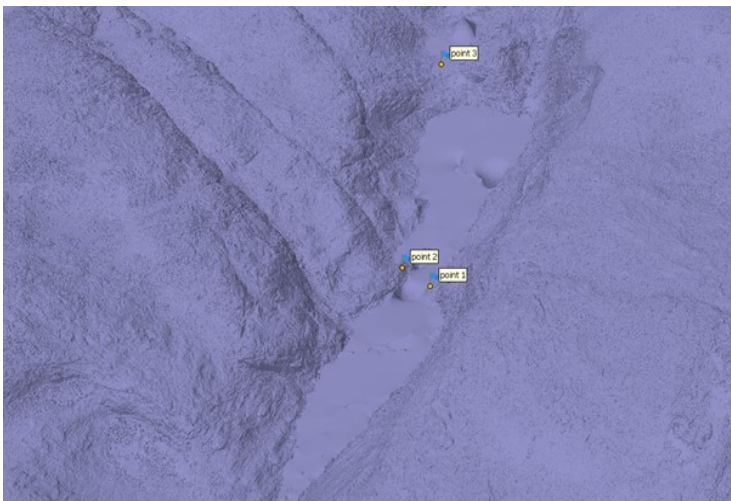


Figure 4.9: 3D model generated from the dense cloud presented in figure 4.7 (year:1962)

4.1.5.8 3D model generation

Once the dense cloud is produced, it is often necessary to manually remove faulty point locations¹⁰– an extensive process.

Then, a 3D model is created from the dense cloud through the “Mesh” function. Finally, the DEM is directly created from the 3D model.

¹⁰ Removing the points before the mesh processing is more satisfactory.

4.1.6 Formerly generated DEMs

Several DEMs of Folgefonna have already been created. In this work, they are used to complete the DEMs produced by photogrammetry (section 4.1.5), principally to obtain high-quality references for the co-registration and interpolation (section 4.1.7) but also to increase the data density.

4.1.6.1 LiDAR DEM computation

4.1.6.1.1 DATA

DEMs can directly be calculated using electromagnetic waves (RaDAR) or light waves (LiDAR) (section 3.1.4.1). In this study, LiDAR is predominantly used as it is more accurate than RaDAR, thanks to the deep snow penetration of the electromagnetic waves.

Two DEMs were downloaded on the Høydedata website. One of them was created in 2013 with a one-meter resolution. The second one was built in 2017 with a half-meter resolution. The quality is excellent as the data was collected using an aerial LiDAR. The data was downloaded in a small area section, and the function “mosaic_to_raster” was used to build the DEMs.

The 2017 DEM does not cover the entire surface of the three ice caps. Nevertheless, a considerable part of the stable ground located around the glacier was computed, making it particularly interesting to use as a reference in the co-registration.

Another DEM created by LiDAR from 2007 is used. However, the resolution is relatively low (30m). It is a three files layer of Søndre, Midtre and Nordre Folgefonna. To complete a single DEM, the co-registration of each one was necessary before the assembling step.

4.1.6.2 Satellite photogrammetry

ArcticDEM is a public-private initiative to automatically produce a high-resolution digital surface model of the arctic using photogrammetric methods from optical stereo imagery (Porter et al., 2018). The main inconvenience is that ArcticDEM only provides DEMs above 60° N. As this latitude line crosses Folgefonna, the south of Søndre Folgefonna is not covered.

For Folgefonna, two DEMs are available (2013 and 2017). These DEMs were created from satellite imagery and have a lower resolution than the aerial photogrammetric method.

4.1.6.3 Ancient maps

Aerial LiDAR allows for building high-quality DEMs; however, this method is relatively recent. An ancient topographic map is used to have older DEMs without using photogrammetry. One DEM from 1959 is calculated from a 1959 contour lines layer. This contour lines layer was built from aerial images. The “topo to raster” function on ArcGIS converts the contour lines layer into a DEM layer to construct the final DEM.

4.1.6.4 DATA synthesis

The below table offers a summary of the DEMs presented in this chapter.

Date	Origin of data	Resolution [m]	ArcGIS function used
1959	1959 contour lines		Topo_to_raster
2007	LiDAR	30	Co-registration, next Mosaic_to_new_raster
2013-08-22 to 2013-09-20	Høyedata – NVE	1	Mosaic_to_new_raster
2014-05-31 to 2014-06-18	ArcticDEM	2	Mosaic_to_new_raster
2017	Høydedata – NVE	0.5	Mosaic_to_new_raster
2017-05-15 to 2017-05-19	ArcticDEM	2	Mosaic_to_new_raster

Table 4.4: Presentation of formerly completed Folgefonna DEMs and the applied post-processing

4.1.7 Co-registration, bias corrections and interpolations of DEMs

The two most critical steps of DEM processing are the co-registration and the interpolation. The diagram below simplifies the necessary DEM types and how their process.

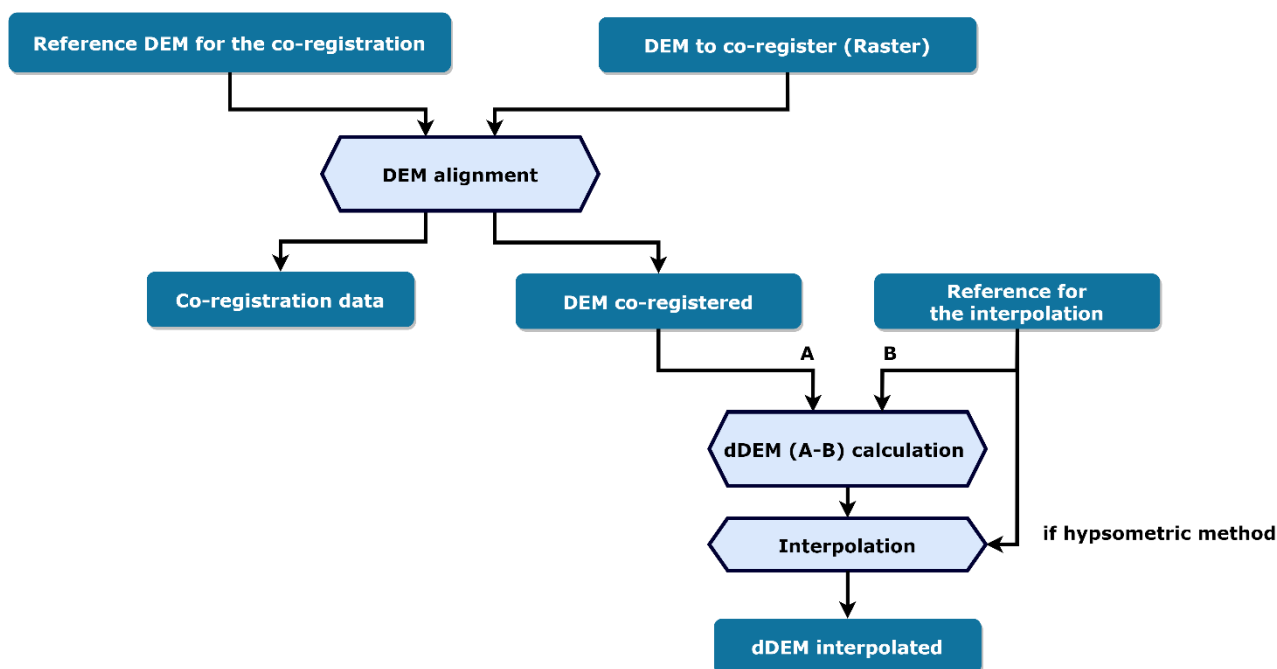


Diagram 4.4: Simplified processing for DEM alignment and interpolation

4.1.7.1 Co-registration and bias corrections

To compare the DEMs, a co-registration of each of them is necessary. This aligns the stable ground of each DEM by applying translational and rotational shifts. Using a reference DEM, the shifts are computed, and the slave DEM¹¹ is corrected.

Four methods are used:

- Nuth and Kääb algorithm
- Iterative Closest Point (ICP)
- Deramp
- Vertical Offset

These methods are presented in the literature review (chapter **Error! Reference source not found.**). Several combinations of these four methods are used by comparing the Normalized Median Average Deviation (NMAD). This step was performed using the software developed in this work (*method*: section 4.2, *results*: section 5.2).

This step requires masking unstable ground such as glaciers, lakes or rivers¹². A shapefile is used to cover the glacier for the execution of the co-registrations. The glacier area calculated in the glacier area computation (section 4.1.1) serves as a basis for this computation.

4.1.7.2 Interpolation

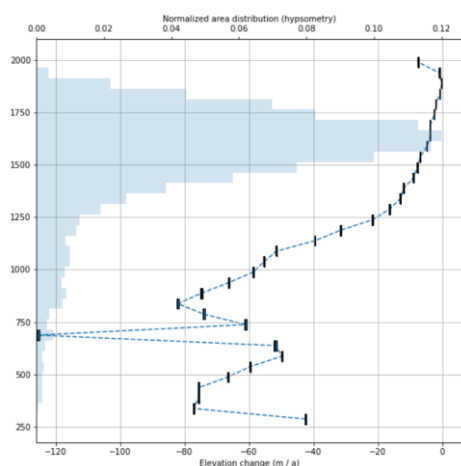


Figure 4.10: Hypsometric distribution of the glacier and elevation change as a function of altitude.

The interpolation is particularly necessary for the DEMs calculated using photogrammetry. Due to voids on each DEM induced by a poor contrast (section 4.1.5.7), interpolating these voids on the glacier is essential to compare each DEM on the three ice caps. The literature review (section 3.1.5.2) presents several existing interpolation methods. The local hypsometric interpolation python script is predominantly used (Mannnerfelt et al., 2021). This method assumes a relationship between the elevation and the elevation change, as glaciers have lost the highest ice quantity in the lower regions, while the higher altitudinal regions are less impacted. This approach estimates change gradients using a linear or polynomial model with a reference DEM and the DEM to co-register.

¹¹ DEMs requiring co-registration

¹² The co-registration is presented in the Eagloo software section (*method*: section 4.2, *results*: section 5.2)

4.1.8 Evolution of Folgefonna's geophysical features

The final stage is to infer the historical evolution of Folgefonna in the last 80 years. Four geophysical features are calculated:

- Volume change
- Mass change
- Meter water equivalent
- Contribution to sea level rise

The first objective is to calculate the volume change between two DEMs of the exact location from two different dates. There is a latest DEM and earliest DEM. These calculations were conducted with Eagloo (*method*: sections 4.2; *results*: section 5.2).

4.1.8.1 Volume change

To calculate the difference in volume between two DEMs, one must first subtract the earliest from the latest DEM. This is called a dDEM.

$$dDEM' = DEM_{latest} - DEM_{earliest} \quad (4.4)$$

Where DEM_{latest} is the latest DEM, $DEM_{earliest}$ is the earliest DEM and $dDEM'$ is the elevation change including glaciers and stable ground.

Once the $dDEM'$ is computed, the stable ground has to be removed. The associated glacier outline shapefile is used to mask the external ground of glaciers (trees, rock, lakes, etc.). These glacier outline shapefiles are the results of the glacier area calculation from section 4.1.2. For the DEMs calculated by photogrammetry, the glacier outline shapefiles are computed using orthophotos. The final dDEM is calculated with the following equation:

$$\forall x \in C, \forall y \in R, dDEM = \begin{cases} dDEM_{x,y} = dDEM'_{x,y}, & \text{if } Glacier_{outline_{x,y}} = 1 \\ dDEM_{x,y} = Null, & \text{if } Glacier_{outline_{x,y}} = 0 \end{cases} \quad (4.5)$$

Where C is the number of columns of $dDEM'$, R is the number of rows of $dDEM'$, and $dDEM$ represents the elevation change raster of the analyzed glacier without stable ground. $dDEM_{x,y}$ is the elevation change value for the pixel located on column x and row y .

The resolution must be known to calculate the final volume change. For each DEM computed, pixels have the same length and width (simplification of the calculation).

$$V_{dDEM} = \sum_{x=0}^C \sum_{y=0}^R dDEM_{x,y} \times Resolution^2 \quad (4.6)$$

Where V_{dDEM} is the volume associated with the dDEM raster, and $Resolution$ is the resolution associated with this raster¹³.

4.1.8.2 Mass change

Once the volume change is computed (V_{dDEM}), the mass change can be calculated.

Multiplying the volume change (V_{dDEM}) by the ice density coefficient converts the difference in glacier volume into the difference in glacier mass. As presented in the literature review (section 3.1.5.3), ice density is primarily heterogeneous based on depth and time.

Given that the estimation of the conversion factor of glacier volume change into glacier mass change is challenging, constant ice density is assumed on all glaciers and their entire surface.

¹³ Assuming that the pixels are square – same width and length resolution.

As described by Huss in 2013, considerable variability affects the accuracy of the widely used geodetic method for determining glacier mass balance. It is recommended to use a factor of $850 \pm 60 \text{ kg/m}^3$ for periods extending five years. As all compared DEMs are separated by at least four years (there is only one period under five years), this coefficient, along with its associated uncertainty, is used.

Multiplying the volume change by the ice density calculates the mass change.

$$M_{dDEM} = V_{dDEM} \times \rho_{ice} \quad (4.7)$$

Where ρ_{ice} is the ice density, and M_{dDEM} is the mass variation of the dDEM.

4.1.8.3 Meter Water Equivalent

Meter Water Equivalent (m.w.e.) indicates the average lost or gained water thickness on the glacier. It is calculated as follows:

$$MWE_{dDEM} = \frac{M_{dDEM}}{\rho_{water} \times S_{dDEM}} \quad (4.8)$$

Where MWE_{dDEM} is the number of Meter Water Equivalent associated with the dDEM, ρ_{water} is the water density (1000 kg.m^{-3}) and S_{dDEM} is the glacier area.

4.1.8.4 Contribution to sea-level rise

The contribution to sea-level rise measures the rise in sea level caused by the ice melting. Knowing the oceans' surfaces is necessary for calculating this ratio.

$$CSLR_{dDEM} = - \frac{M_{dDEM}}{\rho_{water} \times S_{sea}} \quad (4.9)$$

Where S_{sea} is the sea's surface area, and $CSLR_{dDEM}$ is the coefficient of the sea level increase or decrease.

4.1.8.5 Uncertainties

This chapter provides an overview of the calculated uncertainties associated with the volume change, mass change, meter water equivalent and contribution to the rise of the sea-levels.

4.1.8.5.1 Standardized integrated errors on the glacier

This uncertainty is computed from the $dDEM'$ layer. It is based on the assumption of a spatial correlation between slope/curvature and elevation change error. Thus, on stable ground, dDEM' values are associated with errors. Errors on the glaciers are directly calculated from a three-dimensional array file, transcribed in Figure 4.11 (on the right). The Normalized Median Absolute Deviation (NMAD) shows that the error is strongly correlated to the curvature and slope. This correlation is used to calculate the errors.

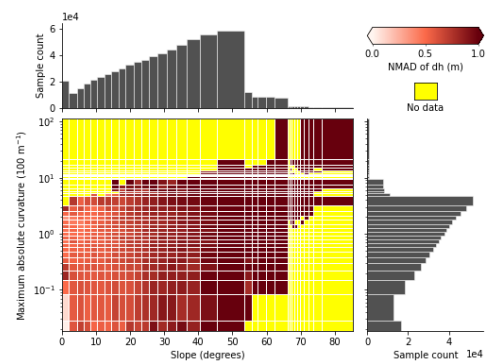


Figure 4.11: Normalized Median Absolute Deviation as a function of the maximum absolute curvature and slope (calculated for Folgefonna)

To calculate the standardized integrated errors on a specific glacier, it is first necessary to standardize error values associated with the stable ground of $dDEM'$ by applying equation 4.10.

$$E'(x, y) = \frac{E(x, y) - \bar{E}}{\sigma_E} \quad (4.10)$$

Where $E'(x, y)$ is the standardized error on the stable ground as a function of latitude and longitude, $E(x, y)$ are the values of $dDEM'$ on the stable ground, \bar{E} is the average value of E , and σ_E is the standard deviation of E .

Standardization is a fundamental process of using the stable ground as a reliable proxy; it allows a stationary variance. Once the standardized errors are computed, slope and curvature are calculated from a reference DEM. The standardized integrated errors calculated as a function of slope and curvature (Figure 4.11) resulting in a three-dimensional array file [curvature, slope, standardized errors]. This is directly used to calculate the spatial error on the glacier. Each pixel on the glacier is linked to a specific curvature and slope, and standardized errors are calculated for each pixel.

Afterward, the standardized integrated error ($\sigma_{\bar{E}'}$) can be calculated as follows:

$$\sigma_{\bar{E}'} = \frac{\sigma_{E'}}{\sqrt{N}} \quad (4.11)$$

Where $\sigma_{E'}$ is the standard deviation, in this case, as a consequence of standardization, $\sigma_{E'}=1$, N is the adequate number of observations derived from numerical integration. N is calculated from the variogram displayed in Figure 4.12, based on the method described in Rolstad et al., 2009.

Once $\sigma_{\bar{E}'}$ is calculated, it is needed to unstandardized this value.

$$E_{\sigma_{\bar{E}'}} = \frac{\sigma_E}{\sigma_{\bar{E}'} + \bar{E}} \quad (4.12)$$

Where $E_{\sigma_{\bar{E}'}}$ is the final uncertainty associated with the $dDEM$ of a specific glacier.

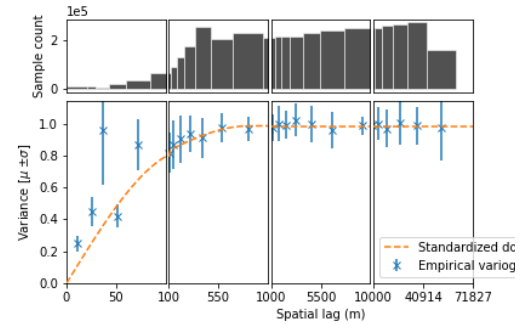


Figure 4.12: Variogram of the sample count standardized

4.1.8.5.2 Final uncertainties

The surface area errors and $dDEM$ must be known for the final uncertainties. Four uncertainties are calculated: volume change, mass change, meter water equivalent, and contribution to sea-level rise. The associated errors are the following:

$$E_{volume} = \left(\frac{E_{\sigma_{\bar{E}'}}}{dDEM} \times \frac{E_{S_{dDEM}}}{S_{dDEM}} \right) \times VC \quad (4.13)$$

Where VC is the volume change, S_{dDEM} is the surface area of the $dDEM$, $E_{S_{dDEM}}$ is the error of the *area*, and E_{volume} is the error associated with the volume change.

$$E_{mass} = \left(\frac{E_{volume}}{VC} + \frac{E_{\rho_{ice}}}{\rho_{ice}} \right) \times MC \quad (4.14)$$

Where MC is the mass change, ρ_{ice} is the density of the ice, $E_{\rho_{ice}}$ is the error of ρ_{ice} and E_{mass} is the error of MC .

$$E_{m.w.e.} = \frac{E_{mass}}{\rho_{water} \times S_{dDEM}} \quad (4.15)$$

Where, ρ_{water} is the density of the water and $E_{m.w.e.}$ is the error of the meter water equivalent.

$$E_{SLR} = \frac{E_{mass}}{\rho_{water} \times S_{sea}} \quad (4.16)$$

Where S_{sea} is the world sea surface area and E_{SLR} is the error associated with the rise in sea levels induced by $dDEM$.

4.1.8.6 Scale of the analysis

As the quality of the DEMs varies depending on the methods and data, Folgefonna is studied on two levels:

- **The three ice caps:** 100% of Folgefonna, from 1959 to 2017
- **The local region:** < 30% of Folgefonna, from 1937 to 2017

4.1.9 Evolution of the mass balance by gravimetry

The change in water mass of Folgefonna is calculated through gravimetric monitoring with data from the Gravity Recovery and Climate Experiment (GRACE) satellite mission.

4.1.9.1 GRACE data

Raw GRACE data can be found on the data analysis tool provided by the GRACE Nasa website (Figure 4.13). Available data on this website is pre-processed, which means that the evolution of water mass is already computed. Two centers are used and compared:

- NASA's Jet Propulsion Laboratory (JPL)
- the Center for Space Research (CSR) (University of Texas).

The GRACE mission was launched in April 2002; thus, data from April 2002 until December 2021 are used.

This tool provides water equivalent thickness data. Graphs are automatically and freely generated by ROI selection (with georeferences). Calculating the glacier area makes it possible to convert water equivalent thickness data into water mass.

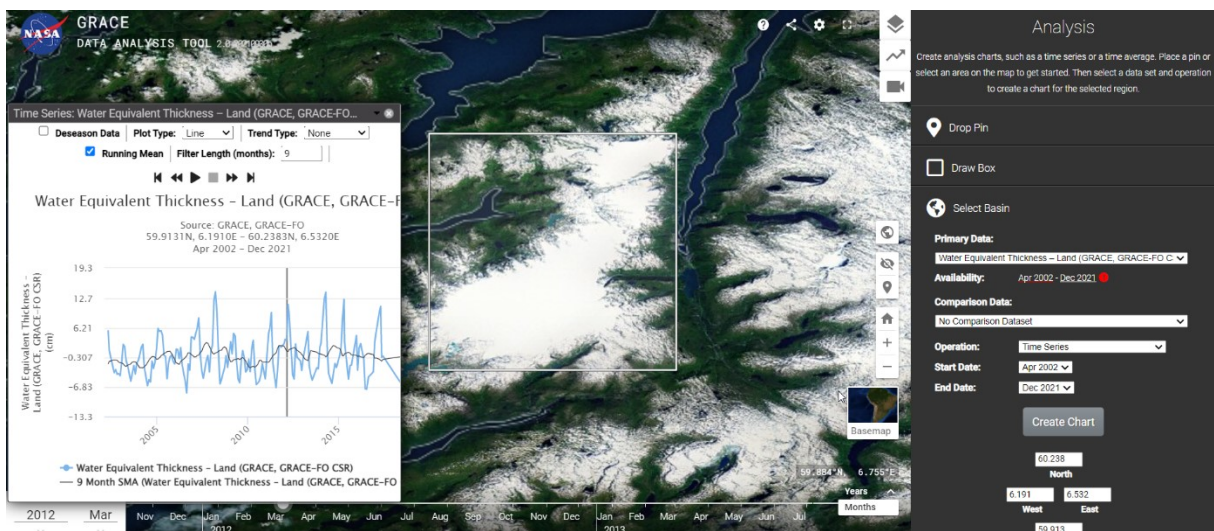


Figure 4.13: Water equivalent thickness fluctuation obtained on GRACE's website –GRACE NASA data analysis tool

Once the data was downloaded, the mean calculations were performed to analyze fluctuations in water mass. Both averages are calculated for 12 and 24 months.

4.1.9.2 Biases and utility

Gravimetric data is helpful; however, variations can only be compared to the mass evolution calculated from DEMs. Gravimetric data correlates to an area's mass (solid water + liquid water). Thus, the mass of glaciers could decrease while liquid water within lakes, soils or aquifers increases. In such a case, no significant gravimetric data fluctuations are seen.

GRACE data is available monthly from April 2002; this data is derived and compared to the mass calculations from DEMs.

4.2 DEM processing software development

A DEM processing software was developed to apply glaciology's most promising DEM methods. The secondary objective was to simplify and gain efficiency in processing glacier DEMs. The software allows the co-registration, subtraction, interpolation, calculation volume change, determination of local errors and complete PDF report generation in a single run. Moreover, the user can simultaneously launch a sole or a series of processes.

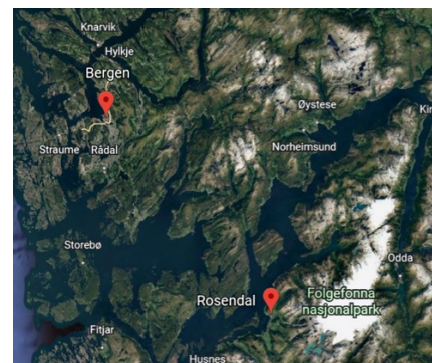


Figure 4.14: Rosendal and Bergen station location

4.2.1.1 Backend frameworks

The frameworks used in the main functions are only presented – for the co-registration, interpolation and error calculation, the Xdem framework was partly used (Mannerfelt, et al., 2021). This framework uses methods published in the scientific literature (i.e. Nuth and Kääb algorithm for the co-registration). Furthermore, a script provided by the DEMcoreg framework was modified and used for volume change calculations.

4.2.1.2 Graphical User Interface framework

The PySimpleGUI framework was used to develop the User Interface (UI). It is a Graphical User Interface¹⁴ (GUI) framework written in python, which supports python's 3rd version. The main full-featured version, "Tkinter-based graphics," is used.

As the core element is the backend, a simple frontend framework was the practical choice. PySimpleGUI is a straightforward GUI framework without any object-oriented requirements and a small amount of code (Sun and Grimmond, 2019). PySimpleGUI is well documented and widely used across the world. Moreover, this framework allows creating Linux, Mac, and Windows applications.

¹⁴ GUI is part of a computer program created for human interaction.

4.3 Correlation calculations

4.3.1 Correlation of ELA and glacier area

4.3.1.1 Data acquisition

Meteorological data was directly downloaded from the Norwegian Meteorological Institute eKlima¹⁵. The precipitation records are available from the Rosendal station, located west of Folgefonna, as of 1930. However, the availability of temperature statistics is reduced. Nevertheless, the temperature data from Bergen–Florida is accessible as of 1870 and is therefore used.

All meteorological data is collected monthly, and then the moving averages are calculated.

4.3.1.2 Correlation between surface area and ELA

This section determines which features present the highest correlation coefficient between the surface areas and climatic data and between the ELA and climatic data.

The temperature and precipitations are the only features used to observe the correlation with climatic data.

Several combinations were assessed:

- Yearly precipitations
- Yearly temperatures
- Summer temperatures
- Winter precipitations
- Summer temperatures + Winter precipitations

Theoretically, these features present various seasonal influences. For wetting glaciers, it has been shown that temperatures in spring, summer, and fall greatly influence ablation (Oerlemans et al., 2000). At the same time, precipitations influence ablation through rainfall and snowfall, which then, in turn, influence the accumulation.

The applied correlation calculation is the following:

$$\rho_{x,y} = \frac{\text{cov}(x,y)}{\sigma_x \sigma_y} \quad (4.17)$$

Where $\text{cov}(x,y)$ is the co-variance between x and y , σ_x and σ_y respectively are the standard deviation of x and y and $\rho_{x,y}$ is the correlation index of x and y .

4.3.2 GRACE data correlations

Two types of correlations were performed for GRACE data; the first one is the correlation between the GRACE data and the climatic data and between the GRACE data and the glacier area data. The primary goal of these calculations is to confirm or refute GRACE data in this analysis.

The above equation 4.17 was to perform these two correlations. As the GRACE data is available monthly, the correlation was performed by a monthly interval with the climatic data. Due to the lack of GRACE data, precipitations are summed on the concerned periods and

¹⁵ More precisely, on the Norwegian Meteorological Institute website: seklima.met.no.

averages are calculated for the temperature. For example, if GRACE data is missing for January and February, the precipitations for March are the following:

$$Precipitation_used_{march} = Precipitation_{march} + Precipitation_{february} + Precipitation_{january} \quad (4.18)$$

Where $Precipitation_used_{march}$ is the precipitation used for the correlation calculation for March, and $Precipitation_x$ is the raw precipitation data of the month x.

For the temperature:

$$Temperature_used_{march} = \frac{Temperature_{march} + Temperature_{february} + Temperature_{january}}{3} \quad (4.19)$$

Where the $Temperature_used_{march}$ is the temperature used in the correlation calculation for the month of March. $Temperature_x$ is the raw temperature data of the month x.

4.4 Open–Global Glacier Model – historical and future evolution

This section describes the produced historical and forthcoming glacier simulations of Folgefonna through the Open Global Glacier Model (OGGM) physical model.

4.4.1 Model description

OGGM is an open–source model coded in python (Rounce et al., 2019). It can simulate glaciers’ dynamics for past, present, and future climate, by computing the volume and area change of a specific glacier (Maussion et al., 2019). The latest version of this model was used (OGGM 1.5.3).

4.4.2 Choice of the methods

OGGM was chosen for the following reasons:

- The possibility of computing bedrock topography from drainage basin information
- The open–source availability

Nonetheless, numerous other models exist. ALPGM, another open–source python script based on deep learning technics (Bolibar, 2020), was tested to compute the future evolution of Folgefonna. There are two drawbacks to applying this script to Folgefonna. Firstly, a bedrock topographic layer is required; secondly, ALPGM is currently set for glaciers in the Alps. Folgefonna’s conditions are unrelated to those of alpine glaciers, so the model would have to be trained with historical mass balance data of southwestern Norwegian glaciers and their associated climatic data. As the training of ALPGM would have been extensively time-consuming and requires a considerable amount of data, using this model was rejected.

4.4.3 Workflow

This section summarizes the method of processing inspired by Maussion et al. in 2019:

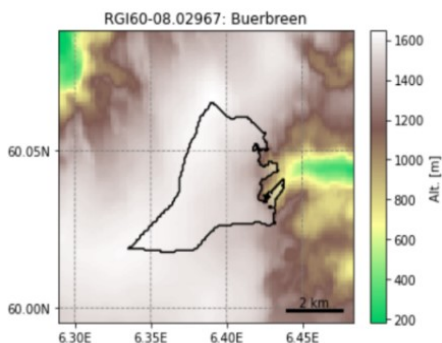


Figure 4.15: Buerbreen glacier, with RGI outlines and aerial LiDAR DEM.

- **Flowlines:** The glacier centerlines are computed using a geometrical routing algorithm (adapted from Kienholz et al., 2014).
- **Climatic data and mass balance:** Gridded climatic data (monthly temperature and precipitation) is interpolated from the glacier location. The temperature was corrected from the altitude using a linear gradient.

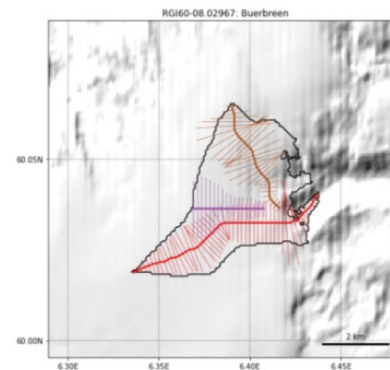


Figure 4.16: Catchment area and flowlines of Buerbreen

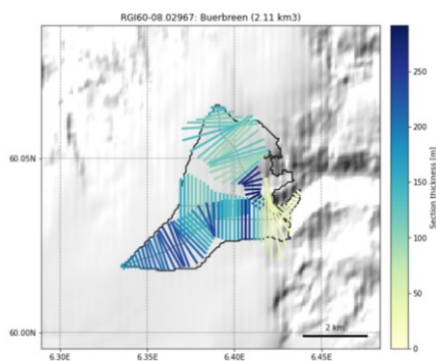


Figure 4.17: Ice thickness of Buerbreen

- **Glacier evolution:** A dynamic flow-line model simulates the glacier's advance and retreat in response to the surface mass-balance forces.

- **Ice thickness inversion:** By using the mass-balance data previously computed and relying on mass-conversion considerations, an estimate of the ice flux along each glacier cross-section is computed.

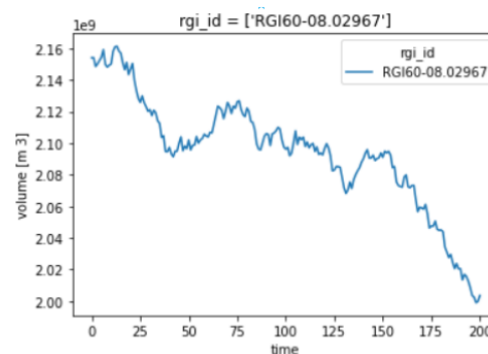


Figure 4.18: Volume evolution of Buerbreen in the next 200 years.

4.4.4 Model description

This section contains the main calculations for the OGGM script.

4.4.4.1 Script processing

To calculate the evolution of ice thickness with climatic data, the following equations are used in OGGM (Rounce et al., 2020):

$$B = \frac{\sum_{bin=0}^n b_{clim,bin} \cdot S_{bin}}{S} \quad (4.20)$$

Where B is the monthly mass balance, S is the glacier area, and bins refer to each elevation bin (presented in Figure 4.14 as the color lines) and $b_{clim,bin}$ is associated with the elevation change equivalent in water. $b_{clim,bin}$ is defined as follows:

$$b_{clim,bin} = a_{m,bin} + c_{m,bin} + R_{potential} \quad (4.21)$$

Where $a_{m,bin}$ is the ablation, $c_{m,bin}$ is the accumulation, and $R_{potential}$ is the potential of refreezing.

The ablation as a function of bins ($a_{m,bin}$) is calculated as follows:

$$a_{m,bin} = \begin{cases} f^{snow,ice,firn} \cdot T_{m,bin} \cdot n & \text{if } T_{m,bin} \geq 0 \\ 0 & \text{if } T_{m,bin} \leq 0 \end{cases} \quad (4.22)$$

Where f is the degree day factor of snow, ice or firn (m.w.e./d/°C), $T_{m,bin}$ is the monthly mean near-surface air temperature (°C), and n is the number of days in each month.

The accumulation as a function of bins ($c_{m,bin}$) is calculated as follows:

$$c_{m,bin} = \delta_{m,bin} \cdot P_{m,bin} \quad (4.23)$$

Where $\delta_{m,bin}$ is the monthly fraction of solid precipitations and $P_{m,bin}$ is the monthly precipitations (m.w.e.). $\delta_{m,bin}$ is based on $T_{m,bin}$ and the temperature threshold used to differentiate between liquid and solid precipitation as follows:

$$\delta_{m,bin} = \begin{cases} 1 & \text{if } T_{m,bin} \leq T_{snow} - 1 \\ 0 & \text{if } T_{m,bin} \geq T_{snow} + 1 \\ 0.5 + \frac{T_{m,bin} - T_{snow}}{2} & \text{if } T_{snow} - 1 < T_{m,bin} < T_{snow} + 1 \end{cases} \quad (4.24)$$

Monthly precipitations ($P_{m,bin}$) are calculated as a function of the precipitations factor, k_p , according to:

$$P_{m,bin} = P_{m,GCM} \cdot k_p \cdot (1 + d_{prec} \cdot (z_{bin} - z_{ref})) \quad (4.25)$$

Where $P_{m,GCM}$ is the monthly precipitations from the climate data based on the nearest neighbors, and d_{prec} is the precipitations gradient (%/m).

And finally, the potential of refreezing ($R_{potential}$), is calculated as a function of the weighted annual mean air temperature, T_a (°C):

$$R_{potential} = -0.0069 \cdot T_a + 0.000096 \quad (4.26)$$

4.4.5 Climatic data

The monthly time series of temperatures and precipitations from the Climatic Research Unit (CRU) TS v4.04 gridded dataset covering 1902–2019 are used to calibrate the temperature index model in OGGM (Marzeion et al., 2012).

The gridded monthly temperatures and precipitations data of CMCC–CMS GCM from the CMIP6 projected under RCP 2.6, RCP 4.5, RCP 6.5 and RCP 8.5 climate scenarios are used in OGGM to simulate the glacier area and volume changes from 2020 to 2100. The low–resolution CMCC–CMS GCM data are downscaled to higher resolution in specific glacier methods before estimating the glacier dynamics.

4.4.6 Spatial data

The glacier outlines of the Randolph Glacier Inventory (RGI v6.0) (RGI Consortium, 2017), released in 2017 and distributed by the Global Land Ice Measurements from Space (GLIMS), are used for initial topographical processing in OGGM.

Moreover, the Shuttle Radar Topography Mission (SRTM) provides a 90m digital elevation database – version 4.1 from the Consultative Group on International Agricultural Research. This DEM was used in OGGM to project the glacier outlines to a local gridded map.

The DEM from the Advanced Spaceborne Thermal Emission and Reflection Radiometer (ASTER), global DEM v2 of 30m resolution, available from the United States Geological Survey (USGS), is used to compute the grid elevation data in GDM.

Chapter 5

Results

This chapter presents the results obtained from formerly presented processing methods.

5.1 Historical evolution of Folgefonna by remote sensing

5.1.1 Evolution of the glacier area

Due to varying dynamics within the three ice caps, different ROIs were calculated for the following regions:

- Three ice caps of Folgefonna
- Søndre Folgefonna
- Midtre Folgefonna
- Nordre Folgefonna

For each ROI, two types of calculations are carried out. The first is the computation of raw data (i.e. section 5.1.1.1.1). The second corresponds to a manual data filtration (i.e. section 5.1.1.1.2) to reduce the noise caused by the presence of snow and/or clouds. The standard deviations for a given period are compared to the variations; when the standard deviation is at least two times higher than the variations, the associated glacier area is removed.

For the three ice caps of Folgefonna, the evolution is calculated from 1959 to 2021, while for Midtre, Søndre, and Nordre Folgefonna, the period is only from 1985 to 2021.

5.1.1.1 Three ice caps of Folgefonna

5.1.1.1.1 Folgefonna –unfiltered

Figure 5.1 displays the results for the three ice caps of Folgefonna. In 2021, the glacier area was $180.7 \pm 11\text{km}^2$. It fluctuated by $+8.7 \pm 28\text{km}^2$ between 1959 and 1994. Following this period, from 1994 to 2021, the glacier area decreased by $53.74 \pm 25\text{km}^2$ ($-1.99\text{km}^2/\text{yr}$), representing 22.92% of the glacier area in 1994.

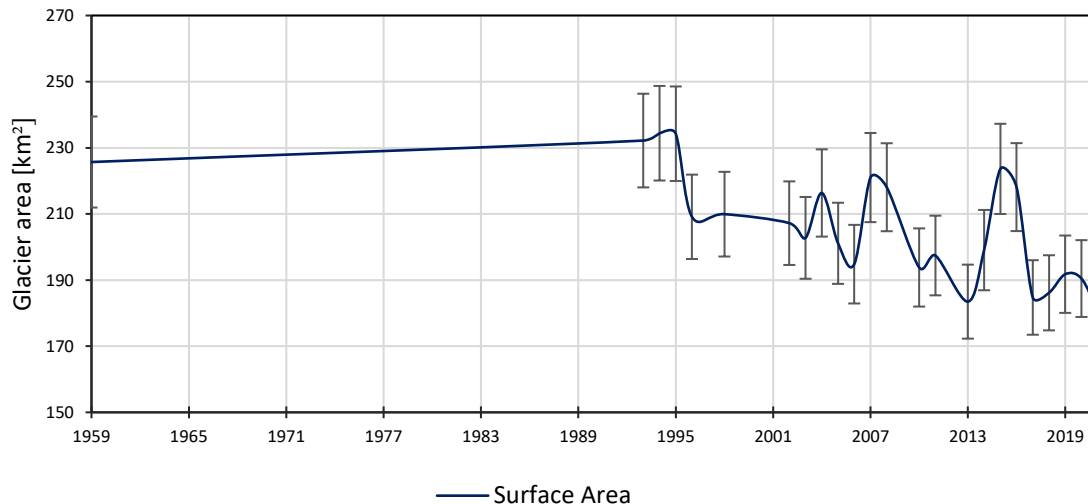


Figure 5.1: Unfiltered glacier area of the three ice caps of Folgefonna

5.1.1.1.2 Folgefonna – filtered

A filter is applied to remove the years with exceptionally high snow levels.

Figure 5.1 offers three variabilities. From 2004 to 2007, the standard deviation is 10.71km², and the glaciers gained 4.66km². From 2006 to 2010, the standard deviation is 12.66km², and the glaciers lost 1km². From 2013 to 2017, the standard deviation is 16.59km², and the glaciers expanded by 2.67km².

The following years were deleted: 2004 – 2007 – 2008 – 2015 – 2016.

Figure 5.2 illustrates the filtered data for the three ice caps of Folgefonna. The glaciers have been shrinking linearly since 1995.

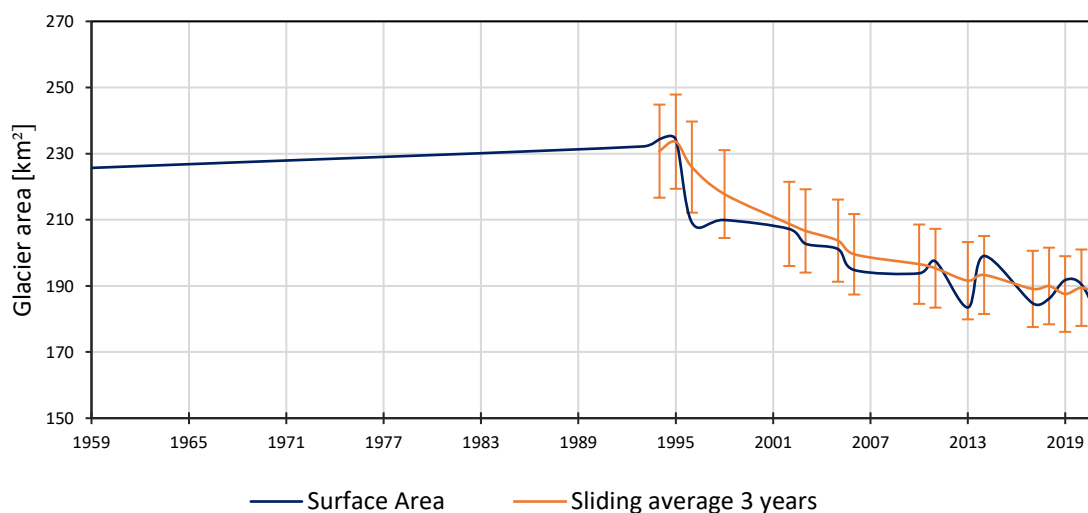


Figure 5.2: Filtered glacier area of the three ice caps of Folgefonna glacier

5.1.1.2 Søndre Folgefonna

5.1.1.2.1 Søndre Folgefonna – unfiltered

Appendix A.7 shows the evolution of Søndre Folgefonna without filtering. In 2021, the glacier area is of $154.9 \pm 9.5\text{km}^2$. From 1994 to 2021, the glacier lost $33.6 \pm 20.6\text{km}^2$, representing 18.17% of the glacier area in 1994. However, from 1985 to 1994, it seems to have grown by $5 \pm 22\text{km}^2$ ¹⁶.

5.1.1.2.2 Søndre Folgefonna – filtered

On Søndre Folgefonna, the fluctuations caused by snow coverage are lower compared to Midtre Folgefonna and Nordre Folgefonna. Between 2013 and 2015, the standard deviation is approximately 12.1km^2 , representing 6.55% of the glacier area in 1994.

The following five years were removed: 1989 – 2007 – 2008 – 2015 – 2016.

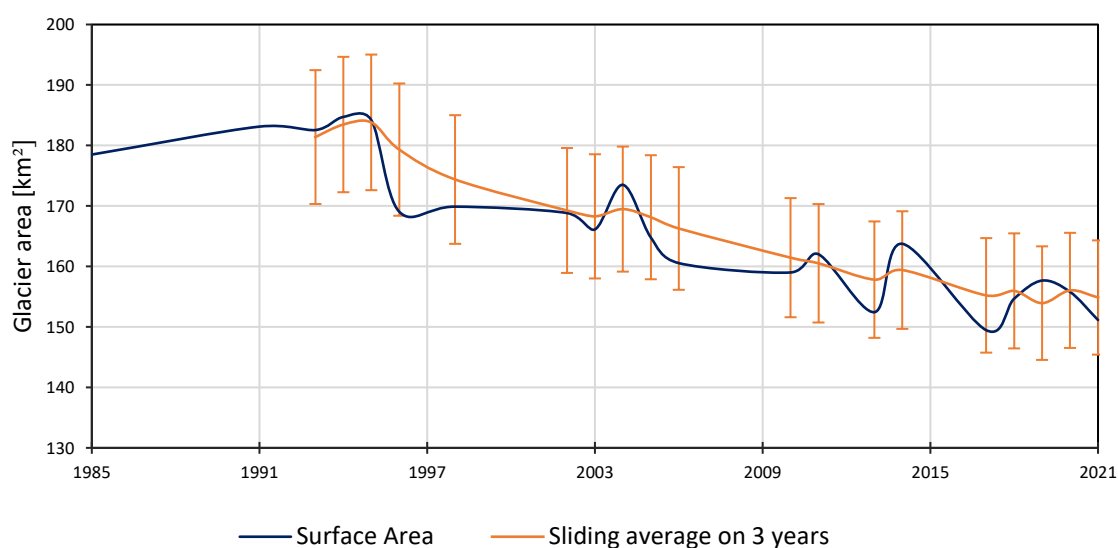


Figure 5.3: Evolution of the glacier area of Søndre Folgefonna – filtered

5.1.1.3 Midtre Folgefonna

5.1.1.3.1 Midtre Folgefonna – unfiltered

Midtre Folgefonna is the smallest ice cap with more continuous snow coverage than Søndre Folgefonna. In 2021, the glacier area was evaluated at $6.7 \pm 0.4\text{km}^2$. From 1994 to 2021, this ice cap lost $12.7 \pm 1.6\text{km}^2$ of its surface area, representing 68.91% of the glacier area in 1994 (Appendix A.8).

5.1.1.3.2 Midtre Folgefonna – filtered

The snow coverage on Midtre Folgefonna can be persistent until the end of the summer causing high fluctuations in the glacier area, which significantly influences the glacier area calculations. The standard deviation between 2006 and 2010 is 5.04km^2 , corresponding to 27.3% of the glacier area in 1994. Between 2014 and 2015, the standard deviation is 4.73km^2 , corresponding to 25.66% of the glacier area in 1994.

¹⁶ The uncertainty is most likely over-evaluated.

The following six years were removed: 1989 – 2004 – 2007 – 2008 – 2015 – 2016.

Figure 5.4 establishes the resulting data where years with significantly high snow coverage were removed.

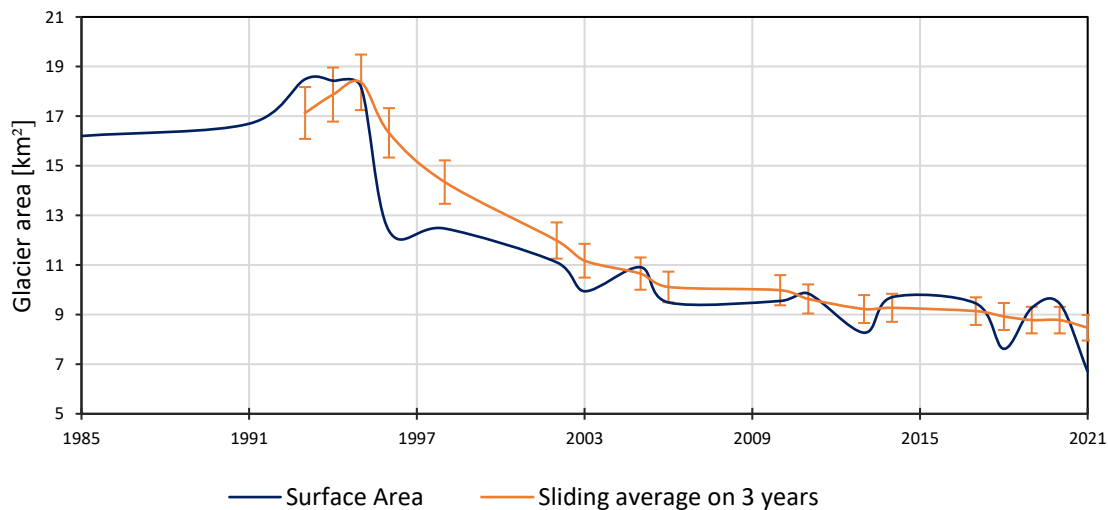


Figure 5.4: Evolution of the glacier area of Midtre Folgefonna – manually filtered

5.1.1.4 Nordre Folgefonna

5.1.1.4.1 Nordre Folgefonna – unfiltered

In 2021, Nordre Folgefonna had an area of $22.81 \pm 1.57\text{km}^2$. From 1994 to 2021, the glacier lost $9.14 \pm 3.32\text{km}^2$, representing 28.6% of the glacier area in 1995.

5.1.1.4.2 Nordre Folgefonna – filtered

For Nordre Folgefonna, there was one particular period with high snow coverage. From 2013 to 2018, the standard deviation was 2.8km^2 , and the glacier area increased by 1.09km^2 .

The removed years are the following: 2007 – 2014 – 2015 – 2016 – 2017.

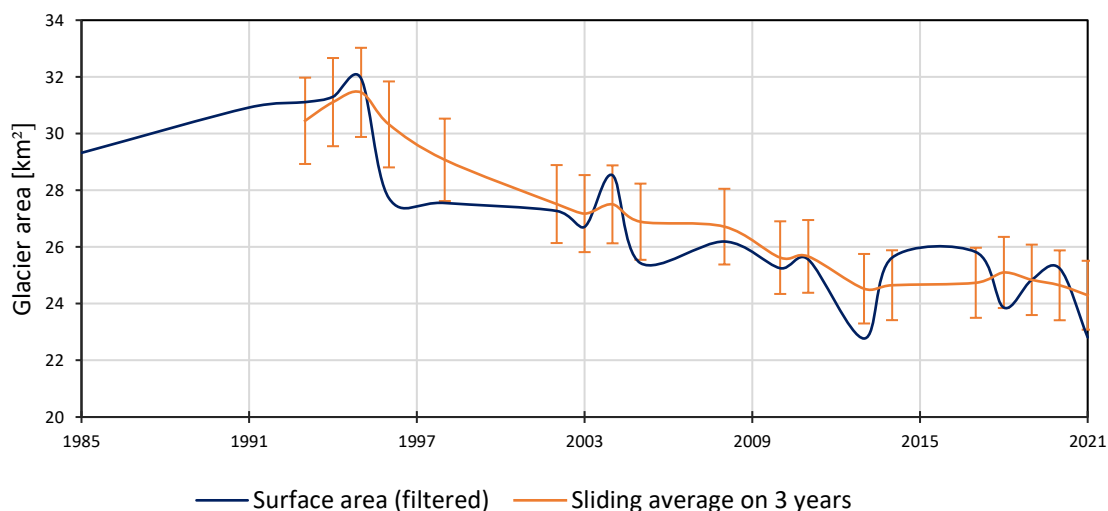


Figure 5.5: Evolution of the glacier area for Nordre Folgefonna – manually filtered

5.1.2 Equilibrium Lines Altitude

Similarly to the glacier area calculations, the ELA is calculated on four scales:

- Three ice caps of Folgefonna
- Søndre Folgefonna
- Midtre Folgefonna
- Nordre Folgefonna

The evolution is calculated from 1988 to 2021.

5.1.2.1 Three ice caps of Folgefonna

In 2021, the ELA of the three ice caps of Folgefonna is estimated at 1433.15m.

Between 1994 and 2021, the moving average (blue curve in Figure 5.6) increased by 88.5m. Three phases are observed; from 1994 to 2005, the moving average of the ELA increased by 127.9m. From 2005 until 2013, the moving average decreased by 58.3m. Then, from 2013 to 2019, the moving average stabilized around 1415m. Finally, from 2019 to 2021, the ELA increased by 21.6m.

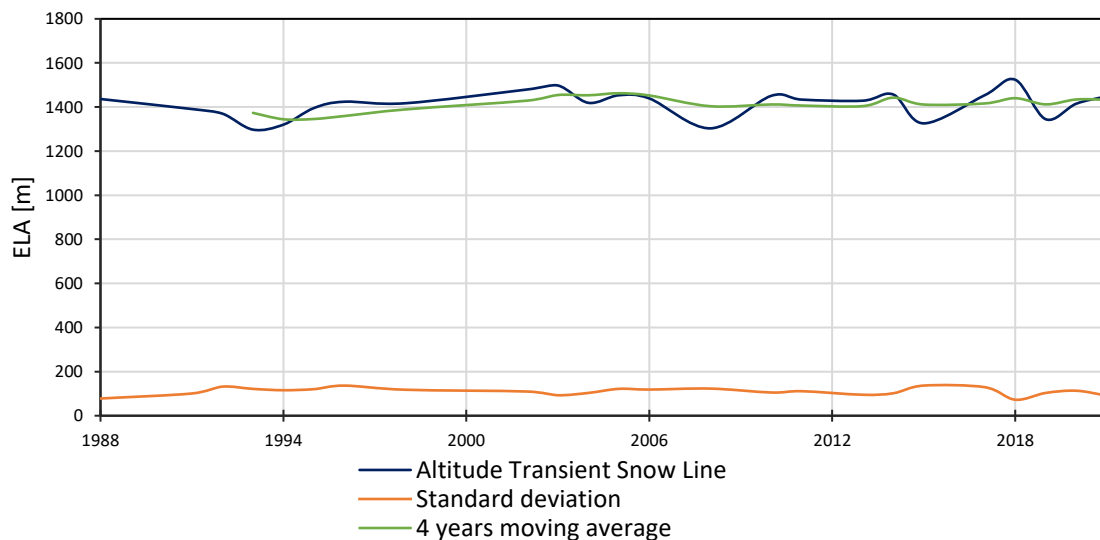


Figure 5.6: ELA between 1987 and 2022 for the three ice caps of Folgefonna.

5.1.2.2 Søndre Folgefonna

The Evolution of the ELA for Søndre Folgefonna is strongly correlated to the data of the three ice caps of Folgefonna (Figure 5.7), and three phases appear. In 2021, the ELA was estimated at 1425.7m. From 1995 to 2021, the ELA increased by 88.57m.

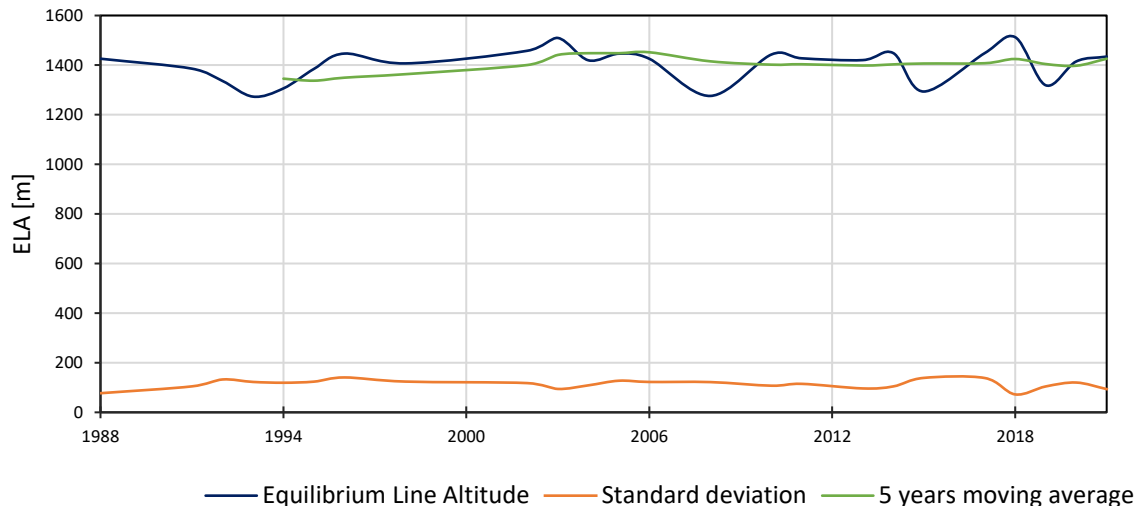


Figure 5.7: Evolution of ELA for Søndre Folgefonna from 1987 to 2022

5.1.2.3 Midtre Folgefonna

For Midtre Folgefonna, in 2021 the ELA is 1411.4m. From 1995 to 2021, the ELA increased by 34.3m. There are five distinct phases. For the periods from 1995–2005, 2010–2017, and 2020–2021, the ELA increases, while from 2005–2010 and 2017–2020, the ELA decreases.

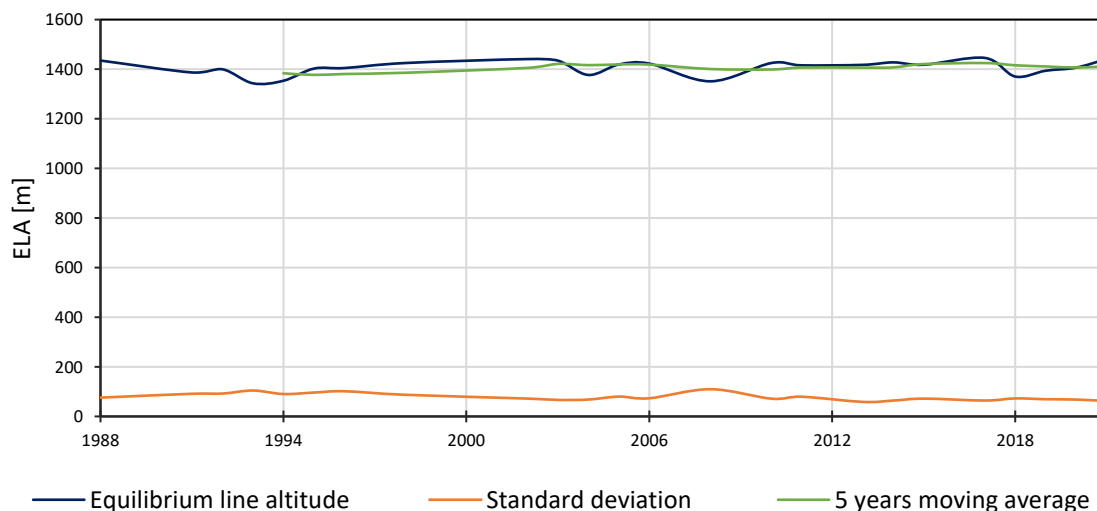


Figure 5.8: Evolution of ELA for Midtre Folgefonna

5.1.2.4 Nordre Folgefonna

For Nordre Folgefonna, in 2021 the ELA is 1479.1m. From 1994 to 2005, the ELA increased by 85.1m. Two different phases are observed. From 1994 to 2005, the glacier area increases by 97.5m. Then, from 2006 to 2021, the five-year moving average remains constant.

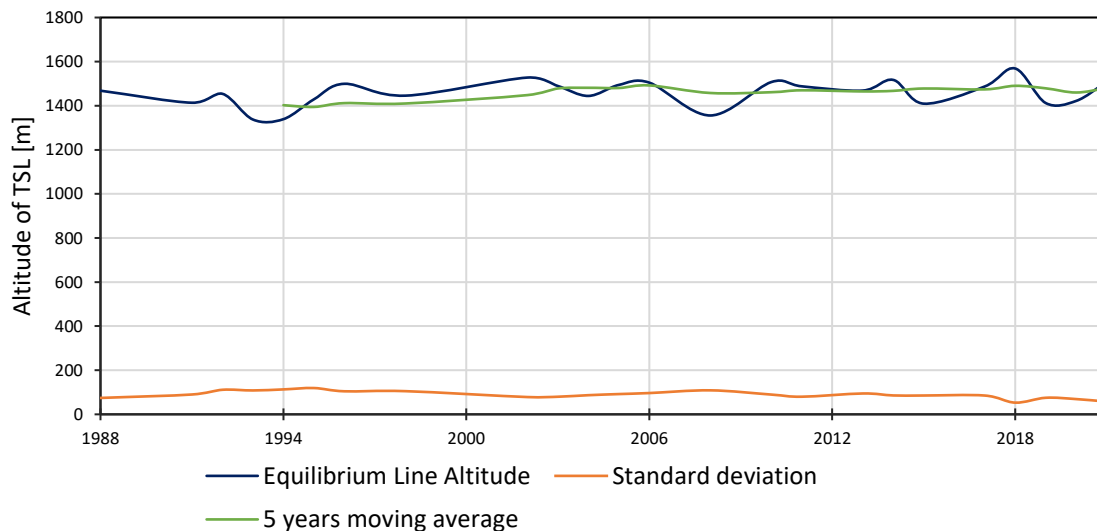


Figure 5.9: Evolution of the ELA for Nordre Folgefonna from 1987 to 2022

5.1.3 Glacier snow area

This section presents the snow area evolution on the glacier at the end of the ablation season. These results were obtained during the ELA calculations. The same four scales for the glacier area and ELA calculations are used. The evolution is calculated from 1988 to 2021.

5.1.3.1 Three ice caps of Folgefonna

In 2021, the snow area on three ice caps of Folgefonna was 120.3 km² (Figure 5.10), and the five-year moving average was as follows:

- From 1995 to 2021, the snow area decreased by 45.5 ± 17.45 km²
- From 1995 to 2004, the snow area decreased by 70.92 ± 15.90 km²
- From 2004 to 2010, the snow area increased by 54.11 ± 14.85 km²
- From 2010 to 2021, the snow area decreased by 28.79 ± 16.42 km²

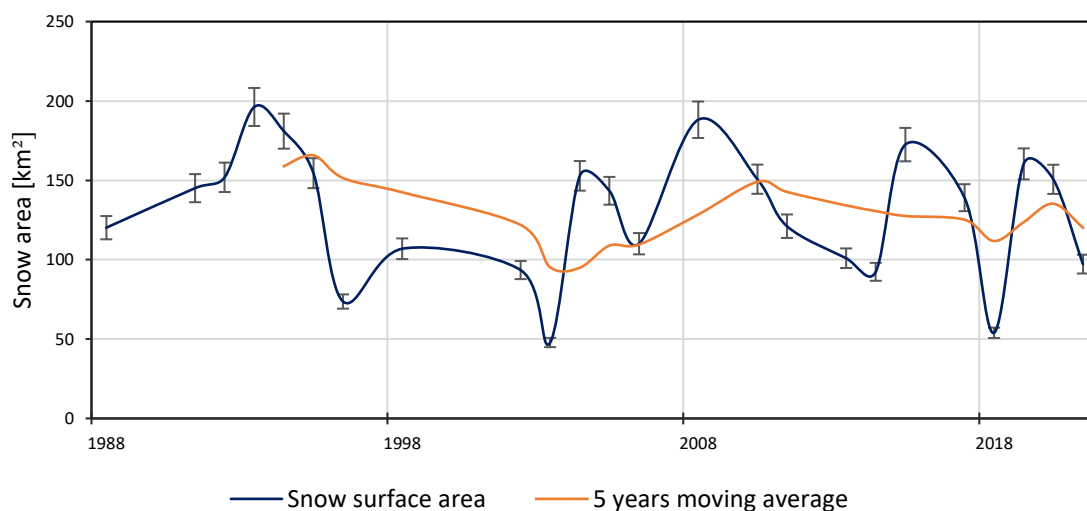


Figure 5.10: Evolution of the snow area for the three ice caps from 1987 to 2022, at the end of the ablation period (August – September)

5.1.3.2 Søndre Folgefonna

The snow area of Søndre Folgefonna in 2021 (Appendix A.10) was $100.7 \pm 6.1\text{km}^2$. The tendency is similar for the three ice caps of Folgefonna, as Søndre is the largest. From 1995 to 2021, the snow area decreased by $33.6 \pm 14.3\text{km}^2$.

5.1.3.3 Midtre Folgefonna

The snow area of Midtre Folgefonna in 2021 (Appendix A.11) was $0.69 \pm 0.04\text{km}^2$, meaning that the glacier's surface was mainly composed of ice. From 1993 to 2021, the snow area decreased by $11.85 \pm 0.79\text{km}^2$, 95.26% of the area in 1993.

5.1.3.4 Nordre Folgefonna

The snow coverage of Nordre Folgefonna in 2021 (Appendix A.12) was $15.2 \pm 0.92\text{km}^2$. From 1994 to 2021, it decreased by $6.6 \pm 2.24\text{km}^2$, 30.1% of the area in 1994.

5.1.4 DEMs evolution

This section presents the results obtained by DEM calculation.

5.1.4.1 Photogrammetry

Four DEMs were built by photogrammetry (1937, 1953, 1962 and 1981); the results obtained during the processing of the DEMs are presented in Table 5.5 and Figure 5.12.

- For 1937: The photographs were only taken on the east side of Folgefonna. The DEM obtained, therefore, only covers 19.52% of the DEM carried out in 1959. The photogrammetric processing was sufficiently effective due to low flight altitude and snow coverage.
- In 1953: the Photographs were taken south of Søndre Folgefonna. The DEM obtained covers 66.98% (ref:1959). However, due to high snow coverage, the photographs contain voids in the center.
- In 1962: The photographs cover the periphery of Søndre Folgefonna, Midtre Folgefonna and Nordre Folgefonna. The DEM obtained covers 22.32% (ref:1959).
- In 1981: The photographs were taken on the entire three ice caps of Folgefonna. The DEM obtained covers 30.87% (ref:1959). The final DEM has a low coverage rate due to high snow coverage and the low image contrast.

Year	Images	GCPs	Dense Quality	Dense Filtering	RMSE _x (m)	RMSE _y (m)	RMSE _z (m)	Dense count points	GSD (m/pix)
1937	16	16	Ultra high	Moderate	–	–	–	–	–
1953	33	10	Ultra high	Agressive	0.0015	0.0016	0.00039	1.405 M	0.44
1962	94	11	Ultra high	Moderate	0.035	0.023	0.0097	2.407 M	0.37
1981	37	9	Ultra high	Moderate	0.0024	0.0026	0.00063	871 M	1.03

Table 5.1: Results obtained by photogrammetry

5.1.4.2 Co-registration results

Concerning the co-registration, the reference layer for the stable ground was the 2017 DEM downloaded on the hoyededata.no website. This DEM offers an extensive and precise area around the glacier, with a 0.5m resolution (aerial LiDAR).

Eagloo is used to compute the co-registration. Eight combinations of Nuth and Kääb, ICP, Deramp, and Vertical Offset are utilized (Table 5.8 for Eagloo results).

The method offering the best results is the combination of ICP and Nuth and Kääb. It is used for 1937, 1962, 1981, 2007, and 2013. The Nuth and Kääb algorithm is solely used for 1959.

Year calculated	Reference DEM	Resolution [m]	Method	Vertical offset (dz) [m]	East offset (dx) [m]	North offset (dy) [m]	Rotation around the vertical axis	NMAD [m]
1937	2017	8	ICP + Nuth and Kääb	-47.70	16.24	5.48	0 °	8.44
1959	2017	8	Nuth and Kääb	-2.87	- 10.94	9.28	0°	6.74
1962	2017	10	ICP + Nuth and Kääb	-15.27	- 15.25	13.29	-	12.39
1981	2017	10	ICP + Nuth and Kääb	-4.56	-4.45	8.11	0°	6.38
2007 Nordre Folgefonna	2017	30	ICP + Nuth and Kääb	-5.88	- 62.73	60.52	-0.24°	8.42
2007 Midtre Folgefonna	2017	30	ICP + Nuth and Kääb	-4.57	- 20.22	20.72	-0.04°	5.15
2007 Søndre Folgefonna	2017	30	ICP + Nuth and Kääb	-0.98	-9.53	10.75	0°	9.7
2013	2017	7	ICP + Nuth and Kääb	0.21	-0.32	1.82	0°	1.18

Table 5.2: Co-registration results for each DEM

5.1.4.3 Uncovered glacier area

Indeed, the processed DEMs contain voids on glacierized parts. This is a major issue for the observation of Folgefonna's evolution. Table 5.3 exposes the surface area of the entire glacier covered by each DEM.

Year calculated	Glacier area covered without interpolation
1937	19.52 % (ref :1959)
1953	66.98 % (ref :1959)
1959 (3 ice caps)	100 %
1962	22.32 % (ref :1959)
1981	30.87 % (ref :1959)
2007 (3 ice caps)	100 %
2013 (3 ice caps)	100 %
2017 (3 ice caps)	96.9 % (ref :2013)

Table 5.3: Glacier area covered without interpolation

5.1.4.4 Folgefonna (3 ice caps, coverage: 100%)

In this part, the evolution of Folgefonna for the three ice caps is calculated. Four years are used to perform this calculation: 1959 – 2007 – 2013 – 2017.

The results in Table 5.5 from 1959 to 2017 present the following:

- The volume of ice decreased by $3,03 \pm 0,059 \text{ km}^3$ (Figure 5.12)
- The mass decreased by $2,6 \pm 0,63 \text{ Gt}$ (Figure 5.12)
- The sea-level increased by $7,2 \pm 1,8 \mu\text{m}$
- The offset in meter water equivalent decreased by $12,19 \pm 2,44 \text{ m}$

The 2013 DEM downloaded on the website hoyededata.no is used as a reference to calculate the mass and volume change. The DEM covers the three ice caps with at least a five-meter resolution. It was shaped by aerial LiDAR. Table 5.5 presents the associated errors used for the calculation of the mass and volume change.

Year calculated	Reference DEM	Standardized Integrated error [m]	Glacier area + error Without slope correction [km ²]	Ice density + error [g/cm ³]
1959	2013	2.42	216.73 ± 13.2	0.85 ± 0.06
2007	2013	0.089	190.06 ± 11.59	0.85 ± 0.06
2017	2013	0.0159	182.01 ± 11.01	0.85 ± 0.06

Table 5.4: Errors in volume and mass difference between all DEMs

Table 5.5 presents the results for the volume difference, mass difference, meter water equivalent and contribution to sea level rise.

Year calculated	Reference DEM	Surface Interpolated	Volume change (Latest–Earliest) [km ³]	Mass change [Gt]	Meter water equivalent [m.w.e.]	Contribution to sea level rise [mm]
1959	2013	0 %	-3.10 ± 0.53	-2.636 ± 0.600	-12.16 ± 2.35	0.0073 ± 0.0017
2007	2013	0 %	-0.747 ± 0.017	-0.635 ± 0.072	-3.342 ± 0.321	0.0017 ± 0.0002
2017	2013	2.26 %	0.0069 ± 0.0290	0.0058 ± 0.0290	0.0320 ± 0.1354	-0.000016 ± 0.000081

Table 5.5: Results for the volume difference, mass difference, meter water equivalent and contribution to sea-level rise for all DEMs

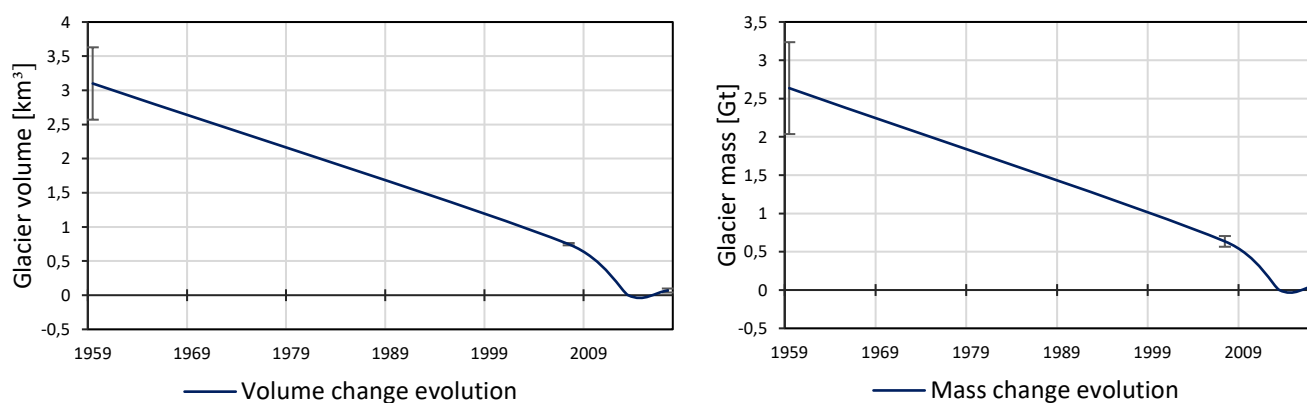


Figure 5.12: Evolution of the mass and volume change of the three ice caps of Folgefonna

5.1.4.5 Evolution of Folgefonna since 1937

Due to numerous voids on the DEMs calculated through photogrammetry, a local observation where the glacier is better shaped was performed. This choice was induced by the quality of the earliest DEM (1937), which was chosen as local ROI. The surface area is 42.30km² in 1959 (with a slope correction), which is equivalent to 19.52% of the glacier area in 1959.

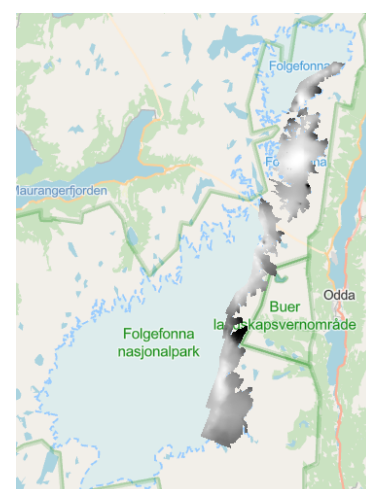


Figure 5.11: DEM (black and white layer) used to monitor the evolution of Folgefonna since 1937

Year calculated	Reference DEM	Standardized integrated error [m]	Glacier area + error (Without slope correction)[km ²]	Ice density + error [g/cm ³]
1937	2013	1.55	40.53 ± 2.47	0.85 ± 0.06
1959	2013	3.99	38.92 ± 2.37	0.85 ± 0.06
1962	2013	5.33	38.92 ± 2.37	0.85 ± 0.06
1981	2013	2.138	39.83 ± 2.43	0.85 ± 0.06
2007	2013	2.21	29.54 ± 1.80	0.85 ± 0.06
2017	2013	0.56	23.44 ± 1.43	0.85 ± 0.06 g

Table 5.6: Errors in volume and mass change for all DEMs

For the evolution at a local scale, it is essential to note that two DEMs were interpolated using a local hypsometric method. The DEM calculated for 1962, 36.98%, was interpolated (reference is the ROI presented in Figure 5.11). For the 1981 DEM, 41.8% was interpolated.

Two phases are observed:

From 1937 to 1962:

- The volume difference was $+0.273 \pm 0.271 \text{ km}^3$ (Figure 5.13)
- The mass difference was $+0.3 \pm 0.3 \text{ Gt}$ (Figure 5.13)
- The meter water equivalent was $+10.05 \pm 7.19 \text{ m.w.e.}$
- The contribution to the rise of sea level was $-0.842 \pm 0.881 \mu\text{m}$

From 1962 to 2017:

- The volume difference was $-1.087 \pm 5.84 \text{ km}^3$ (Figure 5.13)
- The mass difference was $-0.9137 \pm 0.2426 \text{ Gt}$ (Figure 5.13)
- The meter water equivalent was $-25.33 \pm 5.84 \text{ m}$
- The contribution to the rise of sea level was $+2.574 \pm 0.64 \mu\text{m}$

Year calculated	Reference DEM	Surface Interpolated	Volume change (Latest–Earliest) [km ³]	Mass change [Gt]	Meter water equivalent [m.w.e.]	Contribution to sea level rise [mm]
1937	2013	0%	-0.7338 ± 0.0630	-0.6237 ± 0.0885	-15.3883 ± 1.8558	0.001732 ± 0.000246
1959	2013	0%	-0.7919 ± 0.1553	-0.6731 ± 0.1692	-17.2937 ± 3.6948	0.001870 ± 0.000470
1962	2013	36.98 %	-1.0904 ± 0.2075	-0.9268 ± 0.2284	-25.4486 ± 5.3318	0.002574 ± 0.000635
1981	2013	41.8%	-1.0628 ± 0.1808	-0.9034 ± 0.2020	-22.6817 ± 4.3110	0.002509 ± 0.000561
2007	2013	0%	-0.1843 ± 0.0650	-0.1567 ± 0.0669	-5.3034 ± 1.9242	0.000435 ± 0.000186
2017	2013	0%	-0.0031 ± 0.0143	-0.0027 ± 0.0143	-0.1138 ± 0.5181	0.000007 ± 0.000040

Table 5.7: Evolution of glacier features of a local region of Folgefonna from 1937 to 2017

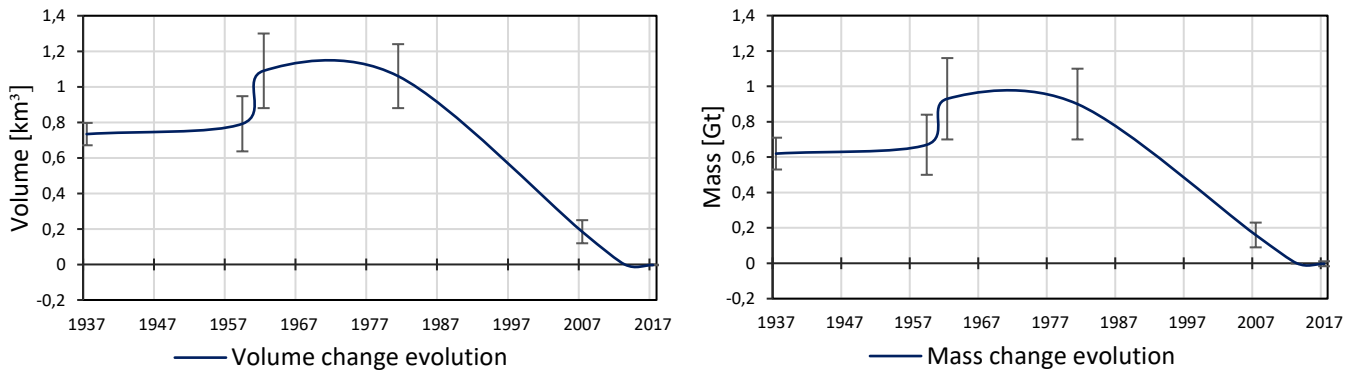


Figure 5.13: Evolution of the volume and mass for a local region of Folgefonna

5.1.5 Gravimetry– GRACE

In this part, Folgefonna and a second glacier named Drangajökull are analyzed through gravimetry.

5.1.5.1 Folgefonna results

Two methods of processing are used for the three ice caps of Folgefonna. The Center for Space Research (CSR) carried out the first processing method. The graph in Figure 5.14 presents the measured mass of water from April 2002 to December 2021. Two moving averages are calculated (1 and 2 years). During the entire period, the mass of water remains stable. Yet, four phases can be observed¹⁷. From 2003 to 2008, the mass of water increased by 48Kt for the one–year moving average. From 2008 to 2010, it decreased by 48Kt, while the period from 2010 to 2019 is stable. From 2019 to 2020, there is a significant increase (+70.5 Kt), and in the following short period (from 2020 to 2021), a substantial decrease is observed (–67.6Kt).

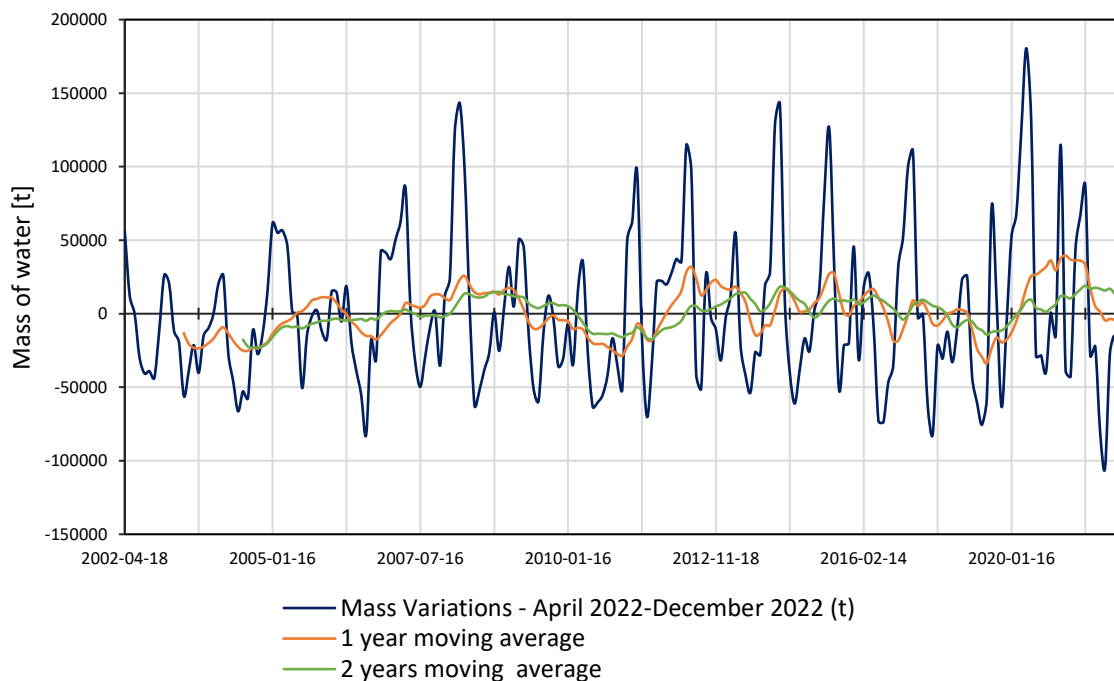


Figure 5.14: Gravimetric water mass variation of Folgefonna – by the center for space research (CSR) – from April 2002 to December 2021

¹⁷ Analysis of the two moving averages

NASA's Jet Propulsion Laboratory (JPL) carried out the second method, which is presented in Figure 5.15. The global variation is similar to the CSR evolution for the entire period (from 2002 to 2021). Three increasing and three decreasing phases are observed for the one-year moving average.

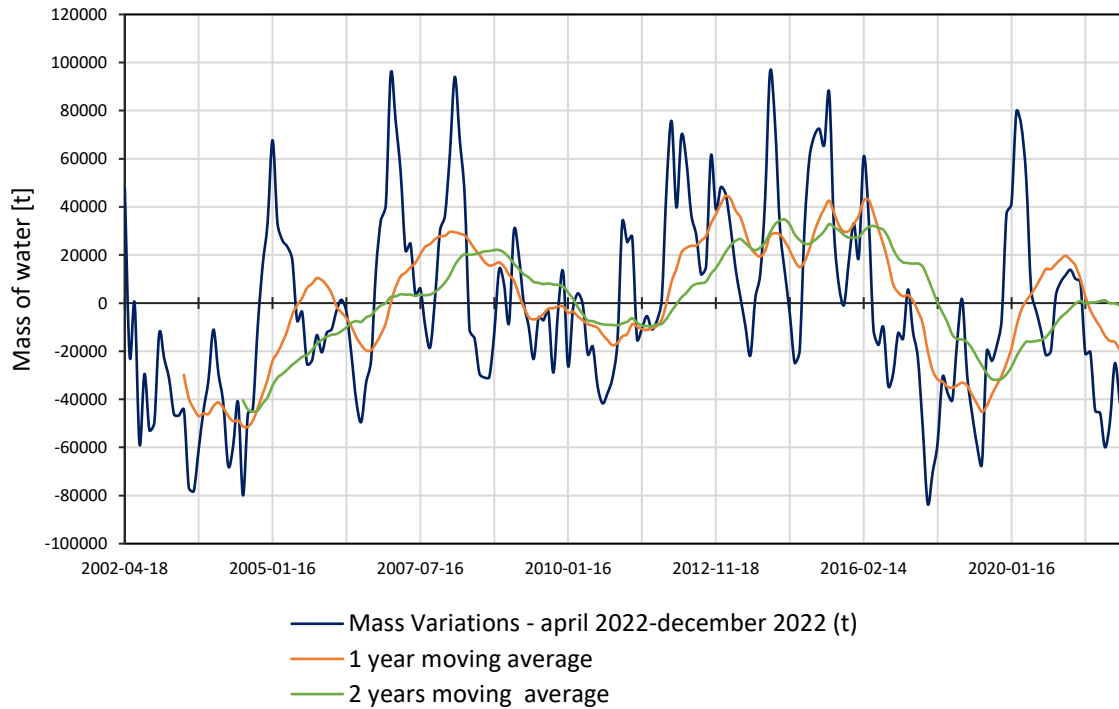


Figure 5.15: Gravimetric water mass variation of Folgefonna – by the NASA's Jet Propulsion Laboratory (JPL)– from April 2002 to December 2021

5.1.5.2 Drangajökull results

This section compares the results of a stable water mass evolution of Folgefonna to a glacier with a similar surface area, altitude and shape. The chosen glacier is Drangajökull, an ice entity located northwest of Iceland.

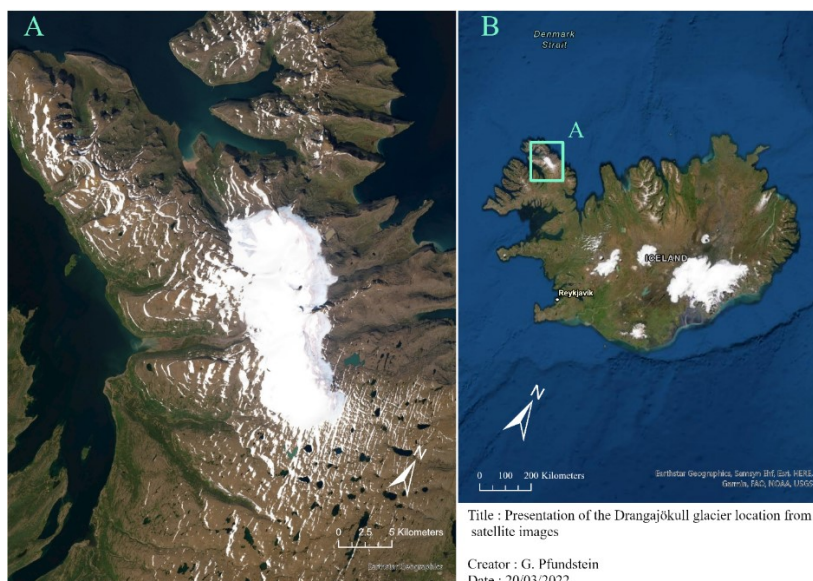


Figure 5.16: Presentation of Drangajökull's location from satellite images

The water mass evolution is calculated for the same period as Folgefonna – from April 2002 until December 2021. Both methods, CSR (Figure 5.17) and JPL (Appendix A.13) are analyzed. For CSR, from 2003 to 2021, a decreasing water mass phase is noticeable, estimated at 215Kt for the one-year moving average.

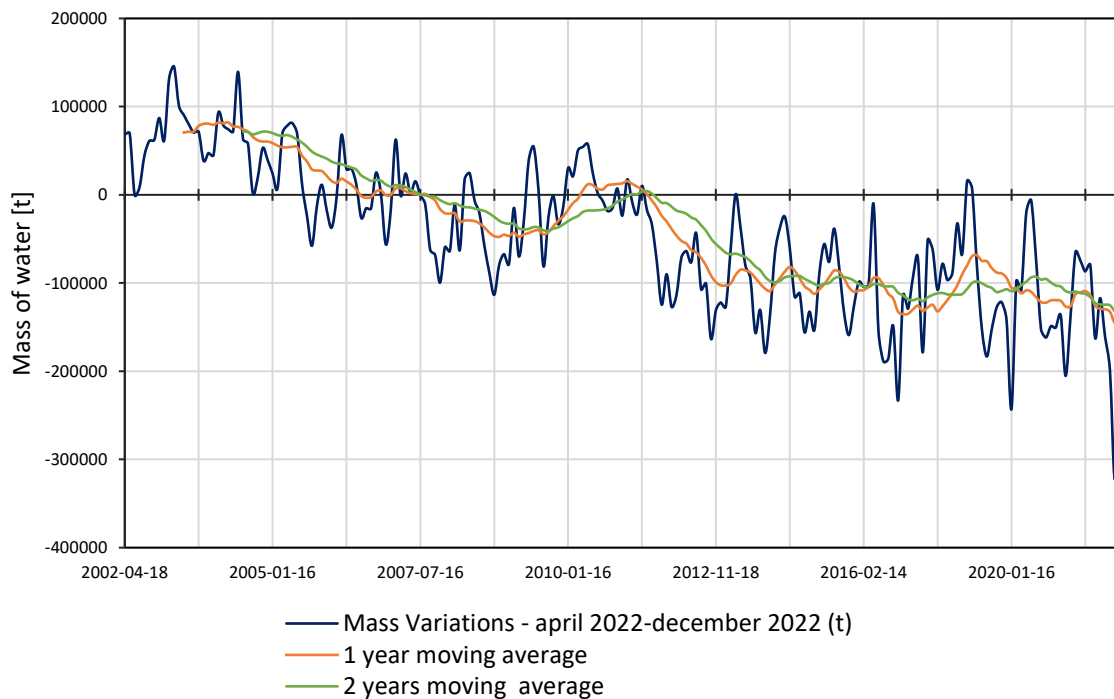


Figure 5.17: Gravimetric water mass variations for Drangajökull – by the Center for Space Research (CSR) – from April 2002 to December 2021

5.2 Results with the Eagloo software

This chapter presents the final functions implemented in the EAGLOO software to process the DEMs¹⁸.

The below illustration is a simplified model of the software.



EAGLOO
DEM Modification Software

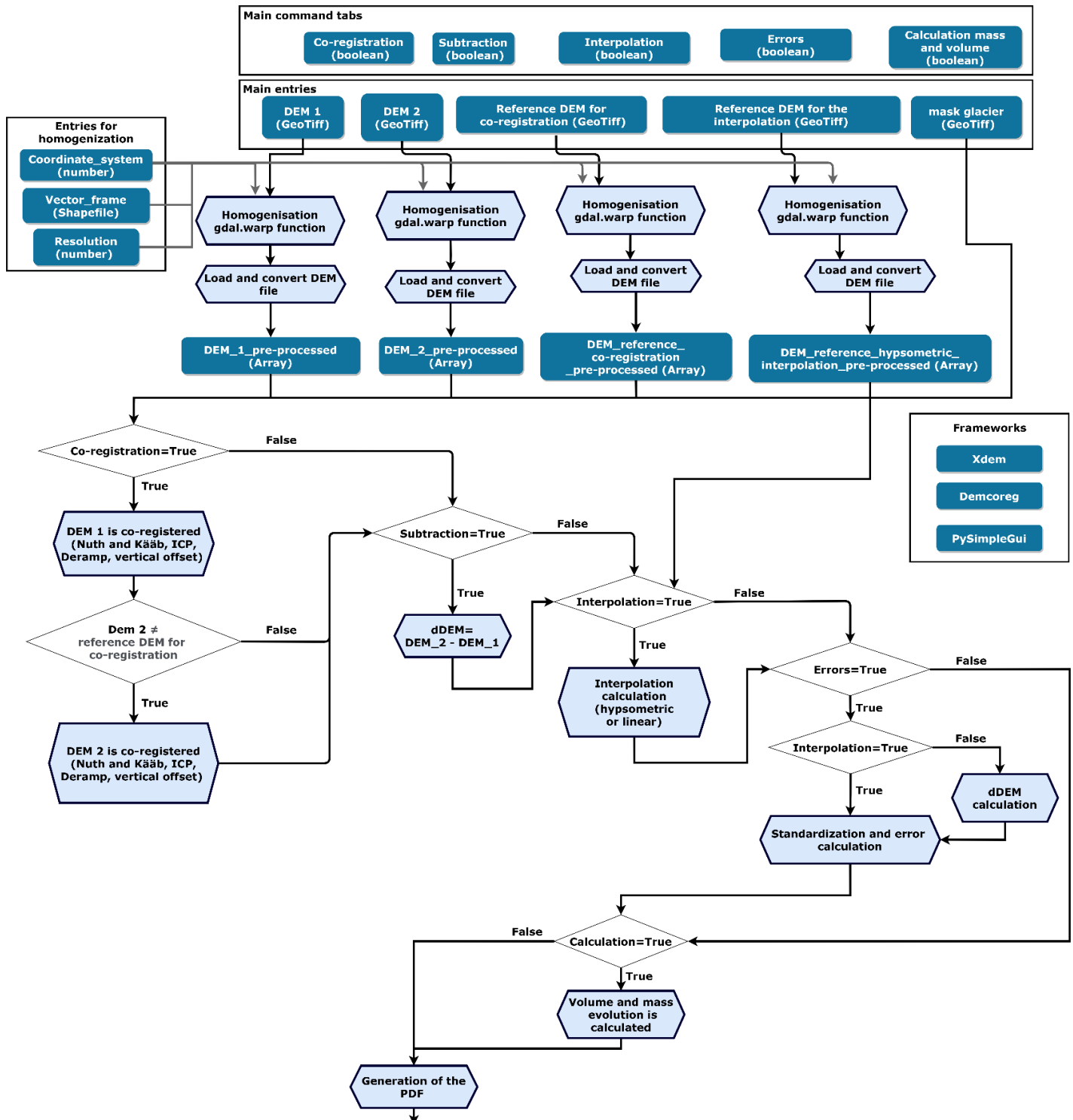


Figure 5.18: Simplified diagram of the EAGLOO software.

¹⁸ Appendix A.14 presents the frontend of the software.

5.2.1 Layer homogenization

Homogenization is a common step for each procedure; it allows the calculations between different DEMs by applying a standard resolution, a coordinated system and the same number of pixels. The necessary entries are a coordinate system, a shapefile layer containing a polygon of the entire study area and the resolution. These parameters are used to homogenize all DEMs. Given that DEMs are array files, the resolution and the frame must be the same for a mathematical operation per pixel. However, an upcoming version of the software will eliminate these requirements.

5.2.2 Co-registration

5.2.2.1 Selection of co-registration methods

Several co-registration combinations are compared to implement the most effective process in the Eagloo software. The Normalized Medium Average Deviation (NMAD) was compared between four DEMs.

The DEMs were co-registered on the Høydedata DEM from 2017 (aerial LiDAR). The compared DEMs are the following:

- 1937: DEM carried out with photogrammetry (high noise)
- 1959: DEM carried out by interpolation
- 2007: DEM carried out by LiDAR (low resolution, relatively noisy and containing significant vertical biases)
- 2013: DEM carried out by aerial LiDAR (high resolution – 1m and low noise)

	NMAD: 1937–2017 [m]	NMAD: 1959 – 2017 [m]	NMAD: 1962–2017 [m]	NMAD: 1981–2017 [m]	NMAD: 2007 – 2017 [m]	NMAD: 2013 – 2017 [m]
Before Co- registration	9.34	7.68	15.462	12.42	8.48	1.63
Nuth and Kääb	8.81	6.74	15.08	11.39	7.31	1.49
ICP	10.69	9.87	13.35	8.77	7.79	1.57
ICP + Nuth and Kääb	<u>8.44</u>	7.30	<u>12.39</u>	<u>6.38</u>	<u>6.30</u>	<u>1.42</u>
Nuth and Kääb + Deramp(degree=1)	9.65	<u>6.58</u>	14.34	6.64	29.46	4.61
Deramp(degree=1) + Nuth and Kääb	9.04	6.63	14.24	6.57	26.66	4.56
Vertical offset + ICP + Nuth and Kääb	8.45	7.29	12.39	6.38	6.30	1.42
ICP + Nuth and Kääb + Deramp(degree=1)	9.69	7.22	14.02	6.52	29.74	4.55
Deramp(degree=1) + ICP + Nuth and Kääb	8.46	7.3	12.42	6.38	6.32	1.42
ICP + Deramp(degree=1) + Nuth and Kääb	8.79	7.47	14.12	6.54	26.78	4.55
Test resolution [m]	8	8	10	10	10	10

Table 5.8: Normalized Median Average Deviation (NMAD) as a function of the methods

5.2.2.2 Final entries, processes and output of co-registration

- Entries: To launch the co-registration, the user ticks the first box. At least two DEMs are necessary; one is used to co-register, and the other is the reference. If no latest DEM is inserted in the main entries tab, a reference DEM has to be inserted in the co-registration tab. However, if a latest DEM is inserted in the main entries tab, it is unnecessary to insert a reference DEM, as the latest DEM will become the reference. Two co-registration calculations will be launched if three DEMs are introduced, and the latest DEM differs from the reference DEM.
- Process: Eagloo currently implements the nine following methods:
 - Nuth and Käab (Nuth and Käab, 2011) (translation: x,y) + Bias correction(translation: z)
 - Iterative closest point (ICP)
 - ICP + Nuth and Käab (for large rotations)
 - Vertical shift + ICP + Nuth and Käab (for large biases, rotations and high amounts of noise)
 - Nuth and Käab + Deramp (for small rotations)
 - Vertical offset + ICP + Nuth and Käab
 - ICP + Nuth and Käab + Deramp(degree=1)
 - ICP + Deramp(degree=1) + Nuth and Käab
 - Deramp(degree=1) + ICP + Nuth and Käab
- Output: The principal output is the co-registered DEMs (.tif). The second output is the elevation graphs (.png) presenting the difference between the reference DEM and those co-registered before and after the co-registration.

5.2.3 Subtraction

This step is optional. It is a pixel subtraction between the latest and earliest DEM.

- Entries: To launch this calculation, the user ticks the corresponding box. After that, two options are currently available. If a co-registration was previously calculated on Eagloo, the co-registered DEM is used as default. If no co-registration was made, the user's earliest and latest DEM inserted are used.
- Process: The earliest DEM is subtracted from the latest DEM (dDEM=latest DEM – earliest DEM), followed by the creation of the corresponding graph.
- Output: A difference DEM (dDEM)(.tif) and a graph of the dDEM(.png) is exported.

5.2.4 Interpolation

Interpolation is a fundamental step to fill voids on a DEM. In this software, the interpolation is always calculated on a dDEM, and a reference DEM is therefore required. If a co-registration is necessary, the user should compute it before the interpolation.

- **Entries:** If the dDEM has not been calculated, the following calculation is automated: $dDEM = \text{latest DEM} - \text{earliest DEM}$. If the subtraction was previously done, the calculated dDEM is directly used. Otherwise, the user must input the dDEM.
- **Process:** Only three methods are currently implemented:
 - Linear interpolation
 - Regional hypsometric interpolation
 - Local hypsometric interpolation

For the linear interpolation, the option to choose the radius will be added to an upcoming version.

The hypsometric interpolation method is based on the assumption of a relationship between the elevation and the change in elevation of the dDEM (section 3.1.5.2.2). The principle is the same for regional and local methods. For each altitude, the difference in elevation from the reference DEM and the dDEM to interpolate is averaged.

However, the difference between the regional and local hypsometric interpolation is the following:

- For **regional hypsometry**, the glacier outlines inputted in the main entries tab are used for the hypsometric initialization. This method is specifically adapted for small glaciers or large voids. However, no distinction is made between the south and north exposition, which means that the elevation changes at a specific altitude will be the same for any exposition.
 - For **local hypsometry**, the user uses a shapefile layer with a polygon of a specific glacier section. Currently, if the shapefile contains several polygons, the algorithm will read it as a single polygon. The main advantage of this method is the accuracy of the catchment and/or the exposition differentiation.
- **Output:** The main output is the interpolated dDEM. If hypsometric interpolation is selected, then a graph of the dDEM before and after the co-registration is also created.

5.2.5 Errors based on slope and curvature

The errors of a dDEM are calculated based on the stable ground around the glacier through a correlation between slope/curvature and altimetric shift per pixel.

Four types of errors can be calculated:

- Spatial unstandardized errors
 - Spatial standardized errors
 - Integrated errors (with standardization)
 - Mean errors (with standardization)
- **Input:** The user ticks the corresponding box to launch the calculation of the errors. If the user wishes to calculate the spatial unstandardized error or the spatial standardized integrated error, the associated box has to be ticked. After that, a reference DEM can be inserted. If left empty, the latest DEM input in the main entries tab is used. If the user has already calculated a dDEM, it can be inserted. To calculate the mean and integrated errors of a specific area, the user must tick the corresponding box and select the shapefile with the outlines of the glacier where the errors are to be calculated.

- **Process:** The primary process is the error calculation based on the assumption of a correlation between the values of a dDEM and the slope/curvature of a reference DEM.
 - If standardization is ticked, the dDEM is standardized – which means the standard deviation is equal to 1, and the average is equal to 0. Using standardization is encouraged as it linearizes the data.
 - After a three-dimensional file is calculated on the stable ground, it contains the following features: slope, curvature and elevation change (this step is typical for standardized and unstandardized data).
 - As the slope and curvature are computed from the reference DEM, the elevation change is applied using the three-dimensional files previously calculated. The spatial standardized or/and unstandardized error is calculated.
 - If the integrated and mean error is desired for a specific glacier, the average of the standardized spatial error and the integrated error is calculated within the glacier outlines from the inserted shapefile.
Note: this calculation is currently only available for standardized spatial calculation.
- **Output:** If the spatial and/or unstandardized spatial errors are ticked, the dDEM is exported, depending on the user's expectation. Variograms of the three-dimensional file (slope, curvature, elevation change) and graphs of the spatial standardized and unstandardized errors are exported.

5.2.6 Mass and volume calculation

The final step is where the evolution of the glacier's features is calculated. It contains the volume change, the mass change, the meter water equivalent difference and the resulting sea-level rise.

- **Entries:** This process solely requires the dDEM. The user can choose between the following three:
 - the dDEM calculated in the subtraction
 - the dDEM calculated in the interpolation
 - a previously calculated dDEM.

The ice density must be known to convert the volume change into mass change. By default, it is 850kg/m³. However, another value can be set.

The last line of the associated dialogue tab allows for the automatic computation of associated errors for each calculation. The user must tick the associated box and input the ice density and glacier outline error.

- **Process:** It contains six calculations:
 - The **period** is calculated from the name of the dDEM. If there are two dates, the subtraction of the two dates is automatic. The period is used to calculate the evolution per year.
 - The **area** is calculated by multiplying the number of pixels inside the glacier area by the resolution.
 - The **volume change** is calculated using equation 4.6, where each pixel value of the dDEM is multiplied by the squared resolution and summed.
 - The **mass change** is directly calculated by multiplying the ice density by the volume change calculated through equation 4.7.
 - The **meter water equivalent** is calculated by dividing the mass balance per glacier area and water density (equation 4.8).

- The **contribution to sea-level rise** is calculated directly from the mass change. The computation uses the oceans of 361.8 million km²; thus, 1 mm is equivalent to 361.8Gt (or 361.8km³). The mass change (in Gt) is divided by –361.8 (equation 4.9).

If selected, the error is calculated for all the above features.

- **Output:** The period, surface area, volume change, mass change, meter water equivalent and contribution to sea-level rise are produced with the associated errors if selected.

5.2.7 PDF report generation

For each calculation, a report is automatically generated.

- **Entries:** In the last tab of the main dialogue, the user inputs the location where the final report is saved.
- **Process:** The report is generated, at least one process must have been launched (co-registration, subtraction, interpolation, errors, volume and mass change calculations). An example of a report is shown in Appendix A.15.
- **Output:** The file is saved in the indicated location, and a pop-up offers the user to open the PDF report directly.

5.3 Climatic data and correlation

This section provides the results of the correlation calculation; in the first part, the climatic data is presented, and the final correlation calculations are described in the second part.

5.3.1 Climatic data

The data is downloaded from 1931 to 2021. The historical temperature data is analyzed from the station of Bergen Florida; this data is presented in Figure 5.19. A 10-year moving average is calculated. For the entire period (1941–2021), the linear temperature elevation is evaluated at $+0.01^{\circ}\text{C}/\text{year}$ $\left(\frac{T_{2021}-T_{1941}}{2021-1941}\right)$.

Three tendencies are observed on the moving average. From 1941 until 1970, the temperatures decreased by 0.61°C , and the linear temperature evolution is $-0.021^{\circ}\text{C}/\text{year}$. From 1970 until 1986, the temperature was relatively stable. Then, from 1986 until 2021, the temperature rose by 1.33°C , from 7.45°C to 8.78°C , with an annual temperature increase of 0.038°C .

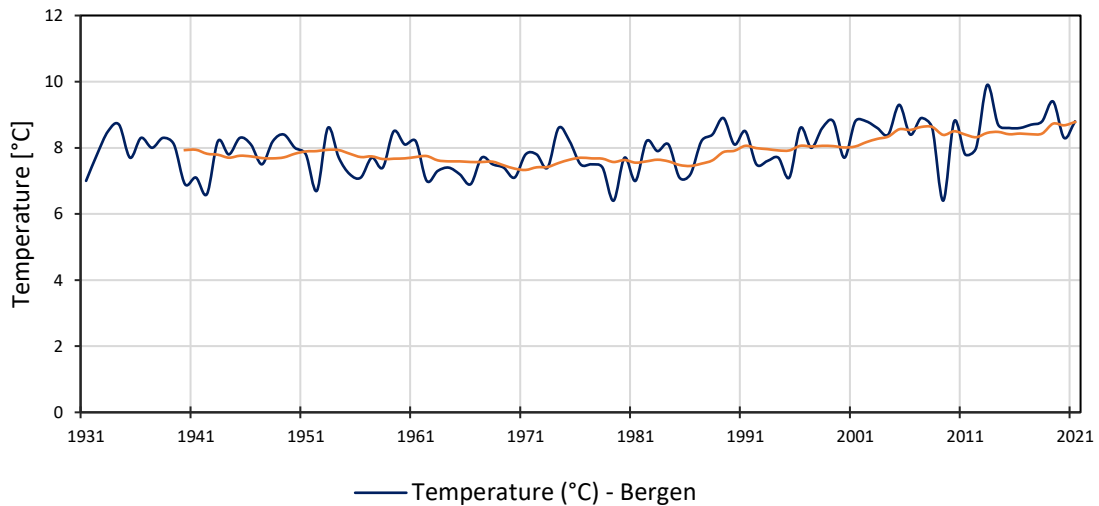


Figure 5.19: Temperature as a function of time from 1931 to 2021 – Bergen Florida station

Concerning the precipitations, the Rosendal station has been chosen. The associated data can be seen in Figure 5.20. Similarly to the temperature, the moving average is also calculated for ten years. For the following analysis, only the moving average was used.

For the whole period (1941–2021), yearly precipitations increased by 446mm (+4.82 mm/year).

Two periods can be identified. From 1940 to 1966, the precipitations decreased by 161.41mm (–5.78mm/year). Then, from 1968 to 2021, a long phase of increase is observable; the precipitations increased by 607.8mm (+10.53mm/year), 39.1% of the yearly precipitation in 1968.

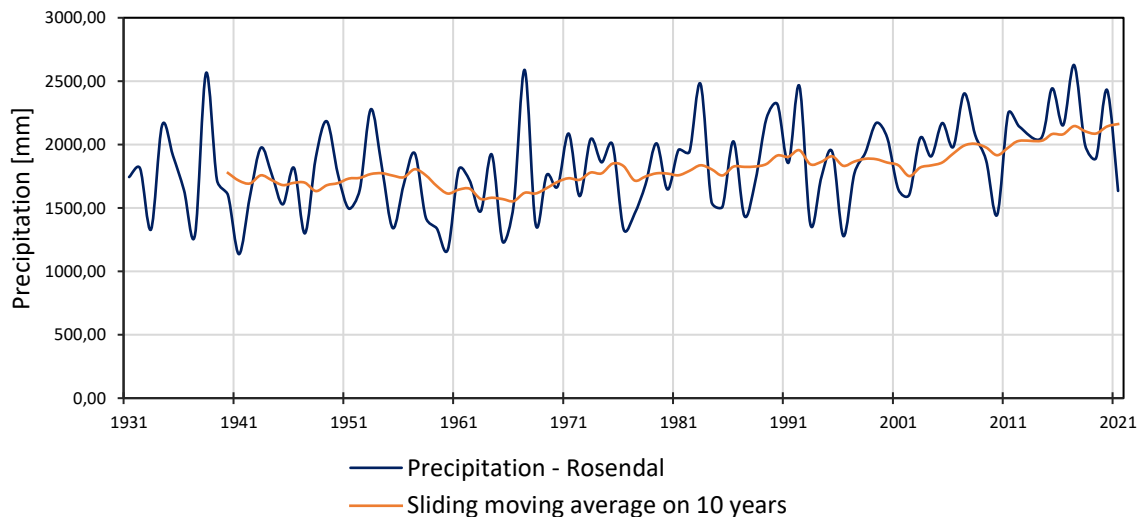


Figure 5.20: Precipitation as a function of time, from 1931 to 2021 – Rosendal Station

The mean cloud coverage was analyzed (Figure 5.21) while not used in the correlation calculation. As for the temperature and precipitations, a 10–year moving average was calculated and used in the following analysis. The meteorological station is the one in Bergen.

From 1967 to 2021, the mean cloud coverage has slightly increased by 0.18okta (+0.003 okta/year).

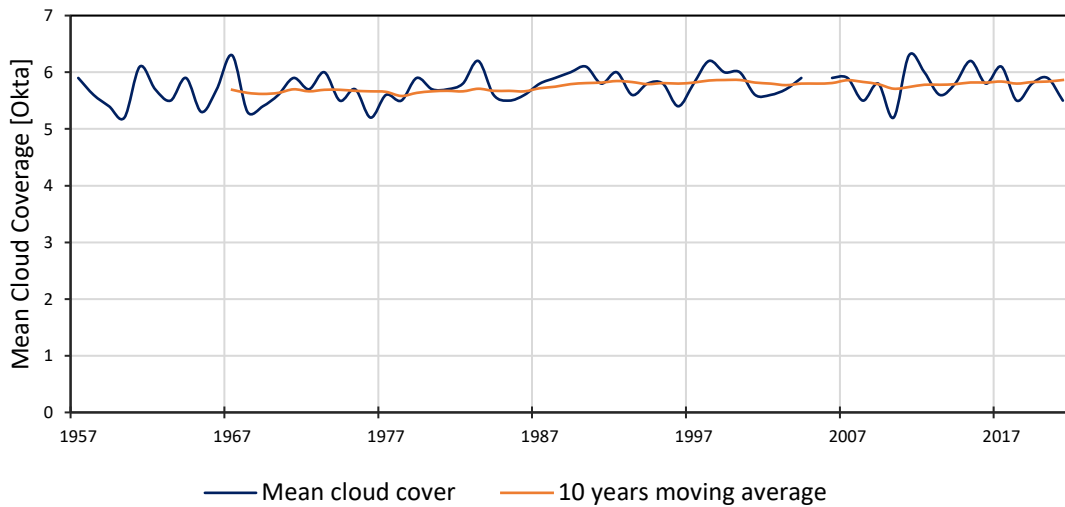


Figure 5.21: Mean cloud cover as a function of time, from 1937 to 2021 – Bergen Florida station

5.3.2 Correlation between glacier features and climatic data

This section presents the final correlation calculations between the climatic data (section 5.3.1) and the feature evolution of Folgefonna (section 5.1).

5.3.2.1 Correlation between glacier outlines and climatic data

Figure 5.22 presents a graph of the data used to calculate the correlation between the glacier area and climatic data (section 5.3.2.1.1), and between the ELA and the climatic data (section 5.3.2.1.2). The climatic data is calculated yearly as the ELA and glacier area are calculated within the same period.

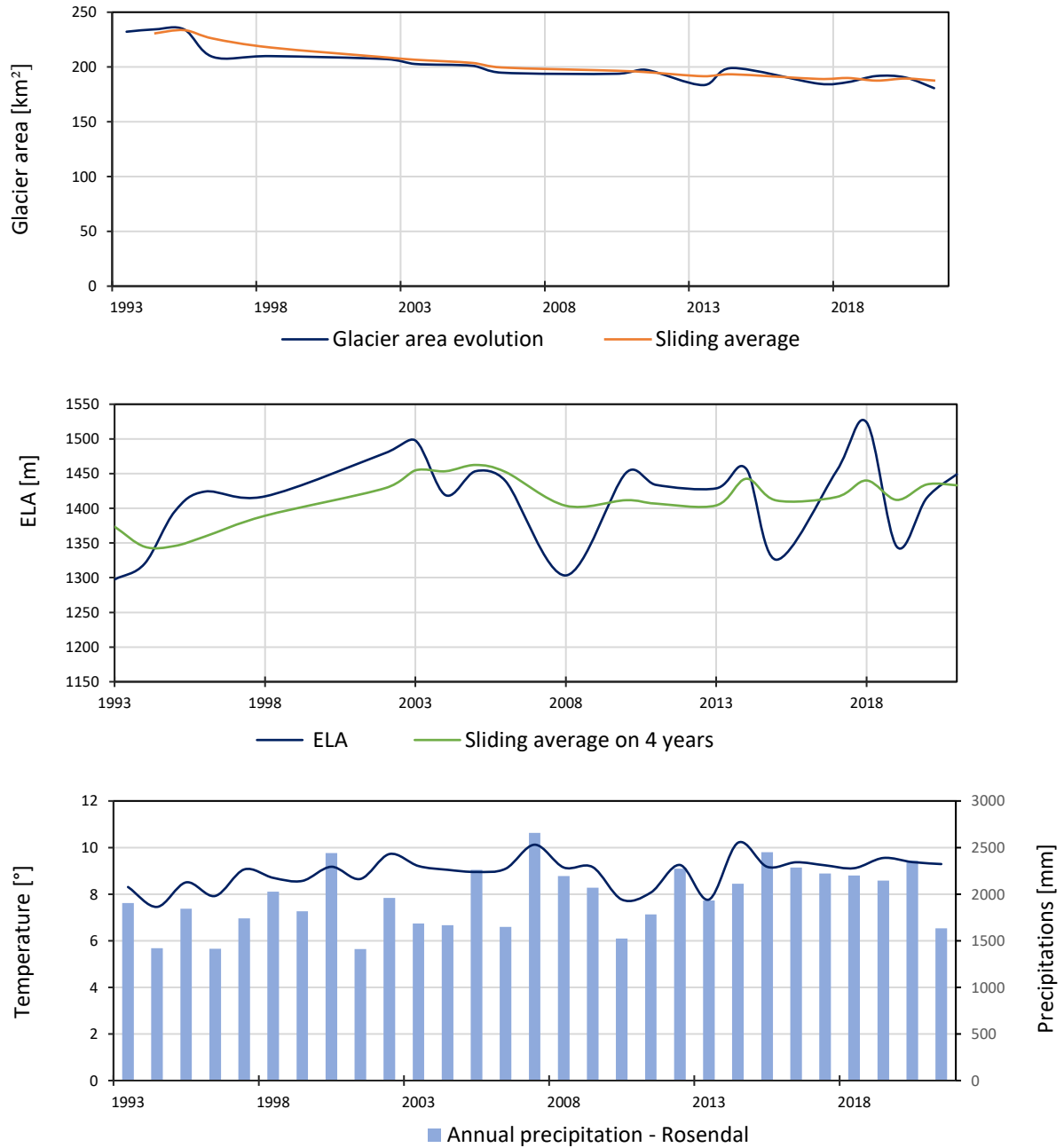


Figure 5.22: Comparison of glacier features and climatic data for the correlation between the glacier area, the ELA and climatic data.

5.3.2.1.1 Glacier area and annual climatic data

Several combinations were calculated for the glacier area (graphs 1 and 3 in Figure 5.22). The results are the following:

- between the glacier outlines and annual temperature: $r = -0.73$
- between the glacier outlines and annual precipitation: $r = -0.42$
- between the glacier outlines and the moving average of temperature for three years: $r = -0.72$
- between the glacier outlines and the moving average of precipitation on three years: $r = -0.70$

The following correlations are produced with the seasonal climatic data. The summer temperature is the average of June, July, August and September, and the winter precipitations represent the sum of November, December, January, February and March. The results are the following:

- between the glacier outlines and the three-year moving average summer temperature: $r = -0.78$
- between the glacier outlines and the moving average winter precipitations: $r = 0.42$

5.3.2.1.2 ELA and climatic data

For the ELA (graphs 2 and 3 of Figure 5.22), only four correlations are calculated:

- between the raw ELA and the temperatures: $r = 0.20$
- between the raw ELA and the precipitations: $r = -0.13$
- between the ELA moving average and the temperatures: $r = 0.67$
- between the ELA moving average and the precipitations: $r = 0.30$

5.3.2.2 Correlation between GRACE data and climatic data

The GRACE data (Figure 5.23) was collected from April 2002 to December 2021. The climatic data was calculated monthly from the available GRACE data. Indeed, the precipitations are summed, and averages are calculated for the temperatures for periods lacking data.

Three correlations are computed;

- 1 For the monthly data, correlations are the following:
 - between GRACE data and the precipitations: $r = 0.02$
 - between GRACE data and the temperature: $r = 0.41$
- 2 For the yearly data, correlations are the following:
 - between GRACE data and precipitations: $r = 0.42$
 - between GRACE data and temperature: $r = 0.22$
 - between GRACE data and precipitation divide per the temperature: $r = -0.42$
- 3 For the data calculated with the temperatures from June to September and precipitation from November to March, correlations are the following:
 - between the yearly GRACE data and precipitations from November to March: $r = 0.48$
 - between the yearly GRACE data and temperatures from June to September: $r = 0.35$
 - between the yearly GRACE data and precipitations from November to March divided by the temperatures from June to September: $r = 0.48$

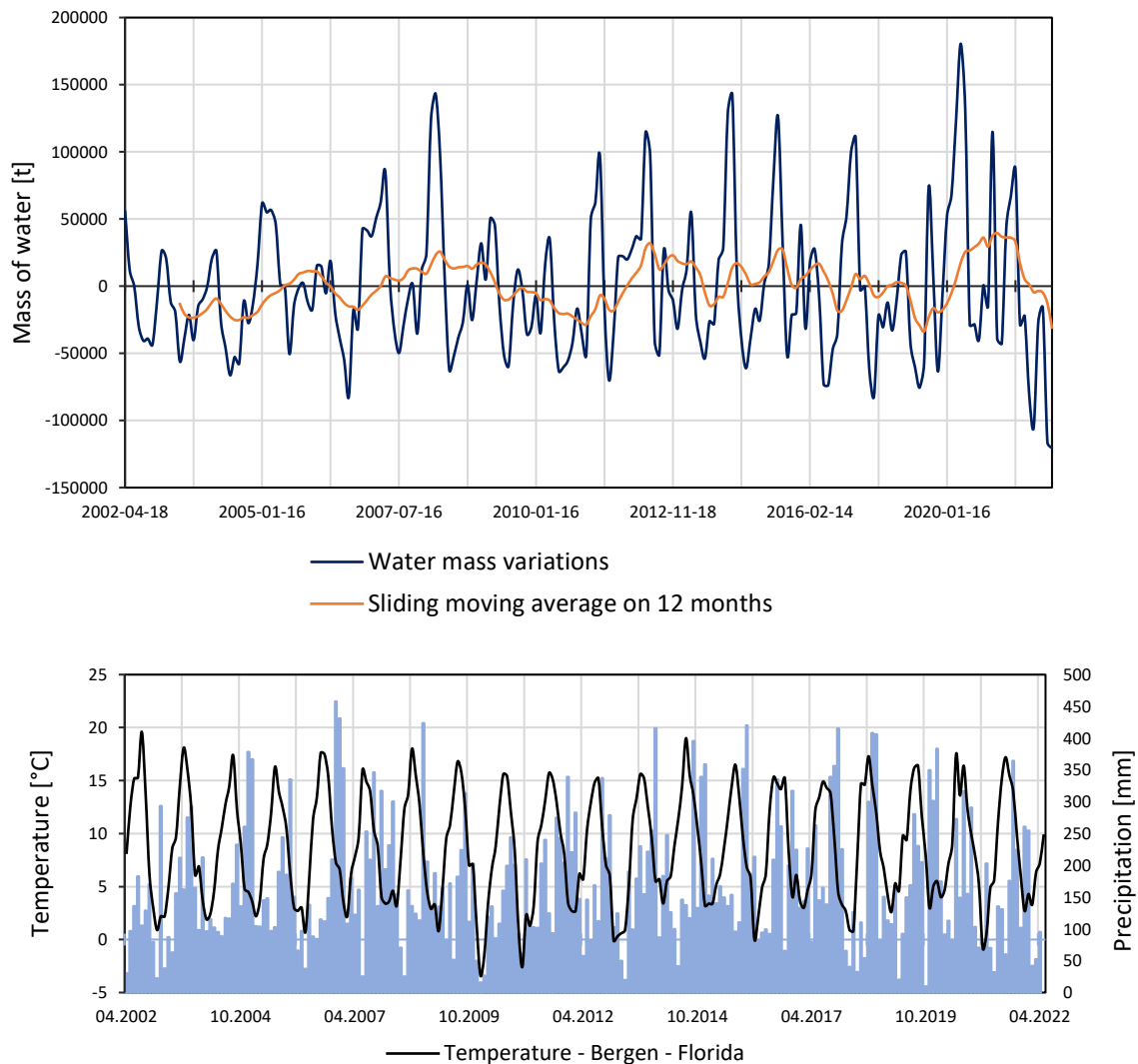


Figure 5.23: Correlation between GRACE data and temperatures of the Bergen station and the precipitations of the Rosendal station

5.4 OGGM results

A historical and future evolution of the glacier is calculated with the Open Global Glacial Model (OGGM).

5.4.1 Historical evolution

The past evolution is computed for the period from 1902 to 2021. The volume evolution (Figure 5.24) of three ice caps of Folgefonna increased by 1.7km^3 during the entire period, representing 6.0% of the volume in 1902. However, four phases can be observed. In the first, from 1902 to 1934, the volume increased by 1.7km^3 . Then, from 1934 to 1967, the glacier was reduced by 1.2km^3 . From 1967 to 2002, the glaciers increased by 1.8km^3 . And lastly, from 2002 to 2020, it increased by 0.6km^3 .

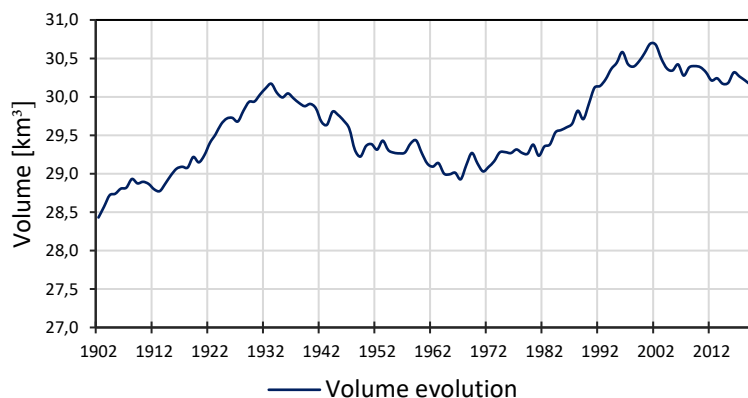


Figure 5.24: Evolution of the volume of the three ice caps of Folgefonna from 1902 to 2021

The glacier area (Figure 5.25), from 1902 to 2021, decreased by 4.85km², 2.4% of the surface area in 1902. From 1902 to 1945, the glacier area increased by 0.41km²; however, it slightly decreased before increasing. For the entire period, this feature increased by 0.41km². Then, from 1945 to 2021, the glacier area decreased by 5.26km².

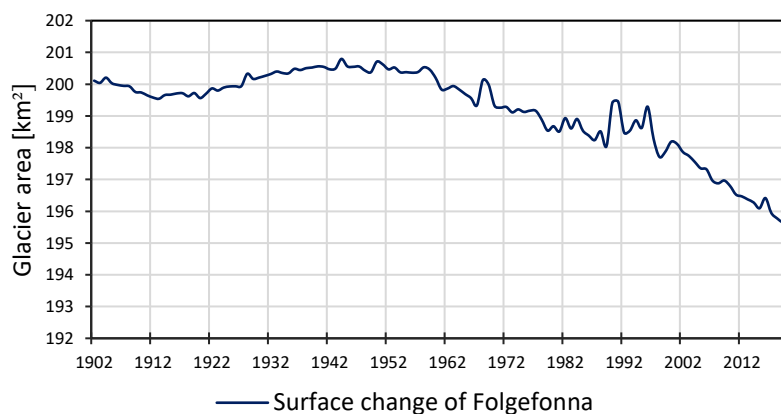


Figure 5.25: Surface evolution of the three ice caps of Folgefonna between 1902 and 2021

5.4.2 Future evolution

A model of Folgefonna's evolution from 2020 to 2100 is computed through the OGGM script. Figure 5.26 presents the volume evolution of Folgefonna. Four scenarios were used with the following outcomes:

- for **RCP 26**: the glacier would decrease by 6,5km³ (–21,6%¹⁹)
- for **RCP 45**: the glacier would decrease by 8,9km³ (–29,6%)
- for **RCP 60**: the glacier would decrease by 9,1km³ (–30,3%)
- for **RCP 85**: the glacier would decrease by 11,1km³ (–37%)

¹⁹ The volume of 2020 is used as an uncertainty is to use the three–cornered reference for all scenarios.

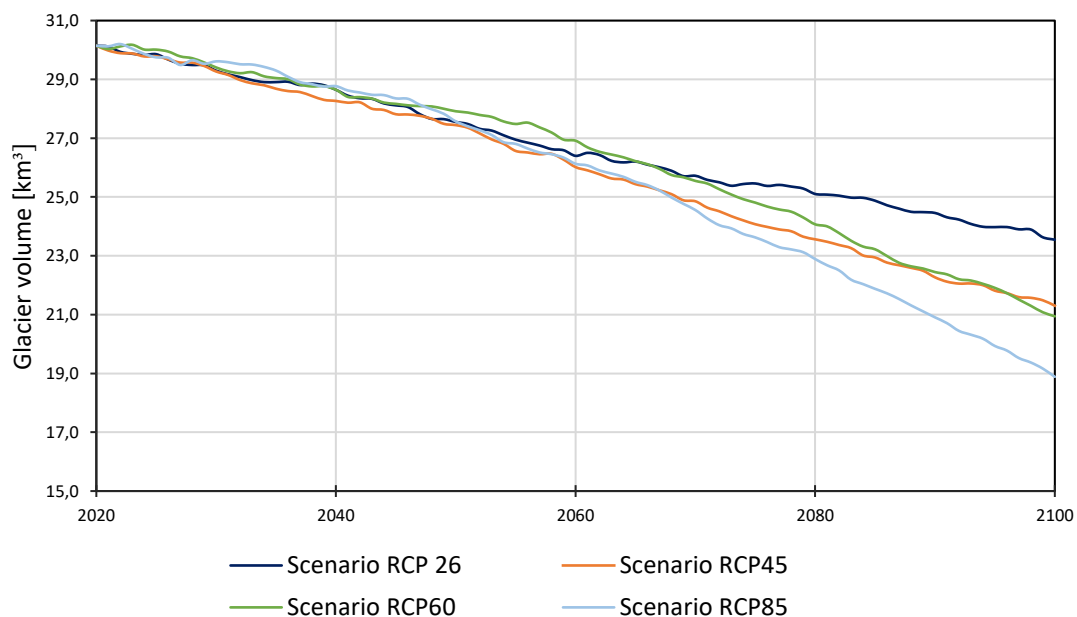


Figure 5.26: Evolution of the three ice caps of Folgefonna, from 2022 to 2100 calculated with OGGM

Figure 5.27 illustrate Folgefonna's area evolution in the different scenarios with the following results:

- for **RCP 26**: the glacier would decrease by 38,8km² (–19.8%²⁰)
- for **RCP 45**: the glacier would decrease by 47,6km² (–24.3%)
- for **RCP 60**: the glacier would decrease by 47,6km² (–24.5%)
- for **RCP 85**: the glacier would decrease by 58km² (–29.7%)

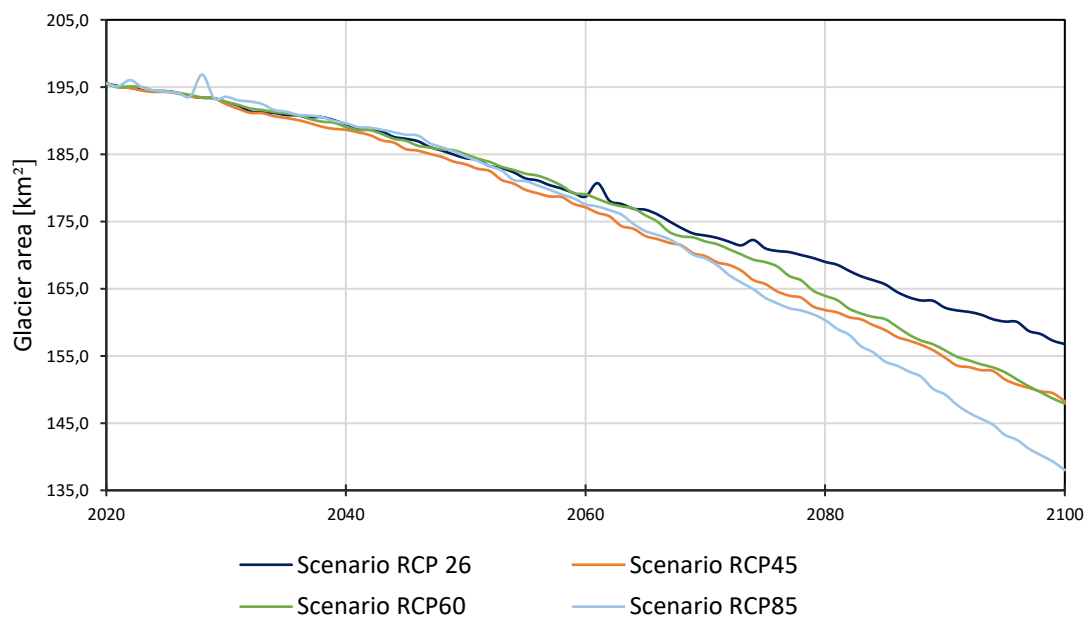


Figure 5.27: Glacier area evolution from 2022 to 2100.

²⁰ The volume of 2020, is used as reference for all scenarios.

Chapter 6

Analysis and discussions

This chapter discusses the methodology and analyzes the outcomes of this research.

6.1 Methods and results discussion

This section discusses the methods and data of Chapter 4 and the results of Chapter 5.

6.1.1 Evolution of glacier area, TSL and snow coverage

Given that the evolutions of the glacier area, ELA and snow coverage are calculated from identical satellite images, similar limitations are found.

6.1.1.1 Glacier area

The primary discussion path for the glacier area concerns the uncertainty induced by natural hazards. Only the uncertainty associated with the NDSI was used. It would be interesting to compute the following uncertainties:

- **Snow coverage:** This feature was considered by applying a manual filter (years with significantly high snow coverage were deleted).
- **Resolution:** The photographs used are satellite images with a lower resolution than aerial images. A higher resolution of 10m (Sentinel-2) is used for the calculations between 2014 and 2022. Before 2014, Landsat bands are used, with a resolution of 30m.
- **Cloud coverage:** Some images show high cloud coverage depending on the period. This increases the uncertainties in glacier area measurement.

6.1.1.2 Evolution of the ELA

There are two points of discussion for the ELA. The first one is related to the period of the year when the photographs were taken. Similarly to the glacier area, the other is the uncertainty.

6.1.1.2.1 Temporality

The highest TSL of a year should be photographed to infer the most accurate mass balance from ELA. It is, therefore, necessary to have a glacier image on the day marking the end of the ablation season and the beginning of the accumulation season. However, as the images were taken from Sentinel 2 and Landsat, no daily images are available, and there often is high cloud coverage. Thus, the used images were taken from the beginning of August to the end of October. Having highly accurate mass balance results from the data is difficult.

6.1.1.2.2 Uncertainties

Only the uncertainty associated with the NDSI is used. For an improvement in accuracy, it would be relevant to compute the following others:

- **Temporality:** Nearly all the ELA could not be calculated from the last day of ablation. Thus, an error related to the date of the highest ELA of the year could be included to improve the global uncertainty.
- **Resolution:** The resolution is relatively low compared to aerial images; adding the associated uncertainty can be interesting.
- **Cloud coverage:** As for the glacier area evolution, the cloud density increases the level of uncertainty as the clouds may hide the ELA.

6.1.1.3 Snow coverage

For the snow coverage, the main elements of discussion are the same as those for the evolution of the ELA: *temporality* and *uncertainties* (section 6.1.1.2).

6.1.2 DEM evolution

The discussion elements for the DEM evolution are the periods between each DEM, the photogrammetric processing, co-registration, interpolation, errors calculation and conversion between the volume and mass change.

6.1.2.1 Period between each DEM

Two evolutions were calculated to monitor the glacier by DEM. The first one (Table 5.5) was from 1959 to 2017. As there was no DEM between 1959 and 2007, observing the corresponding evolution is impossible. However, other studies and results from 1959 to the mid-1990 show a slight increase in the mass of the glacier, followed by a subsequent decrease.

For the evolution calculated on a smaller region (19.52% of the surface area of 1959) (Table 5.7), the period is more extensive than for the evolution of the three ice caps (100% of the glacier's surface area in 1959). It would have been relevant to compute another DEM for the mid-1990; however, no data is available between 1981 and 2007.

6.1.2.2 Photogrammetric processing

The central problem in photogrammetric processing is the presence of voids in the glacier's center caused by the snow coverage in the black and white photographs (255 colors). Images containing a considerable section with the same pixel value make photogrammetric processing impossible on Metashape. It could be interesting to carry out a full try on OrthoEngine (Catalyst) for a DEM with poor results (i.e. 1981). This was not executed due to the extensive number of required waypoints on OrthoEngine.

6.1.2.3 Co-registration

The iterative closest point (ICP) coupled with the Nuth and Kääb algorithm has the highest NMAD, six times. The method with the Nuth and Kääb algorithm exclusively performed best once. The final NMAD fluctuates between 1.18m (for 2013) to 12.39m (for 1962) – yet only one year is below 5.15m. All other values of NMAD are above. As it is relatively high, finding a way to decrease the NMAD on each DEM could be interesting. For this, further co-registration combinations could be tested.

6.1.2.4 Interpolation

The hypsometric methods are efficient for interpolation. However, the function implemented in Eagloo could be improved.

6.1.2.5 Error calculation

The integrated errors calculated on the stable ground were used to estimate the errors. These are calculated assuming a correlation between slope + curvature and the shift in altitude. However, reanalyzing this process could be relevant as the corresponding error is most likely underestimated.

Only ice density and surface area uncertainties were considered for the volume and mass calculations. However, this error calculation could include other types of uncertainties, such as the wave penetration in the snow from LiDAR and RaDAR.

6.1.2.6 Conversion between the volume and mass change

To convert volume change into mass change, the ice density was defined as $850 \pm 60 \text{ kg/m}^3$, which is a linear method (section 3.1.5.3). However, as the density of ice depends on its depth, it would be interesting to use the graph in Figure 3.1 to apply the ice density as a function of depth. Moreover, the crevasses on the glacier have not been considered in the final volume and mass calculations and error estimations.

6.1.3 Gravimetry

6.1.3.1 GRACE data analysis

As portrayed in Figure 5.14, the water mass in Folgefonna seems constant from April 2002 to December 2021. Nevertheless, these results are impacted by the groundwater, water tanks and lakes around the glacier. Indeed, with GRACE one can only select a rectangular ROI. Therefore, the results also describe the mass balance evolution of the surrounding stable ground.

6.1.3.2 Uncertainties

GRACE data uncertainties were not integrated. One of the most suitable ways to estimate data processing uncertainty is to use the three-cornered hat method, described in the paper by Ferreira et al. in 2016. Estimating the following six sources of GRACE data uncertainties could be valuable (Blazquez et al., 2018):

- The processing centers
- The geocentre motion correction
- The $C_{2,0}$ correction
- The filter
- The leakage correction
- The glacial isostatic adjustment (GIA)

6.1.4 Eagloo

6.1.4.1 Potential improvements

The developed software can be improved as follows:

For the frontend: both the user interface (UI) and user experience (UX) could be enhanced. Firstly, removing the shapefile used to homogenize the DEMs would be interesting. This shapefile can be calculated from the other raster files.

For the backend: For the co-registration, it would be interesting to try other methods and compare an extensive range of DEMs. The local and regional hypsometric methods implemented in the interpolation methods seem efficient. However, particular results can be biased; a possible improvement would be to apply a filter on the “hypsometric distribution of the glacier and elevation change as a function of altitude (Figure 4.10). This filter would consistently allow removing the part of the graph with high fluctuations.

6.1.5 Folgefonna evolution

6.1.5.1 OGGM initialization

A 30m resolution DEM was used to compute the models in OGGM. Using a DEM with a higher resolution, such as the DEM provided by Høydedata in 2013 (2m resolution), would improve the results.

6.1.5.2 Correlation

The correlation between the evolution calculated with OGGM and climatic data is unnecessary as both results are derived from the precipitations and temperature data.

6.1.5.3 Uncertainties

Uncertainties were not integrated into the evolution of Folgefonna. Computing them for the RCP scenarios could be pertinent. Indeed, uncertainties in glacier projection originate from five different sources (Marzeion et al., 2020):

- Glacier model
- Climate model
- Scenario
- Internal climate
- Glacier inventory

6.1.5.4 ALPGM model

The ALPGM framework (section 4.4.2), based on a neural network method, is not used as it is trained for glaciers in the Alps. Extensive training on the model with Norwegian maritime glaciers would be necessary for an application on Folgefonna. Moreover, the volume and mass change of a wider range of similar glaciers must be known.

6.2 Analysis of the Results

From 1959 to 1993, the lack of data impairs the observation of the glacier area evolution. Nonetheless, the perceptible decrease from 1995 to 2021 ($-53.74 \pm 25\text{km}^2$, -22.92%) is coherent with the direction of the glacier area evolution calculated with the OGGM script (section 5.4.1). The DEM evolution (section 5.1.4.4) shows a similar tendency; however, due

to the lack of data in 1990 and poor correlation between the glacier area evolution and mass balance, this decreasing phase cannot be validated through DEM monitoring on the three ice caps. Nonetheless, the simulation of historical evolution calculated by OGGM shows an increase in Folgefonna's volume and mass from 1965, followed by a decrease from 2000.

The three ice caps display several differences. Søndre Folgefonna has the strongest influence on the mass evolution as it represents 84.2% of the glacier area in 2021. However, the evolution is heterogenous between the three entities. Midtre Folgefonna has the lowest average altitude, approximately 100 m under Nordre and Søndre Folgefonna – it is also the smallest. It lost 63.5% of its surface area from 1995 to 2021 ($-12.26 \pm 1.54\text{km}^2$). In comparison, Nordre and Søndre Folgefonna present a less significant decrease – Nordre Folgefonna diminished by 27.47% ($-8.61 \pm 3.30\text{km}^2$), and Søndre Folgefonna lost 15.8% ($-28.96 \pm 20.62\text{km}^2$). From 1995 to 2021, the ELA of the three ice caps rose by 88.5m.

From April 2002 to December 2021, the tendency is similar for both GRACE methods used in this study (CSR and JPL). The water mass presents a stable moving average and is not decreasing. For the extremum of CSR data, the moving average on 12 months increased by 29,817T. However, the uncertainty is relatively high as the water contained in the ground and dams for electricity are included. Concerning Drangajökull, there are no artificial dams surrounding the ice cap. The glacier's mass dropped ($-219,592\text{t}$) between April 2002 and December 2021. Even if the area of Folgefonna decreased from 2002 to 2021, the mass balance could be close to zero due to rising temperatures and precipitations acting as a counterbalance. This period characterized by low mass and volume variation is likely an inversion phase announcing a prolonged decrease in the following century caused by anthropic emissions. The three ice caps of Folgefonna will continually decrease, despite the uncertainty of true temperature evolution and high precipitations (section 5.4.2).

Chapter 7

Conclusion

This research analyzes the evolution of Folgefonna through remote sensing methods in a climate change context, improves the current tools of DEM comparison, observes the correlation of the glacier's physical features with climatic data, and explores the evolution of the three-ice caps of Folgefonna.

The four research questions set out in section 1.3 are answered as follows.

7.1 How have Folgefonna's features evolved during the last century using remote sensing methods?

The examination of the results obtained by the OGGM script (Figure 5.24) and comparisons of DEMs from 1937 to 2021 show an increasing and two decreasing phases in glacier volume. From 1937 to 1967, the glacier shows a reduction of 1.2km^3 . Then, from 1967 to 1994, it advanced by 1.5km^3 . Finally, from 1994 to 2021, it decreased again by at least 0.9km^3 . It should be noted that these computations contain a high degree of uncertainty. The evolution of the DEM from 1959 to 2017 (Figure 5.26) is presumably the most accurate due to superior data. During this period, the glacier decreased by $3.03 \pm 0.06\text{km}^3$ ($-2.6 \pm 0.6\text{Gt}$). As for the glacier area, the most precise period is from 1994 to 2017, where the three ice caps display a decrease of $-53.74 \pm 25\text{km}^2$ (-22.92%) in surface area. During the same period²¹, the ELA increased by 88.5m.

7.2 How can DEMs processing be improved?

The developed software was the most substantial work to improve photogrammetry. The first version operates satisfactorily. It allows to expressly reduce the processing time of distinct DEMs by proposing a simple user interface to calculate the evolution of the glacier's features, such as the volume change, mass change, meter water equivalent, and effect on sea-level rise. The software allows the execution of the following steps: co-registrations, subtractions, interpolations and errors calculation. Moreover, it automatically generates a report for all calculations for analysis and comparison of produced results.

²¹ The same period for which the evolution is also the most accurate.

This is the first version, and naturally, various elements can be improved. Furthermore, some necessary entries which can automatically be calculated, such as the vector frame to homogenize entries, will be removed.

7.3 Is there a strong correlation between the evolution of Folgefonna and the climatic data?

The latest phase of rising temperatures recorded by the Bergen–Florida station started in the mid–1980. The temperature rose by 1.33°C until 2021, and the precipitations increased by 331mm. The ELA results reveal that the increase in precipitations counterbalanced the rise in temperatures until the end of the 1990s.

The moving average of the glacier area over four years and the summer temperatures present the highest correlation of $r = -0.78$. Between the moving average of the ELA and the temperature, the correlation is the second–highest, at $r = 0.67$.

Overall, the correlation between the ELA and climatic data is not strong enough to conclude whether or not there is a strong interdependence between the evolution of the glacier and the climatic data. Nevertheless, the most significant feature evolution, the correlation between the mass evolution of Folgefonna and climatic data, could not be calculated due to a lack of data.

7.4 How will Folgefonna evolve facing different climatic scenarios?

All climatic scenarios are based on an increase in carbon dioxide and methane emissions from human activities, which induce a rise in global temperatures and precipitations for Folgefonna. In the scenario with the lowest emissions (RCP 26), Folgefonna will lose a volume of 6.5km³ (–21.6%) by 2100. For the highest emission scenario (RCP 85), Folgefonna will decrease by 11.1km³ (–37%). Nevertheless, computing the uncertainty in climatic prevision and glacier model evolution would allow for more precise results.

References

- Agüera–Vega F. A., Carvajal–Ramírez, & Martínez–Carricondo, 2017: Assessment of photogrammetric mapping accuracy based on variation ground control points number using unmanned aerial vehicle. *ScienceDirect*. doi: 10.3390/rs12142221 <https://www.sciencedirect.com/science/article/pii/S026322411630700X?via%3Dihub>
- Albert T.H., 2002: Evaluation of Remote Sensing Techniques for Ice–Area Classification Applied to the Tropical Quelccaya Ice Cap, Peru, *Polar Geography*, 26:3, 210–226, doi: 10.1080/789610193 <https://doi.org/10.1080/789610193>
- Andreassen L. M., Elvehøy H., Kjøllmoen B., Engeset R., & Haakensen N., 2005: Glacier mass–balance and length variation in Norway. *Annals of Glaciology*, 42, 317–325. doi: 10.3189/172756405781812826 <https://doi.org/10.3189/172756405781812826>
- Benn D., Evans D. J. A. (2010). *Glaciers and Glaciation*, 2nd edition (2nd ed.). Routledge. 3–56, doi :10.4324/9780203785010
- Berthier E., Arnaud Y., Vincent C., Remy F., 2006: Biases of SRTM in high–mountain areas: Implications for the monitoring of glacier volume changes. *Geophysical Research Letters*, American Geophysical Union, 2006, 33 (L08502), 1 to 5 p. doi: 10.1029/2006GL025862
- Blazquez A., Meyssignac B., Lemoine J., Berthier E., Ribes A., & Cazenave A. 2018: Exploring the uncertainty in GRACE estimates of the mass redistributions at the Earth surface: implications for the global water and sea level budgets. *Geophysical Journal International*, 215(1), 415–430. doi: 10.1093/gji/ggy293
- Bogen, J., Wold B. And Ostrem G., 1989: Historic glacier variations in Scandinavia. In: Oerlemans, J(ed.): *Glacier Fluctuations and Climatic Change*. Reidel. Dordrecht: 109–128.
- Bolibar J., Rabatel A., Gouttevin, Galiez C., Condom T., & Sauquet E., 2020: Deep learning applied to glacier evolution modelling. *The Cryosphere*, 14(2), 565–584. <https://doi.org/10.5194/tc-14-565-2020>
- Church J.A. and 13 others, 2013: Sea Level Change. In Stocker, TF and 9 others eds. *Climate change 2013: the physical science basis. Contribution of working group I to the fifth assessment report of the intergovernmental panel on climate change*. Cambridge University Press, Cambridge, UK and New York, NY, USA. doi: 10.1017/CBO9781107415324
- Dozier J., 1989: Spectral signature of alpine snow cover from Landsat 5 TM. *Remote Sensing of Environment*, 28, 9–22.
- Farinotti D., Huss M., Fürst J. J., Landmann J., Machguth H., Maussion F., Pandit A., 2019: A consensus estimate for the ice thickness distribution of all glaciers on Earth. *Nature Geoscience*. Retrieved. doi: 10.1038/s41561-019-0300-3 <https://doi.org/10.1038/s41561-019-0300-3>
- Ferreira G., Montecino H. D. C., Yakubu C., Heck B., 2016: Uncertainties of the Gravity Recovery and Climate Experiment time–variable gravity–field solutions based on three–cornered hat method. *Journal of Applied Remote Sensing*, 10(1), 015015. doi: 10.1117/1.jrs.10.015015 <https://doi.org/10.1117/1.jrs.10.015015>

- Fraser C.S., Cronk S., 2009: A hybrid measurement approach for close-range photogrammetry. *ISPRS Journal of Photogrammetry and Remote Sensing*, 64, 328–333.
- Fricker H. A., Borsa A., Minster B., Carabajal C., Quinn K., and Bills B., 2005: Assessment of ICESat performance at the Salar de Uyuni, Bolivia, *Geophys. Res. Lett.*, 32(5), L21S06, doi: 10.1029/2005GL023423,
- Graabak, Jaehnert S., Korpås M., Mo B., 2017: Norway as a Battery for the Future European Power System—Impacts on the Hydropower System. *Energies*, 10(12), 2054. doi: 10.3390/en10122054 <https://doi.org/10.3390/en10122054>
- Haeberli W. 1995: Glacier fluctuations and climate change detection, *Geogr. Fis. Dinam. Quat.*, 18, 191–199. http://www.glaciologia.it/wp-content/uploads/FullText/full_text_18_2/7_GFDQ_18_2_Haeberli_191_199.pdf
- Hock R., Bliss A., Marzeion B., Giesen R. H., Hirabayashi Y., Huss M., Radić and Slangen A. B. A.: GlacierMIP, 2019: A model intercomparison of global-scale glacier mass-balance models and projections, *J. Glaciol.*, 65(251), 453–467, doi:10.1017/jog.2019.22,
- Huss M., 2013: Density assumptions for converting geodetic glacier volume change to mass change. *The Cryosphere*, 7(3), 877–887. doi: 10.5194/tc-7-877-2013 <https://doi.org/10.5194/tc-7-877-2013>
- Imhof P., Nesje A., Nusbaumer S. U., 2011: Climate and glacier fluctuations at Jostedalsbreen and Folgefonna, southwestern Norway and in the western Alps from the ‘Little Ice Age’ until the present: The influence of the North Atlantic Oscillation. *The Holocene*. doi: 10.1177/0959683611414935
- Johansson F. E., Bakke J., Støren E., Gillespie M., 2019: Subglacial Landscape of Folgefonna (Norway) Indicate Significant Hydrological Changes in a Future Ice-free Environment. *NASA/ADS*. <https://ui.adsabs.harvard.edu/abs/2019AGUFM.C41D1488J/abstract>
- Kienholz C., Rich J. L., Arendt A. A., and Hock R., 2014: A new method for deriving glacier centrelines applied to glaciers in Alaska and northwest Canada, *The Cryosphere*, 8, 503–519, doi: 10.5194/tc-8-503-2014 <https://doi.org/10.5194/tc-8-503-2014>
- Lambeck K., Rouby H., Purcell A., Sun Y. and Sambridge M., 2014: Sea level and global ice volumes from the Last Glacial Maximum to the Holocene. *PNAS*. doi: 10.1073/pnas.1411762111 <https://www.pnas.org/content/111/43/15296>
- Lysaker, D. and Vestøl O., 2020: The Norwegian vertical reference frame NN2000. Technical report of the Norwegian Mapping Authority 19–04811–4, ISBN: 978–82–7945–247–8. <https://www.kartverket.no/globalassets/til-lands/posisjon/the-norwegian-vertical-reference-frame-nn2000.pdf>
- Mannerfelt, E., Hugonnet R., Dehecq A. and others, 2021: Xdem python script <https://xdem.readthedocs.io/en/latest/>
- Marzeion B., Jarosch A. H. and Hofer M., 2012: Past and future sea-level change from the surface mass balance of glaciers. *The Cryosphere* 6, 1295–1322. doi:10.5194/tc-6-1295-2012
- Marzeion B., Hock R., Anderson B., Bliss A., Champollion N., Fujita K., Huss M., Immerzeel W. W., Kraaijenbrink P., Malles J., Maussion F., Radić, Rounce D. R., Sakai A., Shannon S., Wal R., Zekollari H., 2020: Partitioning the Uncertainty of Ensemble Projections of Global Glacier Mass Change. *Earth’s Future*, 8(7). doi: 10.1029/2019ef001470, <https://doi.org/10.1029/2019ef001470>

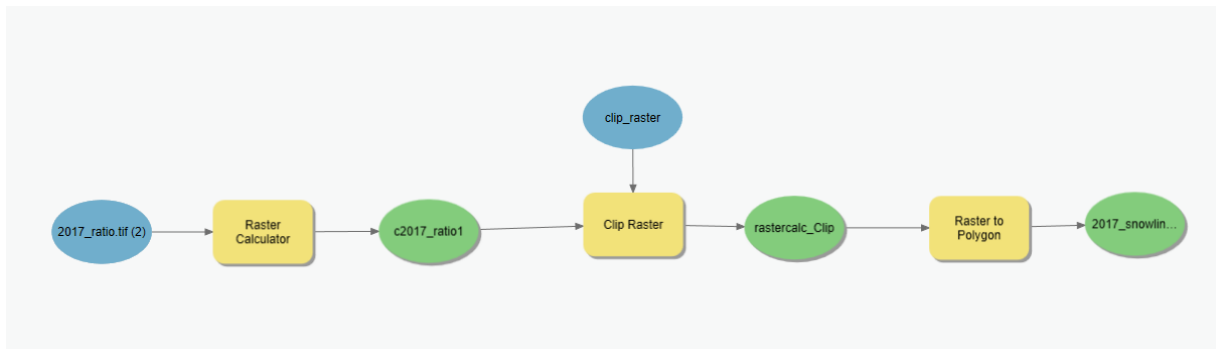
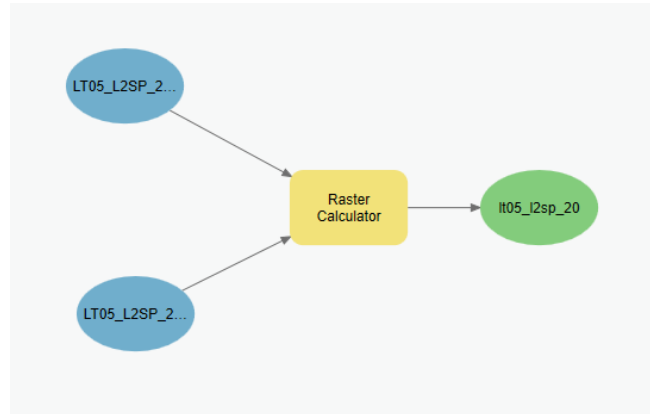
- Matthews N.A., 2008: Aerial and close-range photogrammetric technology: providing resource documentation, interpretation, and preservation. Technical Note, 428. Bureau of Land Management, Denver, Colorado.
- Maussion F., Butenko A., Champollion N., Dusch M., Eis J., Fourteau K., Gregor P., Jarosch A. H., Landmann J., Oesterle F., Recinos B., Rothenpieler T., Vlug A., Wild C. T. & Marzeion B., 2019: The open Global Glacier model (OGGM) v1.1 Geosci. Model De5. (GMD), 12 (3), pp. 909–931, doi: 10.5194/gmd-12-909-2019
- Metashape User Manual (Agisoft), 2021: Professional Edition, Version 1.7, https://www.agisoft.com/pdf/metashape-pro_1_7_en.pdf
- Mölg, N., Bolch, T., 2017: Structure-from-Motion Using Historical Aerial Images to Analyse Changes in Glacier Surface Elevation. *Remote Sensing*, 9(10), 1021. doi: 10.3390/rs9101021, <https://doi.org/10.3390/rs9101021>
- Morlighem M., Williams C. N., Rignot E., An L., Arndt J. E., Bamber J. L., Zinglensen K. B., 2017: BedMachine v3: Complete Bed Topography and Ocean Bathymetry Mapping of Greenland From Multibeam Echo Sounding Combined With Mass Conservation. *Geophysical Research Letters*, 44(21), 11,11–51,61. doi: 10.1002/2017GL074954 <https://doi.org/10.1002/2017GL074954>
- Morlighem M., Rignot E., Binder T., Blankenship D., Drews R., Eagles G., Young D. A., 2019: Deep glacial troughs and stabilizing ridges unveiled beneath the margins of the Antarctic ice sheet. *Nature Geoscience*. doi: 10.1038/s41561-019-0510-8 <https://doi.org/10.1038/s41561-019-0510-8>
- Muskett R. R., 2012: Remote Sensing, Model-Derived and Ground Measurements of Snow Water Equivalent and Snow Density in Alaska. *International Journal of Geosciences*, 03(05), 1127–1136. doi: 10.4236/ijg.2012.35114 <https://doi.org/10.4236/ijg.2012.35114>
- Neale W. T.C., Hessel D., Terpstra T., 2011 : Photogrammetric Measurement Error Associated with Lens Distortion, http://www.close-range.com/docs/Photogrammetric-Measurement-error-from-lens-distortion_2011-01-0286.pdf
- Nesje A., Lie Ø. and Dahl S. O., 2000: Is the North Atlantic Oscillation reflected in Scandinavian glacier mass balance records? *J. Quaternary Sci.*, Vol. 15, pp. 587–601. ISSN: 0267-8179. <https://onlinelibrary.wiley.com/doi/epdf/10.1002/1099-1417%28200009%2915%3A6%3C587%3A%3AAID-JQS533%3E3.0.CO%3B2-2>
- Nussbaumer S. U., Nesje A., Zumbühl H. J., 2011: Historical glacier fluctuations of Jostedalbreen and Folgefonna (southern Norway) reassessed by new pictorial and written evidence. *The Holocene*, 21(3), 455–471. doi: 10.1177/0959683610385728 <https://doi.org/10.1177/0959683610385728>
- Nuth C., Kääb A., 2011: Co-registration and bias corrections of satellite elevation data sets for quantifying glacier thickness change. *The Cryosphere*, 5(1), 271–290. doi: 10.5194/tc-5-271-2011 <https://doi.org/10.5194/tc-5-271-2011>
- Oerlemans J., & Reichert B. K., 2000: Relating glacier mass balance to meteorological data by using a seasonal sensitivity characteristic | *Journal of Glaciology*. Cambridge Core. doi: 10.3189/172756500781833269 <https://www.cambridge.org/core/journals/journal-of-glaciology/article/relating-glacier-mass-balance-to-meteorological-data-by-using-a-seasonal-sensitivity-characteristic/BADC55CE8CD235345DF5554B5C2F5024>
- Østrem, G. 1975: ERTS data in glaciology—an effort to monitor glacier mass balance from satellite imagery. *Journal of Glaciology*, 15, 403–415.

- Paul F., Bolch T., Kääb A., Nagler T., Nuth C., Scharrer K., Shepherd A., Strozzi T., Ticconi F., Bhambri R., Berthier E., Bevan S., Gourmelen N., Heid T., Jeong S., Kunz, M. Lauknes T. R., Luckman A., Merryman Boncori J. P., van Niel T., 2015: The glaciers climate change initiative: Methods for creating glacier area, elevation change and velocity products. *Remote Sensing of Environment*, 162, 408–426. doi: 10.1016/j.rse.2013.07.043, <https://doi.org/10.1016/j.rse.2013.07.043>
- Paul F., Kääb A., Maisch M., Kellenberger, T., Haeberli W., 2002: The new remote-sensing-derived Swiss glacier inventory: I. Methods. *Annals of Glaciology*, 34, 355–361. <https://doi.org/10.3189/172756402781817941>
- Paul F., Kääb A., 2005: Perspectives on the production of a glacier inventory from multispectral satellite data in Arctic Canada: Cumberland Peninsula, Baffin Island. *Annals of Glaciology*, 42, 59–66. doi: 10.3189/172756405781813087 <https://doi.org/10.3189/172756405781813087>
- Porter, Claire; Morin, Paul; Howat, Ian; Noh, Myoung-Jon; Bates, Brian; Peterman, Kenneth; Keeseey, Scott; Schlenk, Matthew; Gardiner, Judith; Tomko, Karen; Willis, Michael; Kelleher, Cole; Cloutier, Michael; Husby, Eric; Foga, Steven; Nakamura, Hitomi; Platson, Melisa; Wethington, Michael, Jr.; Williamson, Cathleen; Bauer, Gregory; Enos, Jeremy; Arnold, Galen; Kramer, William; Becker, Peter; Doshi, Abhijit; D’Souza, Cristelle; Cummins, Pat; Laurier, Fabien; Bojesen, Mikkel, 2018, “ArcticDEM”, <https://doi.org/10.7910/DVN/OHHUKH>, Harvard Dataverse, V1, [12/05/2022]
- Rabatel A., Dedieu J. P., Thibert E., Letreguilly A., Vincent C. 2008: 25 years (1981–2005) of equilibrium-line altitude and mass-balance reconstruction on Glacier Blanc, French Alps, using remote-sensing methods and meteorological data. *Journal of Glaciology*, 54, 307–314. doi: 10.1017/jog.2016.113
- Racoviteanu A. E, Paul F., Raup B., Khalsa S. J. S. & Armstrong R. 2009: Challenges in glacier mapping from space: recommendations from the Global Land Ice Measurements from Space (GLIMS) initiative. *Annals of Glaciology*, 50(53), 53–69. doi: 10.3189/2013AoG63A296 <https://www.cambridge.org/core/journals/annals-of-glaciology/article/on-the-accuracy-of-glacier-outlines-derived-from-remotesensing-data/D9EF9B9A26CEF34970C4F4924C19CE93>
- Ramilien F. S., 2016: *Space Gravimetry Using GRACE Satellite Mission: Basic Concepts*. ScienceDirect. doi: 10.1002/2016GL070265 <https://www.sciencedirect.com/science/article/pii/B9781785481598500062>
- Remondino F., El-Hakim S., 2006: Image-based 3-D modelling: a review. *The Photogrammetric Record* 21, 269–291. doi: 10.1111/j.1477-9730.2006.00383.x https://onlinelibrary.wiley.com/doi/full/10.1111/j.1477-9730.2006.00383.x?casa_token=Is646845XAYAAAAA%3Aqbiip862X3ZgGoLGyenX0MUDXA-1KCBspSMTiGO5J74w7CDncDHY_FBSwpyMGmHaHKBfG-jdqZiGyrWVm
- RGI Consortium, 2017. Randolph Glacier Inventory – A Dataset of Global Glacier Outlines, Version 6. [Indicate subset used]. Boulder, Colorado USA. NSIDC: National Snow and Ice Data Center. doi: <https://doi.org/10.7265/4m1f-gd79>
- Richardson S. D., & Reynolds J. M., 2000: An overview of glacial hazards in the Himalayas. *Quaternary International*, 65–66, 31–47. doi: 10.1016/s1040-6182(99)00035-x [https://doi.org/10.1016/s1040-6182\(99\)00035-x](https://doi.org/10.1016/s1040-6182(99)00035-x)
- Rolstad C., Haug T., Denby B., 2009: Spatially integrated geodetic glacier mass balance and its uncertainty based on geostatistical analysis: application to the western Svartisen ice cap, Norway. *Journal of Glaciology*, 55(192), 666–680.

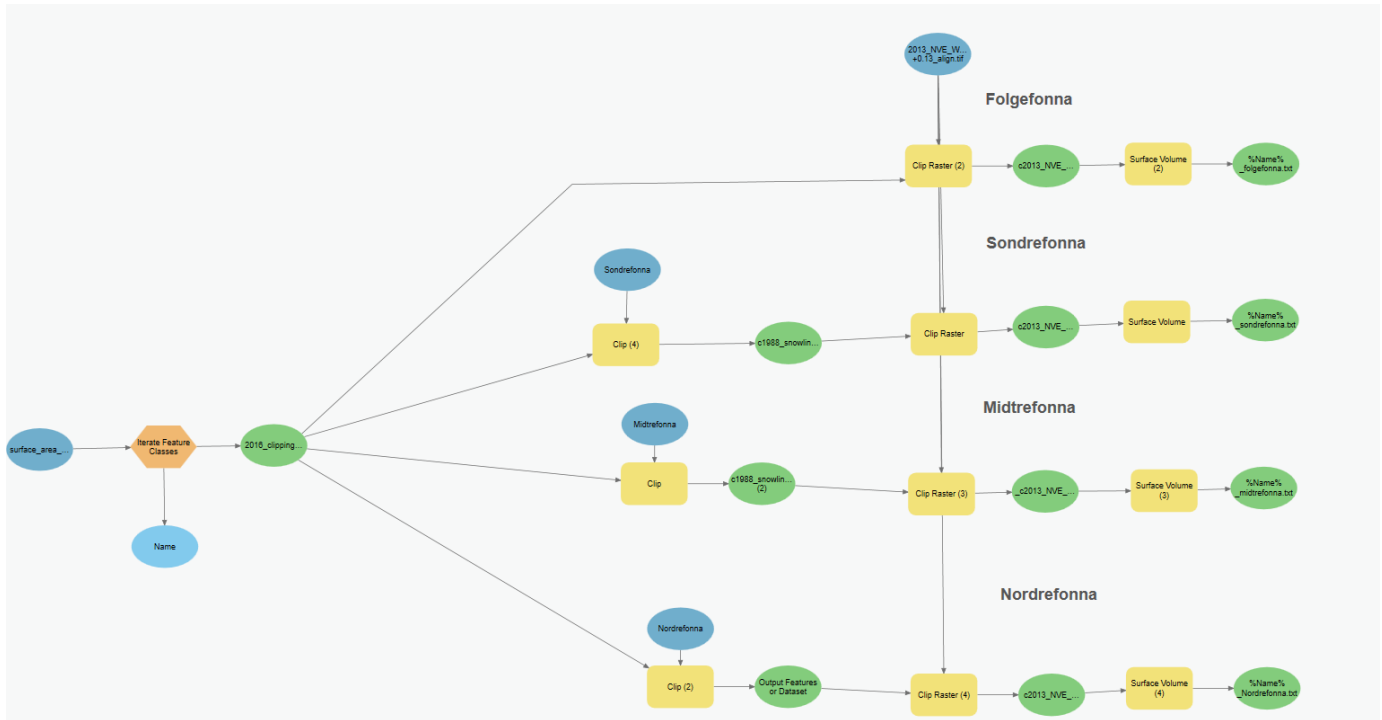
- doi: 10.3189/002214309789470950
<https://doi.org/10.3189/002214309789470950>
- Rosnell T., Honkavaara E., & Nurminen K., 2012: On geometric processing of multi-temporal image data collected by light UAV systems. *The International Archives of the Photogrammetry, Remote Sensing and Spatial Information Sciences*, XXXVIII-1/C22, 63–68. <https://doi.org/10.5194/isprsarchives-xxxviii-1-c22-63-2011>
- Rounce D. R. 2019: Python Glacier Evolution Model ‘PyGEM’ Manual, Github repository. <https://github.com/drounce/PyGEM>
- Rounce D. R., Khurana T., Short M. B., Hock R., Shean D. E., & Brinkerhoff D. J., 2020: Quantifying parameter uncertainty in a large-scale glacier evolution model using Bayesian inference: application to High Mountain Asia. *Journal of Glaciology*, 66(256), 175–187. doi: 10.1017/jog.2019.91
<https://doi.org/10.1017/jog.2019.91>
- Statkraft, 2020: Hydroelectricity in Norway – website: <https://www.statkraft.com/what-we-do/hydropower/>
- Sun T., Grimmond S., 2019: A Python-enhanced urban land surface model SuPy (SUEWS in Python, v2019.2): development, deployment and demonstration. *Geoscientific Model Development*, 12(7), 2781–2795. doi: 10.5194/gmd-12-2781-2019
<https://doi.org/10.5194/gmd-12-2781-2019>
- Thompson, L. G. (2010). Climate change: The evidence and our options. *The Behavior Analyst*, 33(2), 153–170. doi: 10.1007/bf03392211
<https://doi.org/10.1007/bf03392211>
- Tierney J.E., Zhu J., King J., Malevich S. B., Hakim G. J., Poulsen C. J., 2020: Glacial cooling and climate sensitivity revisited. *Nature* 584, 569–573. doi: 10.1038/s41586-020-2617-x
<https://doi.org/10.1038/s41586-020-2617-x>
- Vuille M., Carey M., Huggel C., Buytaert W., Rabatel A., Jacobsen D., Soruco A., Villacis M., Yarleque C., Elison Timm O., Condom T., Salzmann N. and Sicart J.-E. 2018: Rapid decline of snow and ice in the tropical Andes – Impacts, uncertainties and challenges ahead, *Earth-Sc1. Re5.*, 176, 195–213. doi: 10.1016/j.earscire5.2017.09.019
- Westoby J. Brasington N.F. Glasser M.J. Hambrey J.M. Reynolds 2012: ‘Structure-from-Motion’ photogrammetry: A low-cost, effective tool for geoscience applications, *Geomorphology*, Volume 179, Pages 300–314. doi: 10.1016/j.geomorph.2012.08.021
<https://doi.org/10.1016/j.geomorph.2012.08.021>
- Winsvold S. H., Andreassen L. M., Kienholz C., 2014: Glacier area and length changes in Norway from repeat inventories. *The Cryosphere*, 8(5), 1885–1903. doi: 10.5194/tc-8-1885-2014
<https://doi.org/10.5194/tc-8-1885-2014>
- Wouters B. and 5 others, 2014: GRACE, time-varying gravity, earth system dynamics and climate change. *Rep. Prog. Phys.*, 77, 116801. doi: 10.1088/0034-4885/77/11/116801
- Youssef B. B., Bizzocchi J., Bowes J., 2005: The future of video. *Proceedings of the 2005 ACM SIGCHI International Conference on Advances in Computer Entertainment Technology – ACE ’05.* doi: 10.1145/1178477.1178508
<https://doi.org/10.1145/1178477.1178508>
- Zhang M., Wang X., Shi C., Yan D. 2019: Automated Glacier Extraction Index by Optimization of Red/SWIR and NIR /SWIR Ratio Index for Glacier Mapping Using Landsat Imagery. *Water*, 11(6), 1223. doi: 10.3390/w11061223
<https://doi.org/10.3390/w11061223>

A.

Appendix



Appendix A.1: Model builder for drawing Glacier area and snow Glacier area during the autumn. Model builder A calculates the AGEI ratio, while Model builder B allows calculating polygon surface from AGEI ratio raster.



Appendix A.2: Model builder for Glacier area calculation

```

import numpy as np
import matplotlib.pyplot as plt
from scipy.optimize import curve_fit
def distortion_model(r, df, k1, k2, k3):
    r2 = r * r
    r4 = r2 * r2
    r6 = r4 * r2
    a = r * df + r * (k1 * r2 + k2 * r4 + k3 * r6)

    return a
# f = 114.61
# x = np.array([20.0, 40.0, 60.0, 70.0, 80.0, 90.0, 100.0, 110.0])
# y = np.array([+0.004, +0.005, +0.001, -0.003, -0.007, -0.007, -0.004, +0.006])

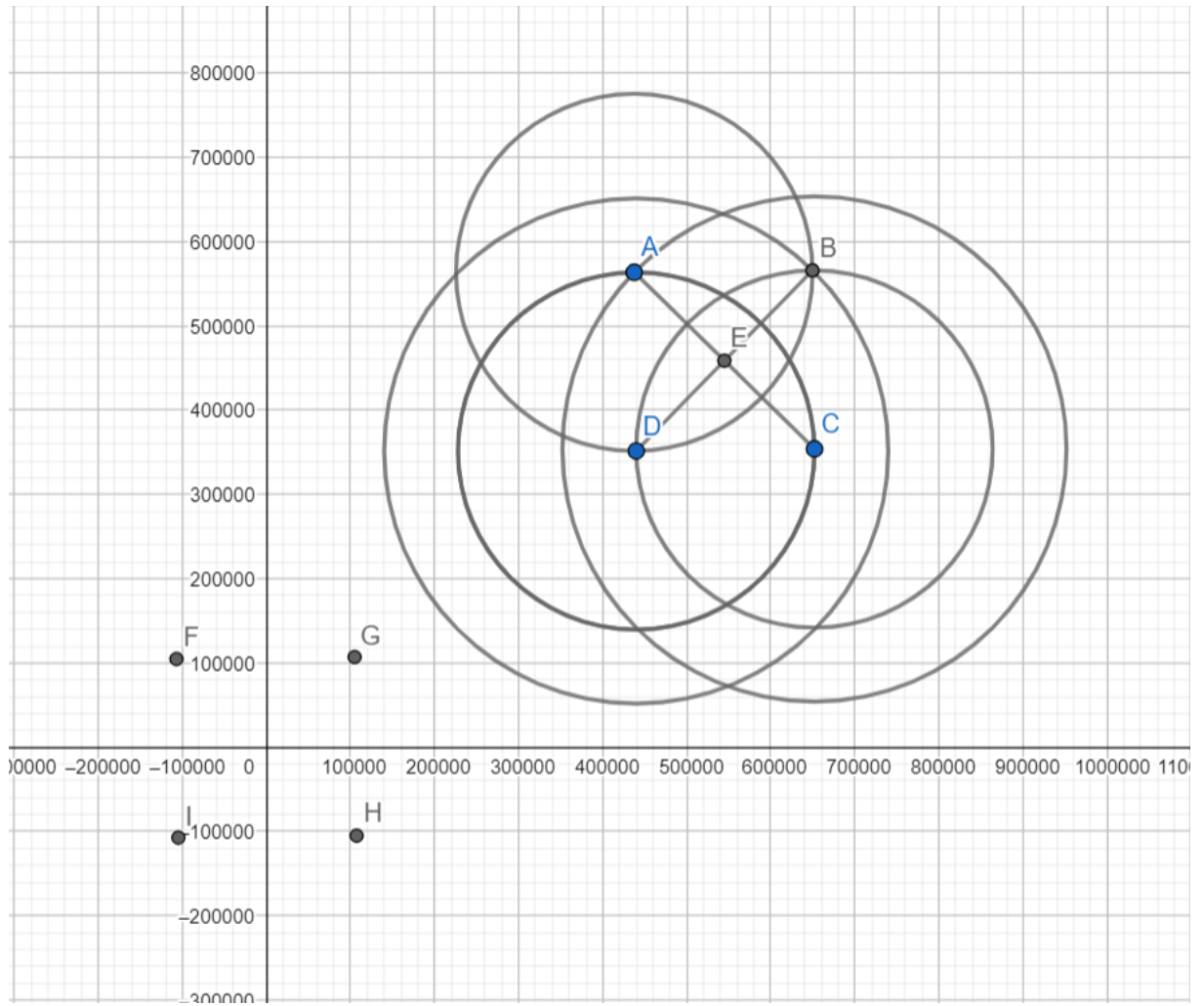
f = 152.99
x = np.array([10.0, 20.0, 30.0, 40.0, 50.0, 60.0, 70.0, 80.0, 90.0, 100.0, 110.0, 120.0, 130.0,
140.0, 148.0])
y = np.array([-1.8e-3, -3.5e-3, -4.7e-3, -5.0e-3, -4.4e-3, -3.4e-3, -1.7e-3, 0.6e-3, 3.0e-3, 4.2e-
3, 3.8e-3, 2.7e-3, 1.8e-3, 0.4e-3, 0.8e-3])
calibration, _ = curve_fit(distortion_model, x, y)
df, k1, k2, k3 = calibration
f += df * f
k1 *= f ** 3
k2 *= f ** 5
k3 *= f ** 7

print("""
<?xml version="1.0" encoding="UTF-8"?>
<calibration>
  <projection>frame</projection>
  <f>{: .3f}</f>
  <k1>{: .3}</k1>
  <k2>{: .3}</k2>
  <k3>{: .3}</k3>
</calibration>
""".format(f, k1, k2, k3))

xnew = np.linspace(x[0], x[-1], 1000)
plt.plot(x, y, 'bo')
plt.plot(xnew, distortion_model(xnew, *calibration), 'r-')
plt.show()

```

Appendix A.3: Wallis script used to increase the contrast of the images



Appendix A.4: Conversion of the calibration reports distances into coordinates by using Geometry GeoGebra software


```

files = dir('W:\Folgefonna_project\DATA\Aerial_images\1962\original\') ;
N = length(files) ;
for i = 3:N
adress= strcat('W:\Folgefonna_project\DATA\Aerial_images\1962\original\',files(i).name);
grayImage = imread(adress);
outputImage2 = WallisFilter(grayImage, 127, 50, 8, 0.3, 100, true);
outputImage = WallisFilter(outputImage2, 127, 50, 8, 0.3, 100, false);
fullFileName = fullfile('W:\Folgefonna_project\DATA\Aerial_images\1962\1962_wallis_v1\', files(i).name);
imwrite(outputImage,fullFileName);
end

function outputImage = WallisFilter(inputImage, desiredMean, desiredStdDev, Amax, percentage, windowWidth,
preSmooth)
outputImage = []; % Initialize
if mod(windowWidth, 2) == 0
% For example, if windowWidth = 4, make it 5 instead.
windowWidth = windowWidth+1;
end

dblImage = double(inputImage); % Cast to double from whatever it is on input.
if preSmooth
% gauss_blur = 1/273 * [1 4 7 4 1; 4 16 26 16 4; 7 26 41 26 7; 4 16 26 16 4; 1 4 7 4 1];
gauss_blur = fspecial('gaussian', windowWidth, 1);
dblImage = conv2(dblImage, gauss_blur, 'same');
end
uniformImage = ones(size(dblImage));
kernel = ones(windowWidth);
sumImage = conv2(dblImage, kernel, 'same');
countImage = conv2(uniformImage, kernel, 'same');

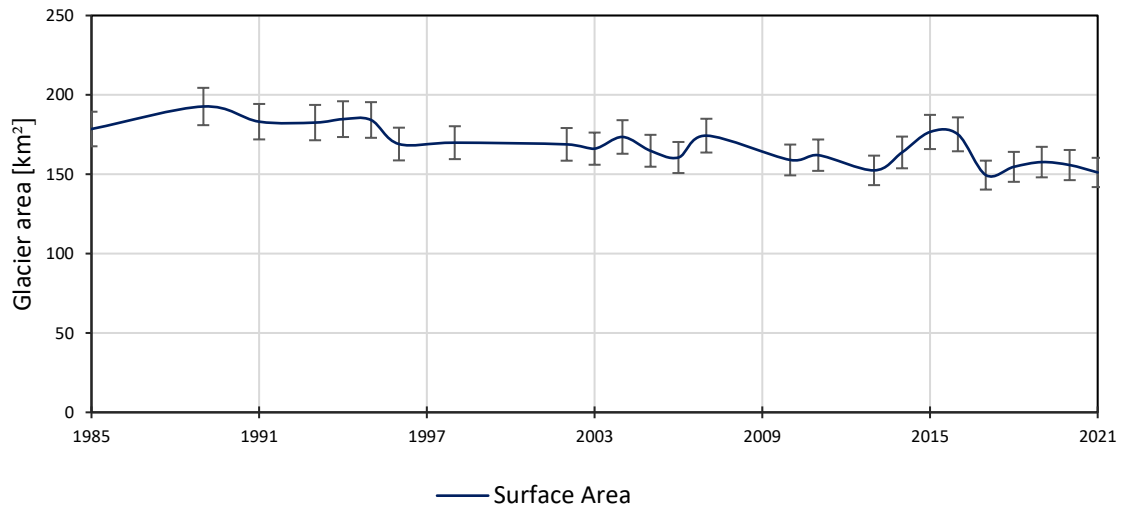
localMeanImage = sumImage ./ countImage;
D = conv2((dblImage - localMeanImage).^2, kernel, 'same') / (windowWidth^2);
D = sqrt(D);
G = (dblImage - localMeanImage) .* Amax .* desiredStdDev ./ (Amax .* D + desiredStdDev) + percentage * desiredMean
+ (1-percentage) * localMeanImage;
G(G < 0) = 0;
maxPossibleGrayLevel = intmax(class(inputImage));
outputImage = cast(G, 'like', inputImage);
end

```

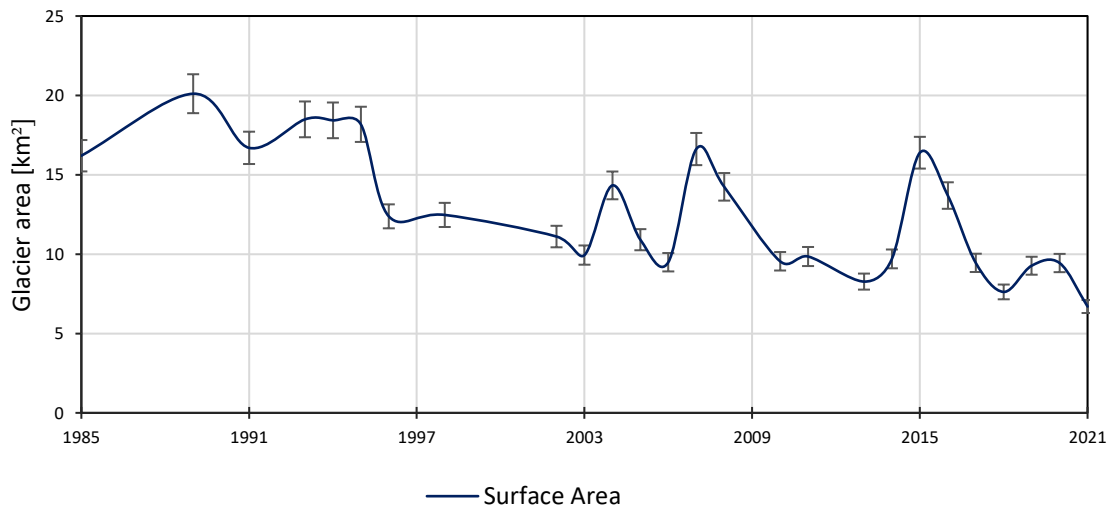
Appendix A.5:Wallis function used to increase the contrast of pictures locally

Type of solid water	Density
New snow (immediately after falling, calm conditions)	50–70 $kg\ m^{-3}$
Damp new snow	100–200 $kg\ m^{-3}$
Settled snow	200–300 $kg\ m^{-3}$
Wind-packed snow	350–400 $kg\ m^{-3}$
Firn	400–830 $kg\ m^{-3}$
Very wet snow and firn	700–800 $kg\ m^{-3}$
Glacier ice	830–923 $kg\ m^{-3}$

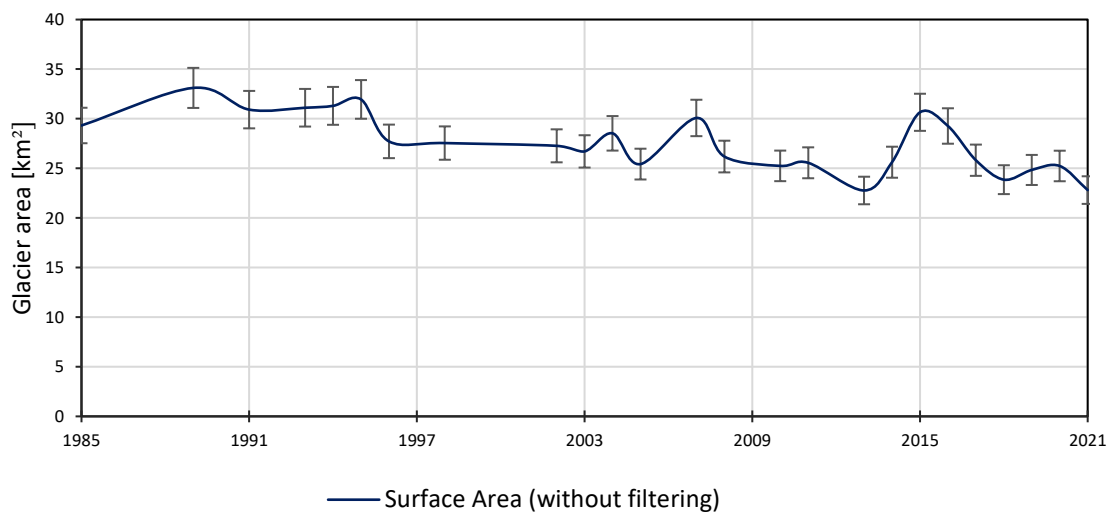
Appendix A.6: Ice density as a function of the type of solid water



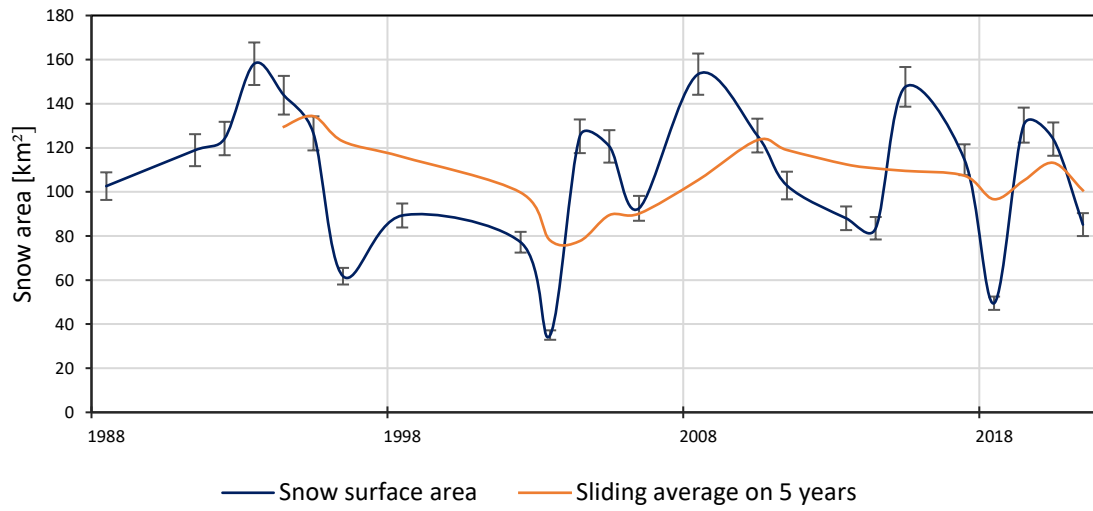
Appendix A.7: Evolution of the Søndre Folgefonna glacier area without filtering



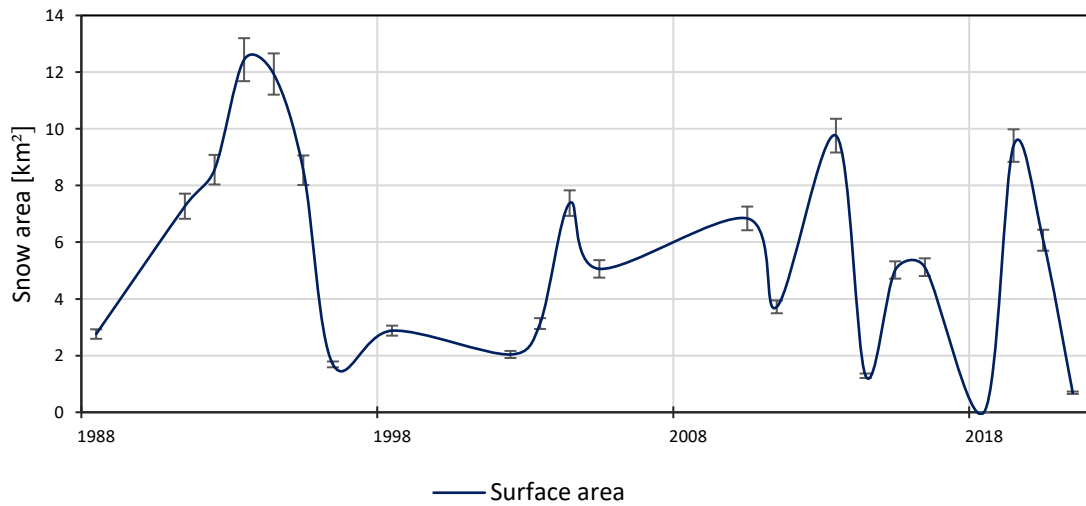
Appendix A.8: Evolution of the Søndre Folgefonna glacier area without filtering



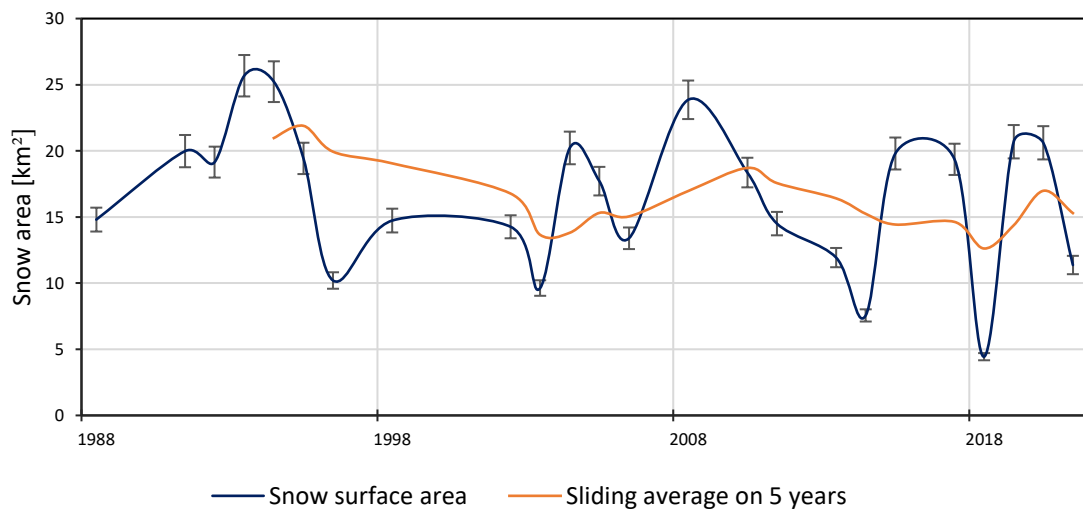
Appendix A.9: Evolution of the glacier area of the Nordre Folgefonna without filtering



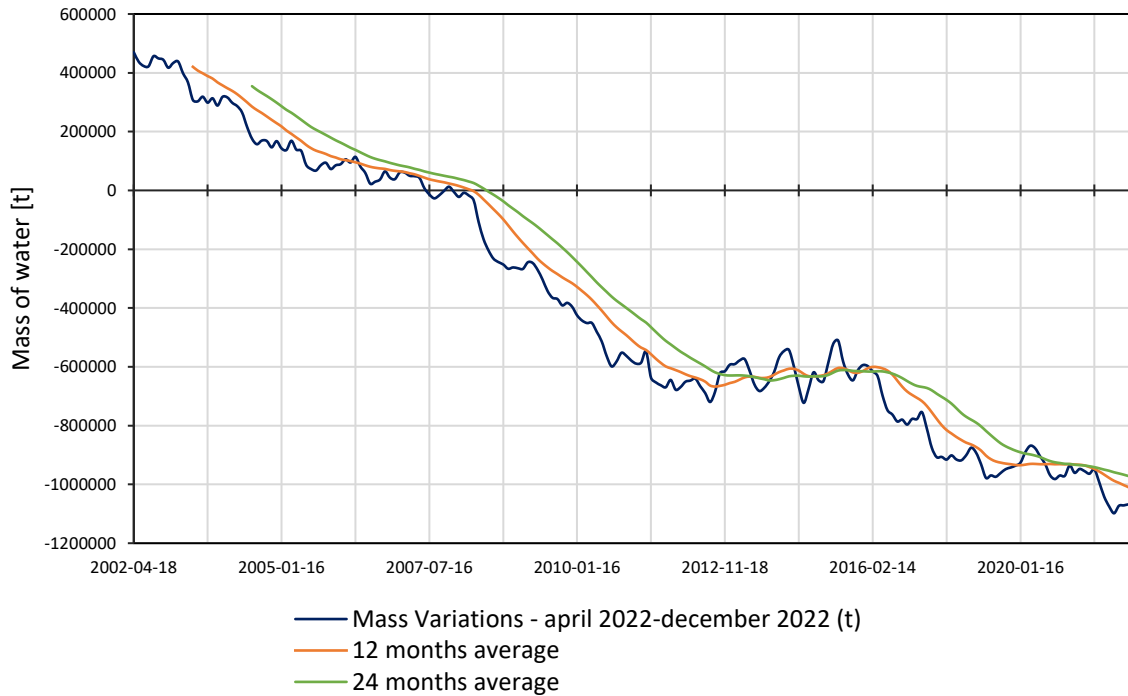
Appendix A.10: Evolution of the snow area for the Søndre Folgefonna from 1987 to 2022, at the end of the ablation season (August – September).



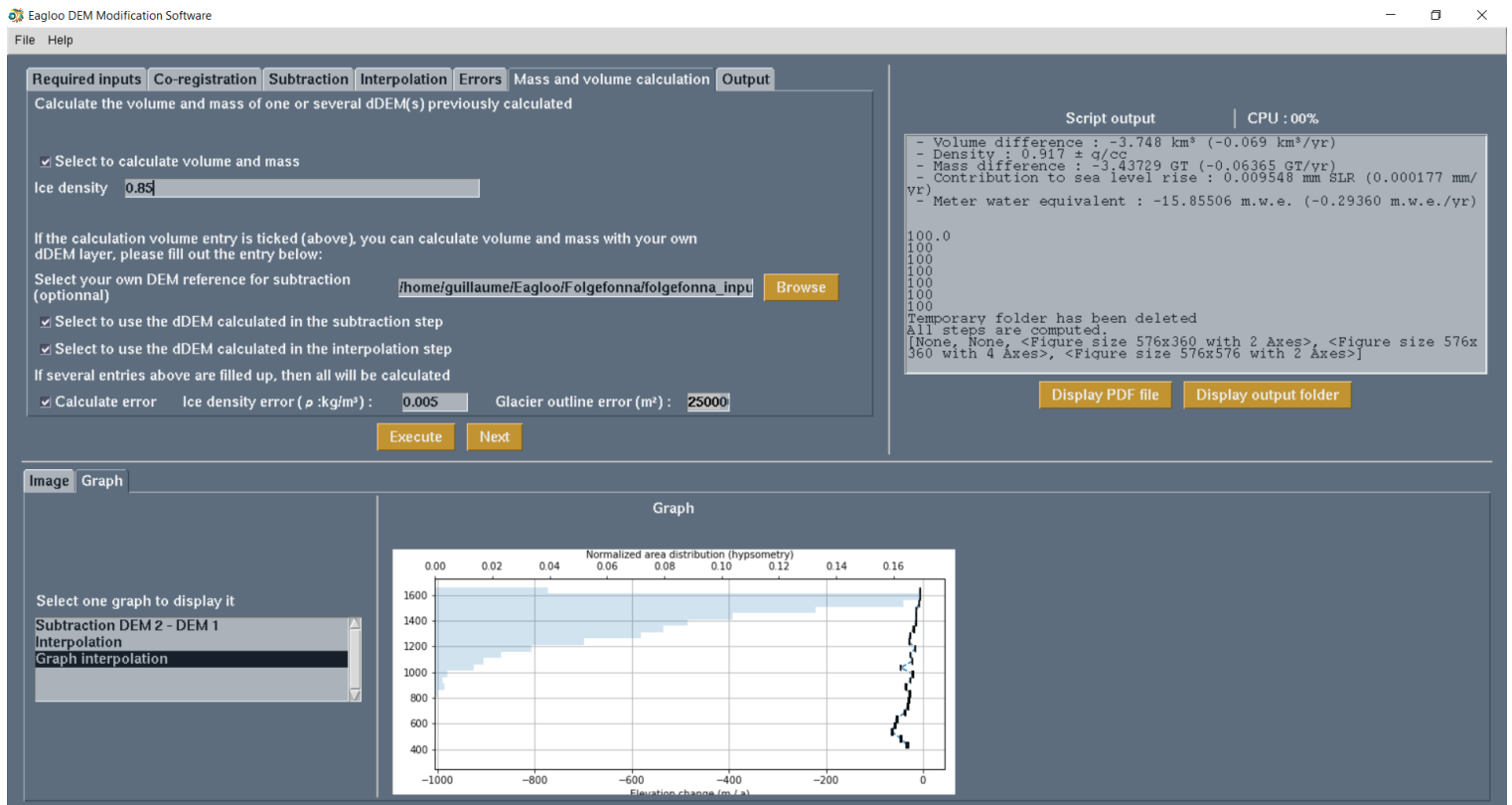
Appendix A.11: Evolution of the snow area for the Midtre Folgefonna from 1987 to 2022, at the end of the ablation season (August – September).



Appendix A.12: Evolution of the snow area from 1987 to 2022 at the end of the ablation season (August to September).



Appendix A.13: Water mass variation by gravimetry for the Drangajökull – carried out by the Center for Space Research (CSR) – from April 2002 to December 2021



Appendix A.14: Frontend of the software Eagloo, the main dialogue in on the upper left, where the user can fill out all necessary entries. On the upper right, there is a console. The graphs are displayed on the lower half at the end of an execution.

EAGLOO
DEM Modification Software

Report : Eagloo appendix

Processing report
Eagloo
Name : Eagloo appendix
28 May 2022

Methods of processing :
Subtraction
Interpolation - method : local hypsometric interpolation
Non-stationarity measurement errors
Volume and mass calculation



EAGLOO
DEM Modification Software

Page 1

EAGLOO
DEM Modification Software

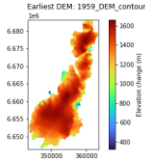
Report : Eagloo appendix

1 - Entry names

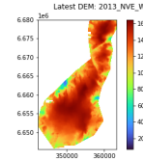
- Earliest DEM : 1959_DEM_contour
- Latest DEM : 2013_NVE_WGS
- Contour line shapefile of the biggest glacier (Use for masking) : Folgefonna1959_utm32
- Path where the files were saved : /home/guillaume/Eagloo/Folgefonna/temporary
- Coordinate system : EPSG:32633
- Shapefile frame of the study area : frame_folgefonna
- Resolution : 15.0 m

2 - Digital Elevation Model entries

Earliest DEM: 1959_DEM_contour



Latest DEM: 2013_NVE_WGS

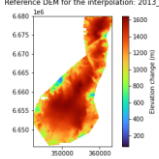


Page 2

EAGLOO
DEM Modification Software

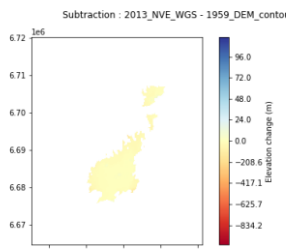
Report : Eagloo appendix

Reference DEM for the interpolation: 2013_NVE_WGS



3 - Subtraction : 1959_DEM_contour - 2013_NVE_WGS

Subtraction : 2013_NVE_WGS - 1959_DEM_contour



Page 3

EAGLOO
DEM Modification Software

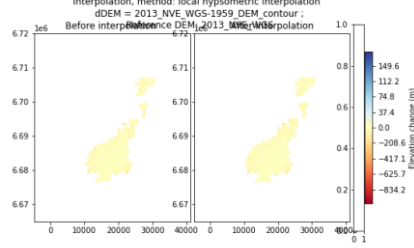
Report : Eagloo appendix

4 - Interpolation

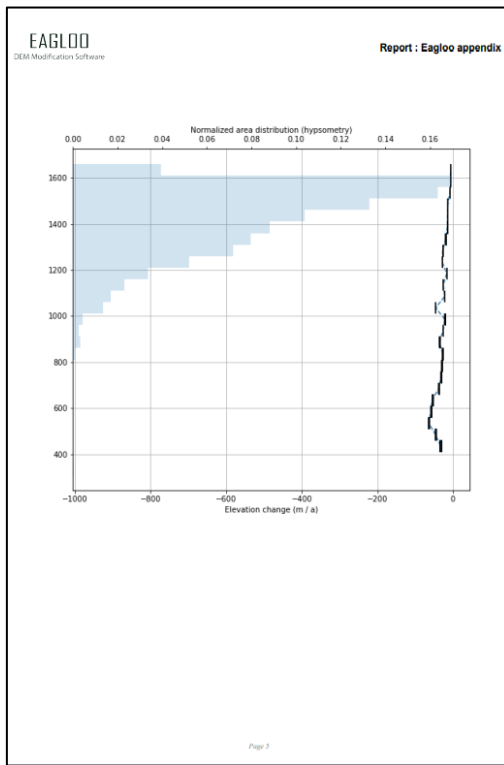
dDEM = 2013_NVE_WGS - 1959_DEM_contour

- Reference DEM for interpolation: 2013_NVE_WGS
- Method : local hypsometric interpolation

Interpolation, method: local hypsometric interpolation
dDEM = 2013_NVE_WGS - 1959_DEM_contour ;
Before interpolation: Reference DEM: 2013_NVE_WGS



Page 4



EAGLOO
DEM Modification Software

Report : Eagloo appendix

5 - Non-stationarity measurement errors

5.1 - Standardized integrated error and standardized mean error - based on the slope and the maximum absolute curvature

Standard deviation before scale-correction : **1.07**

Standard deviation after scale-correction : **1.00**

Surface area (glacier:Folgefonna1959_utm32) : **216977062.05 m²**

Average slope (glacier : Folgefonna1959_utm32): **8.53 °**

Number of effective samples (glacier :Folgefonna1959_utm32) : **9.29**

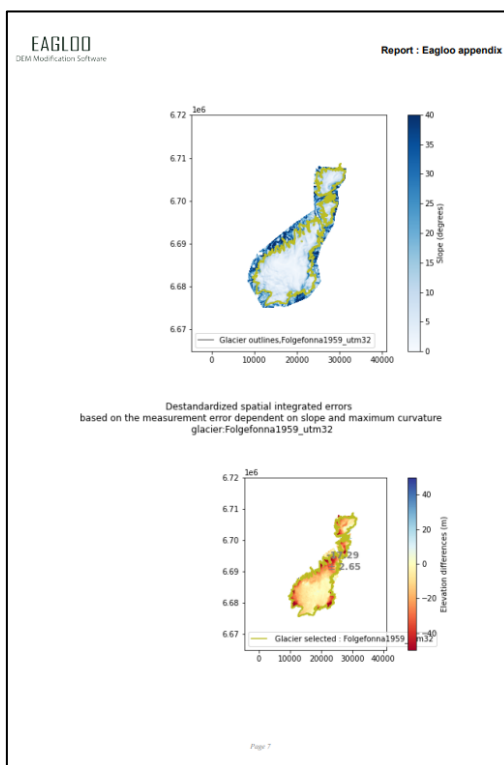
Standardized integrated error(glacier :Folgefonna1959_utm32) : **0.3282**

Average elevation difference and integrated error (destandardized)(glacier Folgefonna1959_utm32) : **-17.290 ± 2.653 m**

Uncertainty of the volume change (glacier :Folgefonna1959_utm32) : **575623114.67 m³**

Standardized mean error over the glacier : **7.55 m**

Page 6



EAGLOO
DEM Modification Software

Report : Eagloo appendix

6 - Volume and mass calculation

6.1 - Volume and mass calculation of the dDEM calculated in the subtraction step

dDEM : DDEM_subtraction_clipped_1959_DEM_contour_2013_NVE_WGS.tif

- Period : **1959-05-28 00:00:00 to 2013-05-28 00:00:00: 54.00 yr**

- Area : **216.79 ± 25.00 km²**

- Volume difference : **-3748407525 ± 575623115 m³ (-69413195 ± 10659417 m³/yr)**

- Volume difference : **-3.7484 ± 0.5756 km³ (-0.0694 ± 0.0107 km³/yr)**

- Density : **0.917 ± 0.005 g/cc**

- Mass difference : **-3.4373 ± 0.7201 GT (-0.0637 ± 0.0133 GT/yr)**

- Contribution to sea level rise : **0.009548 ± 0.002000 mm SLR (0.000177 ± 0.000037 mm/yr)**

- Meter water equivalent : **-15.8551 ± 3.0461 m.w.e. (-0.2936 ± 0.0564 m.w.e./yr)**

6.2 - Volume and mass calculation of the dDEM calculated in the interpolation step

dDEM : DDEM_subtraction_clipped_1959_DEM_contour_2013_NVE_WGS.tif

- Period : **1959-05-28 00:00:00 to 2013-05-28 00:00:00: 54.00 yr**

- Area : **220.92 ± 25.00 km²**

- Volume difference : **-3480708600 ± 575623115 m³ (-64455933 ± 10659417 m³/yr)**

- Volume difference : **-3.4807 ± 0.5756 km³ (-0.0645 ± 0.0107 km³/yr)**

Page 8

EAGLOO
DEM Modification Software

Report : Eagloo appendix

- Density : **0.917 ± 0.005 g/cc**

- Mass difference : **-3.1918 ± 0.6977 GT (-0.0591 ± 0.0129 GT/yr)**

- Contribution to sea level rise : **0.008866 ± 0.001938 mm SLR (0.000164 ± 0.000036 mm/yr)**

- Meter water equivalent : **-14.4475 ± 2.8961 m.w.e. (-0.2675 ± 0.0536 m.w.e./yr)**

Appendix A.15: Example of a report generated by Eagloo software, four calculation steps were processed: subtraction, interpolation, errors, volume and mass change.

List of figures

Figure 1.1: Temporal evolution of public camera resolution, in megapixels, as a function of the year. (data: Youssef, 2005).....	3
Figure 2.1: Presentation of the location of Folgefonna from satellite images (Maps data: Sentinel – 2B – 21/08/2021 and google earth image)	5
Figure 2.2: Presentation of the hydropower plants on the drainage basins of Folgefonna’s ice caps (Source: Geodata AS, NVE – Norwegian Mapping Authority).	7
Figure 3.1: Ice density as a function of depth – credit: Huss, 2013	13
Figure 4.1: Formula 4.2 applied to Sentinel 2 data of 2015	18
Figure 4.2: Presentation of the processing of photogrammetry for black and white photos	21
Figure 4.3: Raising image contrast with Photoshop	22
Figure 4.4: Application of the Wallis filter on a low contrast black and white photo of a part of Folgefonna	22
Figure 4.5: Black and white photography of the Folgefonna with masked frame (1962)...	23
Figure 4.6: Tie points cloud after the alignment step for 1962 – 3 Ground Control Points (GCPs) are placed.....	24
Figure 4.7: Mean values of $RMSE_z$ [cm], vs number of GCPs. Extremum of the bars indicate standard deviation – source: Agüera–Vega et al., 2017	24
Figure 4.8: Dense cloud generated from the tie points cloud presented in figure 4.6. (year: 1962).....	25
Figure 4.9: 3D model generated from the dense cloud presented in figure 4.7 (year:1962)	25
Figure 4.10: Hypsometric distribution of the glacier and elevation change as a function of altitude.....	29
Figure 4.11: Normalized Median Absolute Deviation as a function of the maximum absolute curvature and slope (calculated for Folgefonna).....	31
Figure 4.12: Variogram of the sample count standardized.....	32
Figure 4.13: Water equivalent thickness fluctuation obtained on GRACE’s website – GRACE NASA data analysis tool.....	33
Figure 4.14: Rosendal and Bergen station location.....	34
Figure 4.15: Buerbreen glacier, with RGI outlines and aerial LiDAR DEM.....	37
Figure 4.16: Catchment area and flowlines of Buerbreen	37
Figure 4.17: Ice thickness of Buerbreen	37
Figure 4.18: Volume evolution of Buerbreen on the 200 future years.....	37
Figure 5.1: Unfiltered glacier area of the three ice caps of Folgefonna	41
Figure 5.2: Filtered glacier area of the three ice caps of Folgefonna glacier	41
Figure 5.3: Evolution of the glacier area of Søndre Folgefonna – filtered.....	42
Figure 5.4: Evolution of the glacier area of Midtre Folgefonna – manually filtered	43

Figure 5.5: Evolution of the glacier area for Nordre Folgefonna – manually filtered	43
Figure 5.6: ELA between 1987 and 2022, for the three ice caps of Folgefonna.	44
Figure 5.7: Evolution of ELA for Søndre Folgefonna from 1987 to 2022.....	45
Figure 5.8: Evolution of ELA for Midtre Folgefonna.....	45
Figure 5.9: Evolution of the ELA for Nordre Folgefonna from 1987 to 2022.....	46
Figure 5.10: Evolution of the snow area for the three ice caps from 1987 to 2022, at the end of the ablation period (August – September)	46
Figure 5.11: DEM (black and white layer) used to monitor the evolution of Folgefonna since 1937.....	50
Figure 5.12: Evolution of the mass and volume change of the three ice caps of Folgefonna	50
Figure 5.13: Evolution of the volume and mass for a local region of Folgefonna.....	52
Figure 5.14: Gravimetric water mass variation of Folgefonna – by the center for space research (CSR) – from April 2002 to December 2021.....	52
Figure 5.15: Gravimetric water mass variation of Folgefonna – by the NASA’s Jet Propulsion Laboratory (JPL)– from April 2002 to December 2021	53
Figure 5.16: Presentation of Drangajökull’s location from satellite images	53
Figure 5.17: Gravimetric water mass variations for Drangajökull – by the Center for Space Research (CSR) – from April 2002 to December 2021	54
Figure 5.18: Simplified diagram of the EAGLOO software.	55
Figure 5.19: Temperature as a function of time from 1931 to 2021 – Bergen Florida station	61
Figure 5.20: Precipitation as a function of time, from 1931 to 2021 – Rosendal Station ...	61
Figure 5.21: Mean cloud cover as a function of time, from 1937 to 2021 – Bergen Florida station	62
Figure 5.22 : Comparison of glacier features and climatic data for the correlation between the glacier area, the ELA and climatic data.	63
Figure 5.23: Correlation between GRACE data and temperatures of the Bergen station and the precipitations of the Rosendal station	65
Figure 5.24: Evolution of the volume of the three ice caps of Folgefonna from 1902 to 2021	66
Figure 5.25: Surface evolution of the three ice caps of Folgefonna between 1902 and 2021	66
Figure 5.26: Evolution of the three ice caps of Folgefonna, from 2022 to 2100 calculated with OGGM.....	67
Figure 5.27: Glacier area evolution from 2022 to 2100.	67

List of tables

Table 4.1 : Measured accuracy of the different glacial mapping methods from Landsat TM data (credit: Albert, 2002)	18
Table 4.2: Presentation of the data used to compute the glacier area, ELA and snow coverage	20
Table 4.3: Presentation of image dataset used for DEM calculation.....	21
Table 4.4: Presentation of formerly completed Folgefonna DEMs and the applied post-processing.....	27
Table 5.1: Results obtained by photogrammetry	47
Table 5.2: Co-registration results for each DEM	48
Table 5.3: Glacier area covered without interpolation	49
Table 5.4: Errors of in volume and mass difference between all DEMs.....	49
Table 5.5: Results for the volume difference, mass difference, meter water equivalent and contribution to sea-level rise for all DEMs	50
Table 5.6: Errors in volume and mass change for all DEMs.....	51
Table 5.7: Evolution of glacier features of a local region of Folgefonna from 1937 to 2017	51
Table 5.8: Normalized Median Average Deviation (NMAD) as a function of the methods	56

List of diagrams

Diagram 3.1: Co-registering process for a DEM to a reference DEM with the Nuth and Kääb algorithm credit: Nuth and kääb, 2011	11
Diagram 4.1 : General presentation of the methods	15
Diagram 4.2 : Presentation of calculation process to obtain the glacier area from multiband satellite imagery	16
Diagram 4.3 : Calculation method to determine the altitude of TSL average (ELA) and associated standard deviation	19
Diagram 4.4 : Simplified processing for DEM alignment and interpolation	28

List of appendices

Appendix A.1: Model builder for drawing Glacier area and snow Glacier area during the autumn. Model builder A calculates the AGEI ratio, while Model builder B allows to calculate polygon surface from AGEI ratio raster.....	80
Appendix A.2: Model builder for Glacier area calculation.....	81
Appendix A.3: Wallis script used to increase the contrast of the images	81
Appendix A.4: Conversion of the calibration reports distances into coordinates, by using Geometry GeoGebra software.....	82
Appendix A.5: Wallis function used to increase the contrast of pictures locally.....	83
Appendix A.6: Ice density as a function of the type of solid water	83
Appendix A.7: Evolution of the Søndre Folgefonna glacier area without filtering	84
Appendix A.8: Evolution of the Søndre Folgefonna glacier area without filtering	84
Appendix A.9: Evolution of the glacier area of the Nordre Folgefonna without filtering..	84
Appendix A.10: Evolution of the snow area for the Søndre Folgefonna from 1987 to 2022, at the end of the ablation season (August – September).	85
Appendix A.11: Evolution of the snow area for the Midtre Folgefonna from 1987 to 2022, at the end of the ablation season (August – September).	85
Appendix A.12: Evolution of the snow area from 1987 to 2022 at the end of the ablation season (August to September).....	85
Appendix A.13: Water mass variation by gravimetry for the Drangajökull – carried out by the Center for Space Research (CSR) – from April 2002 to December 2021	86
Appendix A.14: Frontend of the software Eagloo, on the upper left, there is the main dialog, where the user can fill out all necessary entries. On the upper right there is a console. On the lower half graphs are displayed at the end of an execution.	86
Appendix A.15: Example of a report generated by Eagloo software, 4 calculation steps were processed: subtraction, interpolation, errors, volume and mass change.	88